Photons in Pb-Au Collisions at 158 A GeV

INAUGURAL-DISSERTATION

Matthias Messer

INAUGURAL-DISSERTATION
zur
Erlangung der Doktorwürde
der
Naturwissenschaftlich-Mathematischen
Gesamtfakultät
der
Ruprecht-Karls-Universität
Heidelberg

vorgelegt von
Dipl.-Phys. Matthias Messer
aus Hofheim im Taunus

Tag der mündlichen Prüfung: 2. Dezember 1998

Photons in Pb-Au Collisions at 158 A GeV

Gutachter: Prof. Dr. Hans Joachim Specht
Prof. Dr. Jürgen v. Krogh

Photonen in Pb-Au-Kollisionen bei 158 A GeV

Diese Arbeit beschäftigt sich mit der Suche nach direkten Photonen in Schwerionenkollisionen bei ultrarelativistischen Energien. Direkte Photonen werden von einem heißen Hadron-Gas oder einem Quark-Gluon-Plasma emittiert. Theoretische Rechnungen sagen für dieses Signal eine Rate von (5-10) % voraus, verglichen mit dem Photon-Untergrund aus hadronischen Zerfällen. Analysiert wurden Daten des CERES Experiments am CERN SPS aus der Strahlzeit im Herbst 1996. Photonen wurden über die Konversion in ein Elektron-Positron-Paar identifiziert. Mit den 34000 rekonstruierten Photonen wurden Transversalimpusspektren und Multiplizitätsspektren erzeugt, auf Detektoreffekte korrigiert und auf die Anzahl der neutralen Pionen pro Ereignis absolut normiert. Zur Bestimmung des Untergrundes aus hadronischen Zerfällen wurde ein Zerfallsgenerator verwendet, der den hadronischen Endzustand, wie er in Schwerionendaten gemessen wurde, beschreibt.
Das Ergebnis ist ein Überschuß von (12 +13 -13.4) % verglichen mit dem Untergrund. Daraus resultiert eine Obergrenze für die Prodution direkter Photonen von 33.8 % auf einem Vertrauens-Niveau von 90 %.
Die Produktionsrate von Photonen wurde auch als Funktion der Multiplizität untersucht. Im Rahmen der Fehler ist keine Abweichung von einer Konstanten festzustellen. Die gemessene Steigung ist $\alpha = (2.5 \pm 1.3_{stat}\ (+2.5\ -3.7)_{sys}) \cdot 10^{-4}$. Unter der Annahme, daß die Produktion direkter Photonen quadratisch mit der Multiplizität skaliert, läßt sich eine Obergrenze von 21 % ableiten.

Photons in Pb-Au Collisions at 158 A GeV

The objective of the work presented here is the search for direct photons in heavy ion collisions at ultrarelativistic energies. Direct photons are emitted from a hot hadron gas or from a quark-gluon-plasma. Theoretical calculations predict a rate for this signal of some (5-10) % as compared to the photon background from hadron decays. The measurement was done with data of the CERES experiment at the CERN SPS, taken in the fall of 1996. Photons were identified by their conversion into an electron-positron-pair. With a final sample of 34000 photon conversions, spectra in transverse momentum and charged particle multiplicity were produced, fully corrected for detector effects and normalized to the number of neutral pions in an event. For the determination of the hadron-decay background a decay-generator is used which describes the hadronic final state as observed in heavy ion data. The result is a photon excess of (12 +13 -13.4) % over the hadronic yield which is not significant within its error . The upper limit for such a signal is 33.8 % on the 90 % confidence-level. The photon production ratio as a function of multiplicity shows, within errors, no deviation from a constant. The slope parameter is $\alpha = (2.5 \pm 1.3_{stat}\ (+2.5\ -3.7)_{sys}) \cdot 10^{-4}$. With the assumption that the number of direct photons scales quadratically with multiplicity the resulting upper limit for a direct photon excess is 21 %.

“There is a theory which states that if ever anyone discovers exactly
what the Universe is for and why it is here,
it will instantly disappear and be replaced by
something even more bizarre and inexplicable.”

“There is another theory which states
that this has already happened.”

DOUGLAS ADAMS

“I don’t like it, and I’m sorry
I ever had anything to do with it.”

ERWIN SCHRÖDINGER
1887-1961

Contents

List of Figures

List of Tables

Chapter 1

Introduction

In the effort to describe the fundamental structure of matter, heavy ion collisions at high energies provide a unique opportunity. In the laboratory, a scenario can be created which resembles the situation in the very early universe some 10^{-5} seconds after the big bang.
The produced energy densities are in fact so high that one can expect the confinement of quarks into hadrons to be overcome, that is to observe a phase transition from hadronic matter to a plasma of quarks and gluons (QGP) [1]. Theoretical approaches which avoid the problem of infrared divergence by limiting themselves to small cells in phase-space, so called lattice QCD calculations, indeed predict such a phase transition to occur at densities of 2-4 GeV/fm^3.

Heavy ion collisions have been studied at the Brookhaven AGS and the CERN SPS where projectiles were shot on fixed targets at energies as high as 14.6 GeV/nucleon and 200 GeV/nucleon respectively, featuring collision systems as large as gold on gold or lead on lead. Various observables have been measured and it was shown that energy densities of 2-3 GeV/fm^3 have been reached. Among the most prominent observations which indicate new physics are the *anomalous* suppression of the J/ψ measured by the NA50 experiment [2] and an excess production of lepton pairs, the main objective of CERES [3, 4, 8, 10]. The former observation is thought to be an indication of *colour screening* [9] as one would expect to occur in a quark gluon plasma, whereas the latter is presently explained as accompanying a restoration of chiral symmetry. The fact that both results were obtained by studying lepton pairs demonstrates nicely the power of this particular type of experiment. Since lepton pairs and, including photons, electromagnetic probes in general are not subject to strong interaction, most of them leave the reaction volume unperturbed and thus carry information about the hot initial phase of the collision.

The CERES experiment at the CERN SPS is the first and so far only experiment which has been explicitly designed for the measurement of e^+e^--pairs in proton-nucleus and nucleus-nucleus collisions at such high energies. Main part of the spectrometer are two ring imaging Čerenkov detectors, before and after an azimuthally deflecting magnetic field. Due to the high Čerenkov threshold of $\gamma_{th} = 32$, most of the charged hadrons produce no signal at all, whereas electrons produce ring images of asymptotic radius and are thus identified. The momentum is measured by the deflection in the magnetic field. Two radial silicon drift detectors close to the interaction point and a multi-wire proportional chamber at the downstream end of the spectrometer give additional points on each particle trajectory. The silicon drift detectors are also used for a precise determination of the event vertex.

A large fraction of all observed electron-positron pairs are produced by the conversion of photons. For the pair analysis quoted above, this is one of the largest sources of background. This also means that, once the exact conversion length of all relevant material is known, CERES can be used to precisely measure the production rate of photons. High precision is indeed of the essence, since the theoretically predicted rate of photons coming directly from a hot hadron gas or a quark-gluon plasma is small (5-10%) compared to the number of photons from hadron decays. Measurements of direct photons have been performed in S-Au collisions but, due to this difficult background situation, no definite statement on the presence or absence of such a signal could be made [7,11,13].
The search for direct photons in Pb-Au collisions at 158 GeV per nucleon is the subject of the work presented here. The following chapter gives an introduction to the theoretical aspects of photon production. In Chapter 3 the CERES experiment is explained, followed by a description of the analysis software in chapter 4 and an outline of the procedure to get a final sample of photons in chapter 5. The correction of the data for spectrometer efficiency and acceptance, as well as the determination of the conversion length with Monte-Carlo studies is explained in chapter 6. A signal of direct photons can be obtained only if the amount of photons from conventional sources, i.e. hadron decays, can be predicted with sufficient precision. The ingredients of the hadron decay generator used for this purpose are the subject of chapter 7. Chapter 8 shows the final results and chapter 9 provides a discussion of their implications.

Chapter 2

Direct Photons

Photons in heavy ion collisions are mainly produced by the decay of hadrons. The production rate of neutral pions is roughly half the measured number of charged particles and they decay with a branching ratio of 98.9 % into two photons. In the case of CERES, which measures a mean charged particle multiplicity of 220 in one event, some 200 photons from this source are emitted into the spectrometer acceptance. The yield from other photon-sources, discussed in the following paragraphs, is smaller by two orders of magnitude and must therefore be found in a large background.

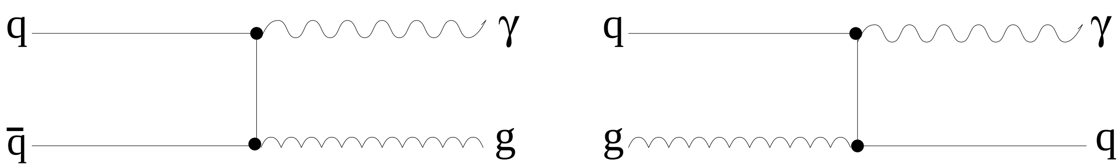

Figure 2.1: Feynman graphs for direct photon production

Photons produced by quark-quark annihilation or quark-gluon compton-scattering are called *direct photons.* To first order α_s the processes are described by the Feynman graphs in figure 2.1.

2.1 Hard Processes

In the initial state of a heavy-ion collision direct photons are produced by parton scattering. A constituent quark (or a gluon) of an incoming nucleon reacts with a constituent quark (or a gluon) of a target nucleon. The cross-section due to parton collisions can be calculated with a hard-scattering model [14]. Since these processes require a high momentum transfer q^2, the outgoing photon-momenta are also large. The prediction of this signal has caused extensive experimental activity in the 1980's both at CERN[1] and at FNAL [2] [15–17]. The result of the E629-collaboration [15] is shown in figure 2.2. A clear signal is obtained for $p_\perp > 2$ GeV/c. Figure 2.3 gives a summary of E629, E704, and NA3 data. Here the background from hadron decays is subtracted. All three experiments are in good agreement with each other and also with the theoretical predictions. The direct photon signal from hard initial-state processes can be regarded as a well established fact.

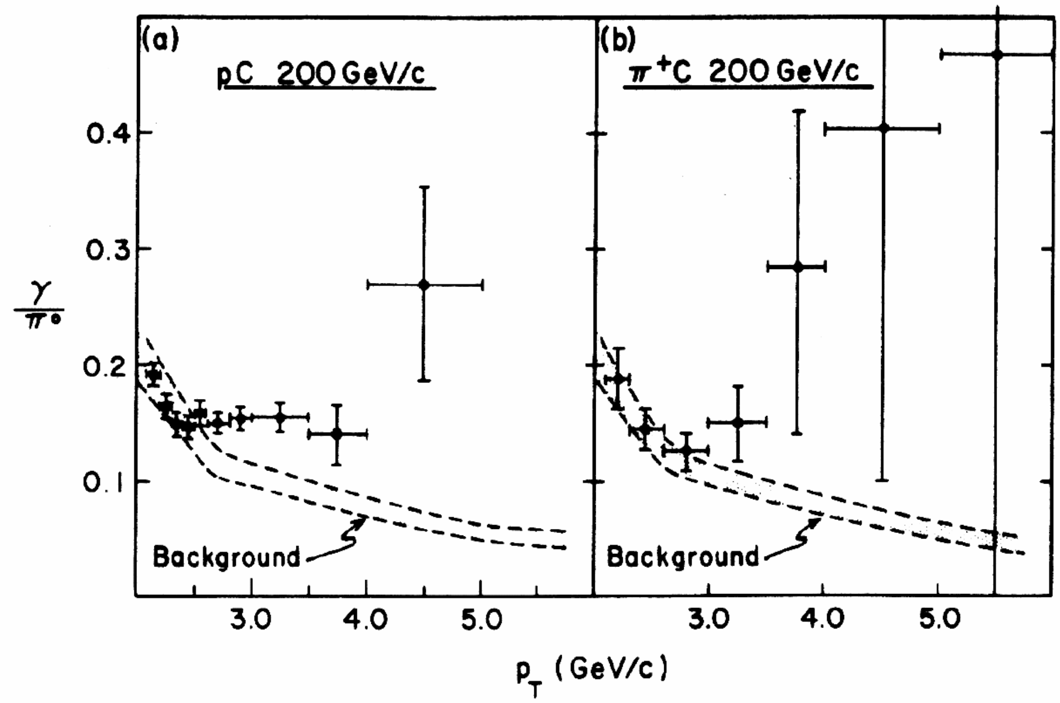

Figure 2.2: Direct photons measured by the E629 Collaboration at the FNAL. A strong rise above the hadronic background is visible for $p_\perp > 2$ GeV/c.

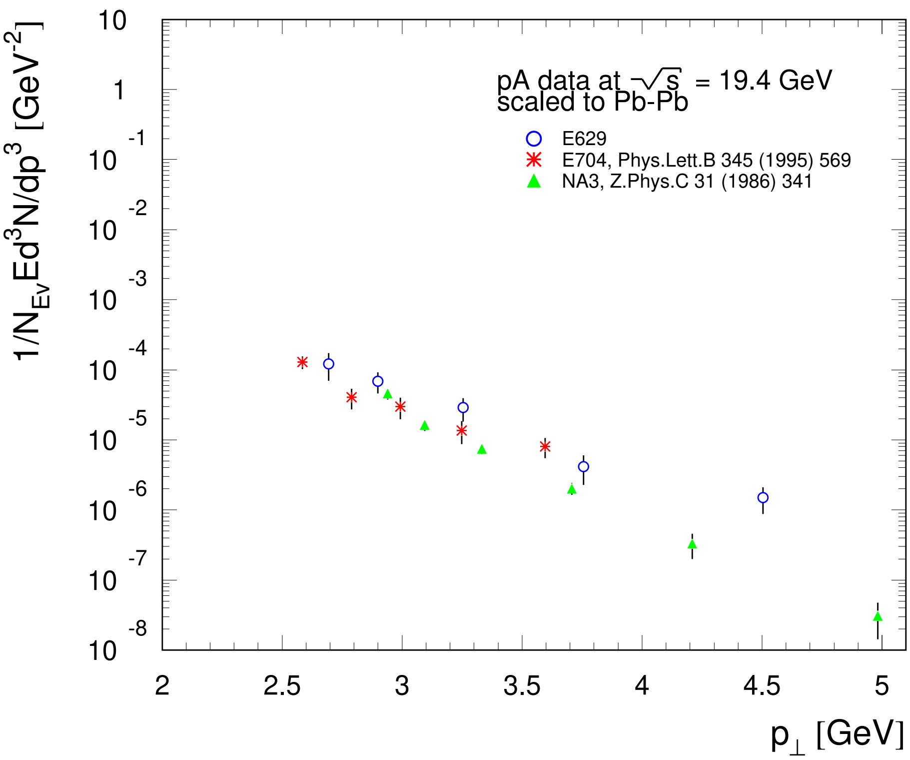

Figure 2.3: Summary of measurements of direct photons.

2.2 Production of soft direct photons

For sufficiently high energy densities, lattice QCD calculations predict a phase transition into a state where quarks and gluons can move freely, without being confined into hadrons. This state of matter is commonly referred to as a *quark-gluon-plasma* (QGP). The processes for direct-photon production no longer require a high momentum transfer and a yield of direct photons could be seen at smaller $p_\perp$. The ratio of such a signal versus the background of hadronic decays has been calculated by several groups in the past [18–20]. The first-order Feynman graphs are again those in figure 2.1. For calculating the differential cross sections, one does not use the structure functions of quarks and gluons in a nucleon, as done for the hard parton-scattering, but rather a thermal distribution of point-like sources - free quarks and gluons. All of these authors come to the conclusion that the relative

[1]European Laboratory for Particle Physics
[2]Fermilab National Accelerator Laboratory

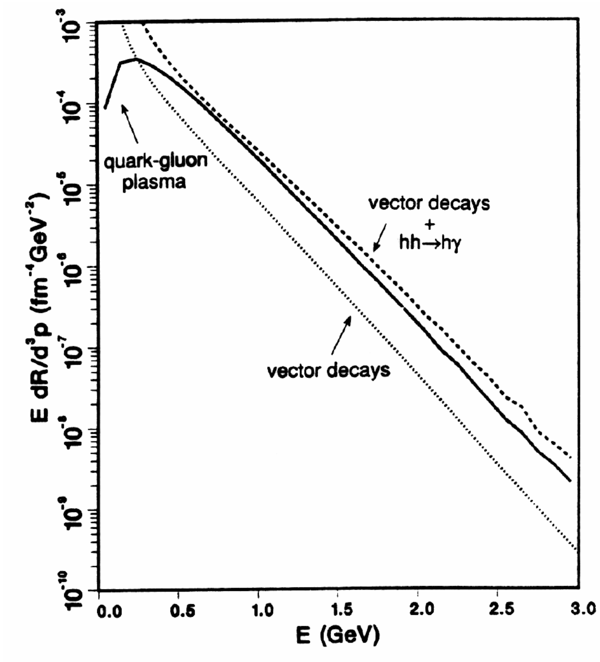

Figure 2.4: Spectra of direct photons from QGP and hot hadron gas as theoretically predicted by [20].

rate should be of the order of (5-10) %, compared to the hadron-decay photon yield. M. Neubert [18] finds that the number of direct photons scales quadratically with the charged particle multiplicity. Since photons from hadron decays show a linear dependence, one can hope to identify those from the QGP by measuring the inclusive yield versus multiplicity. An interesting result of J. Kapusta et al. [20] is that the production cross-section, as well as the spectral shape of direct photons from a QGP are indistinguishable from that of direct photons produced in a hot hadron-gas. Here the processes for photon production are mainly $\pi\pi$-annihilation and $\pi\rho$-compton-scattering. The first-order Feynman graphs look very much the same as those in figure 2.1. One only has to replace the quarks by pions and the gluons by ρ-mesons. The differential cross-sections are shown in figure 2.4. If this is true, one can principally not observe the phase transition by measuring direct photons. One consolation would be that then the measured momentum distribution would depend only on the temperature of the hot matter produced in the collision, making direct photons a good thermometer which does not depend on assumptions about the phase.

Several experiments have looked for soft direct photons at the CERN SPS. In principle they fall into two classes. One measures photons directly, using a calorimeter. This method is applied by the WA80/98 collaboration. The advantage is a high efficiency. Together with photons also neutral pions can be measured via the decay

$\pi^0 \rightarrow \gamma\gamma$. In this way a part of the systematic errors cancel in the calculation of the photon yield versus hadronic background.
Another way is to identify photons by their conversion into e^+e^--pairs as done by HELIOS and CERES. These experiments cannot measure π^0s, which is one of their largest sources of error. On the other hand, they do not suffer from a difficult measurement of a calorimeter efficiency. The small conversion length is no obstacle since it can be calculated or measured with extremely high precision.
So far none of these experiments have found conclusive evidence for direct photons. The kinematical ranges, the collision systems which have been studied, and the obtained upper limits are summarized in table 2.1 and figure 2.5. Figure 2.6 shows that also by measuring the number of photons as a function of charged particle multiplicity, no deviation from a linear dependence was found.

Experiment	y	$p_\perp$ (GeV/c)	system	upper limit	references
HELIOS-2	1.0-1.9	0.1-1.5	p-W,O-W,S-W	13%	[21]
WA80/WA98	1.5-2.1	0.4-2.8	O-Au	15%	[22]
	2.1-2.9	0.5-2.5	S-Au	12.5%	[13]
CERES	2.1-2.65	0.4-2.0	S-Au	14%	[7]

Table 2.1: Experiments searching for soft direct photons at CERN

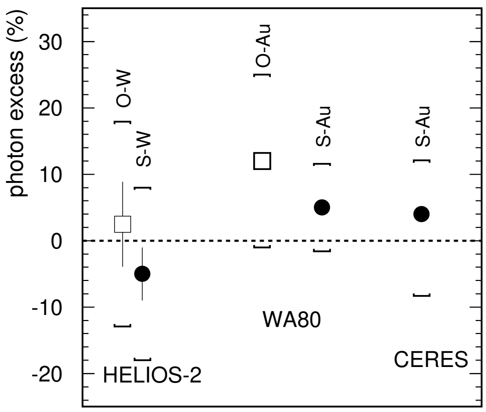

Figure 2.5: Summary of all attempts to detect direct photons with O- and S-beams of 200 GeV/nucleon . Shown is the fraction of the inclusive photon yield not accounted for by hadron decays. Statistical errors are indicated by bars, systematic errors by brackets.

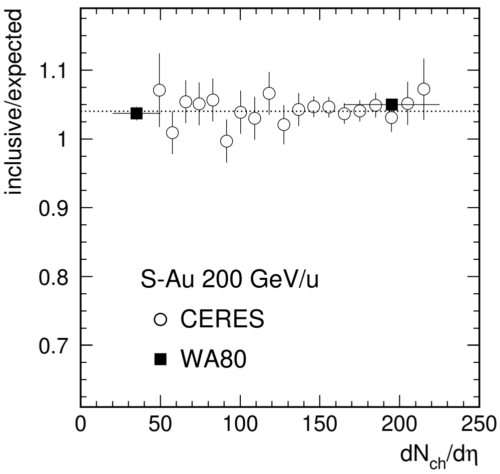

Figure 2.6: Inclusive photon yield normalized to the expected contribution from hadron decays as a function of the charged particle density.

Chapter 3

The CERES Experiment

CERES is an acronym for **ČE**renkov **R**ing **E**lectron **S**pectrometer. The experiment was designed mainly for the detection of electron-positron pairs with invariant masses up to 2.0 GeV/c^2, covering a range in pseudo-rapidity of $2.1 < \eta < 2.65$ [24]. The setup used until 1993, consisted mainly of two ring imaging Čerenkov detectors, before and after an azimuthally deflecting magnetic field. With this configuration measurements in p-Be, p-Au and S-Au collisions have been performed, culminating in the report of an excess production of e^+e^- pairs for invariant masses of more than 200 MeV in S-Au collisions at 200 GeV per nucleon [3]. In addition, photons have been measured by their conversion into e^+e^- pairs [11], and charged pions with a momentum above the ČErenkov threshold were analyzed [28].

The spectrometer as described here is a substantial upgrade, built in the years of 1994 and 1995 to cope with the extreme requirements of Pb-Au collisions. The high multiplicity observed in these interactions leads to a challenging background situation. Very few electron tracks have to be found among several hundred charged particles. An analysis relying on pattern recognition in the RICH detectors alone would not provide a reliable electron recognition and track reconstruction. The new setup as described below accounts for this difficulty with additional detector systems. Data has been taken and analyzed with this configuration in 1995, proving the success of the upgrade. In addition to the electron pair analysis [5,10] the new setup allows the measurement of several hadronic observables [25,26].

3.1 Overview

Figure 3.1 provides an overview of CERES. Main part of the spectrometer are two ring imaging Čerenkov detectors (RICH-1 and RICH-2) which provide particle identification and a measurement of the trajectory. The momentum is determined

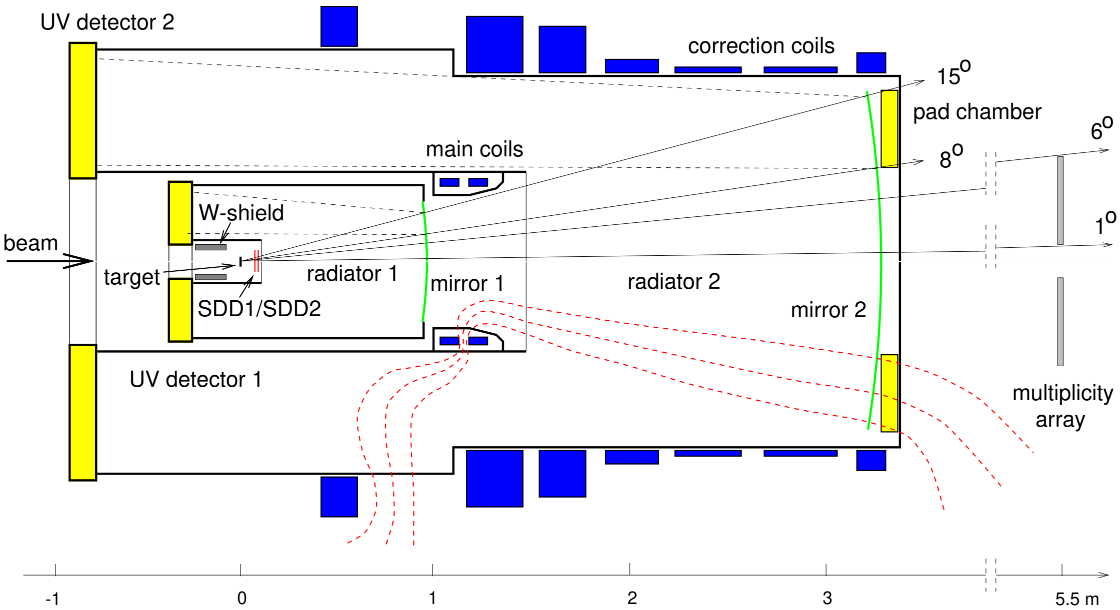

Figure 3.1: Overview of CERES

via the azimuthal deflection in a magnetic field between the two detectors. An additional point on each track is given by a set of two silicon drift detectors (SDD1 and SDD2) close to the target, and by a multi-wire proportional chamber with pad-readout (pad chamber) located downstream of RICH-2. The two SDDs, later on referred to as the target telescope, also allow a precise determination of the event vertex and a measurement of the charged particle multiplicity (Nch). The following section gives a brief description of the setup used for the dedicated photon run in 1996. More details can be found in [24].

3.2 The target region with the SDDs

The target itself and two silicon drift detectors used for tracking and vertex reconstruction form the so called target telescope. This region of the spectrometer is located upstream of the RICH radiator tanks but slightly downstream of the RICH readout chambers. This geometry ensures that the latter suffer as little as possible from background due to particles produced in the collision. Details of the target region are shown in figure 3.2.

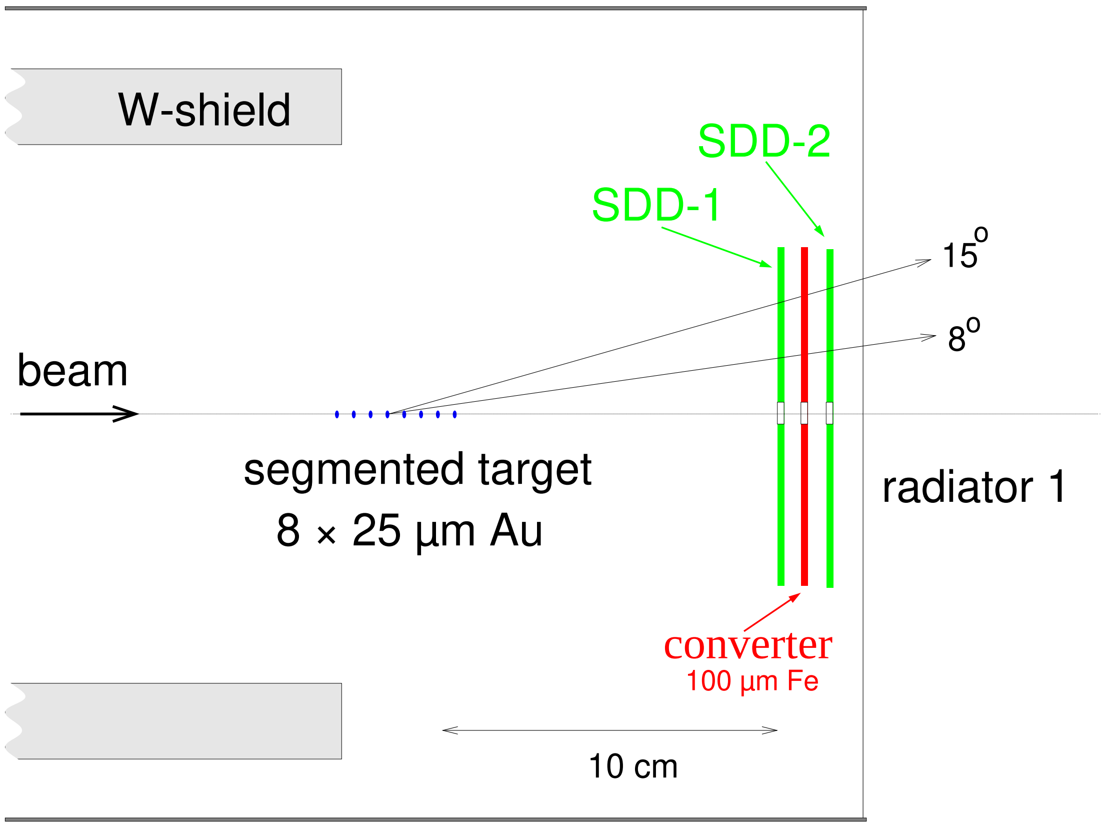

Figure 3.2: Details of the target region

3.2.1 The Au target

The target is segmented into eight Au-discs spaced 3 mm apart, each of 25μm thickness and 600μm diameter. This geometry ensures that particles from a collision which are emitted into the region of spectrometer acceptance will not hit any other disc, thus limiting the effective material to 12.5μm of gold i.e. 0.22% of a radiation length. A tungsten shield is installed around the target to absorb particles emitted backwards which could otherwise cause large background signals in the readout chamber of RICH-1.

3.2.2 The silicon drift detectors

A set of two 4″ silicon drift detectors (SDD) is located 11 cm downstream of the target. CERES is the first experiment which successfully implemented this detector concept and detailed descriptions of development, testing, and the setup in the experiment have been extensively published [29, 30, 35]. This section shall give a brief overview of working principles and implementation.

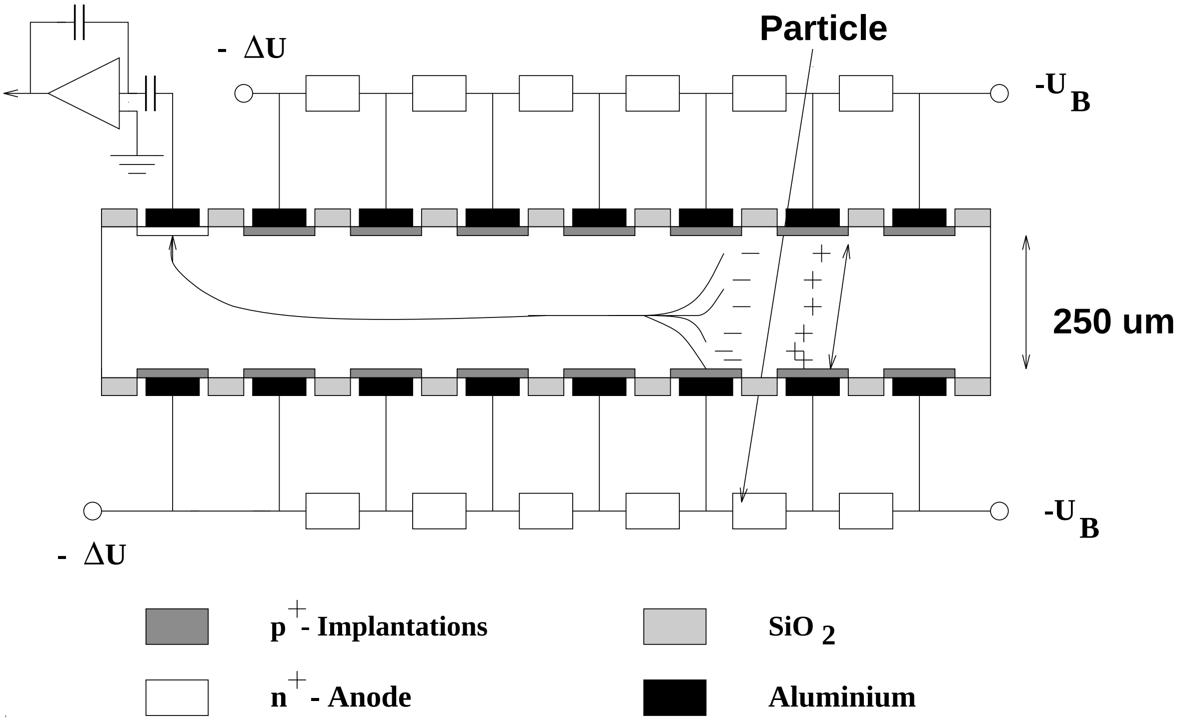

Figure 3.3: Working principle of the SDD

The 4″ SDD used in CERES is designed using the principle of sideward depletion [29]. A charged particle traversing the silicon will create an electron cloud which then drifts along an electric field to the outer rim of the silicon wafer (figure 3.3). There the charge is collected by 360 anodes which are connected to a fast, time sensitive readout system. Position information of such a hit is given by the anode number for the azimuthal coordinate, and the time measurement by an FADC system, which yields a radial coordinate under the assumption of a constant drift velocity. One of the technical improvements of this detector system, as compared to the 3″ SDDs used in previous years, is a split anode structure as shown in figure 3.4. The charge of one hit is detected by several anodes and a more exact position measurement can be made by calculating the center of gravity of this distribution. Measurements done for offline calibration show that the azimuthal precision which can be reached is 1.4 mrad, compared to 5 mrad for the old system. The error on the radial position is found to be 30 μm. Laser tests seem to indicate that the intrinsic precision is indeed even higher [30].
The SDD allows a measurement not only of the hit position, but also of the actual charge deposited, i.e. the energy loss (dE/dx). In particular, a clear distinction can be made between the signal of *one* as compared to *two* minimum ionizing particles (MIPs). Since an e^+e^- pair created by the conversion of a photon has a very small opening angle, it will deposit the energy of two MIPs in most cases within

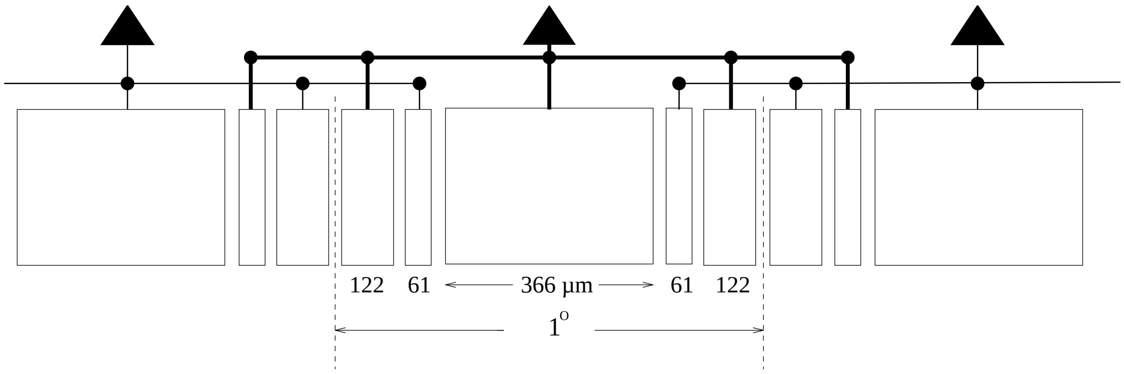

Figure 3.4: Split anode structure of the SDD

the double hit resolution of the detector, and thus be identified by requesting a hit with double dE/dx. This feature of the SDD is extremely important for the rejection of photon conversions, the most prominent background in the low mass pair analysis, and of course also for positive identification of photons, the objective of the work presented here.

3.3 The photon converter

For the dedicated photon run in the fall of 1996 a converter was installed between the two SDDs. A photon converting into an e^+e^- pair inside the converter will have a clear signature with a double dE/dx signal in SDD2 and no hit at all in SDD1. The photograph in 3.5 shows the layout of this device. From a steel disc with a diameter of 10cm and a thickness of 100 μm three segments are cut out and displaced by 40 degrees such that the resulting converter has a threefold repeated structure with the conversion length of zero, 100 μm, 200 μm of steel, respectively.

3.4 The RICH detectors

A Ring Imaging Čerenkov detector (RICH) combines the detection of Čerenkov radiation, which has been used for particle counting since the early days of particle detectors, with position measurement. This allows to determine the Čerenkov angle and thus measure the particle velocity. In combination with a known momentum the mass can be extracted and the particle identified. By using either a very thin radiator located before a two-dimensional readout device, or by reflection in a spheric mirror, light is focused into ring images. The diameter of this ring then corresponds to a certain Čerenkov angle.

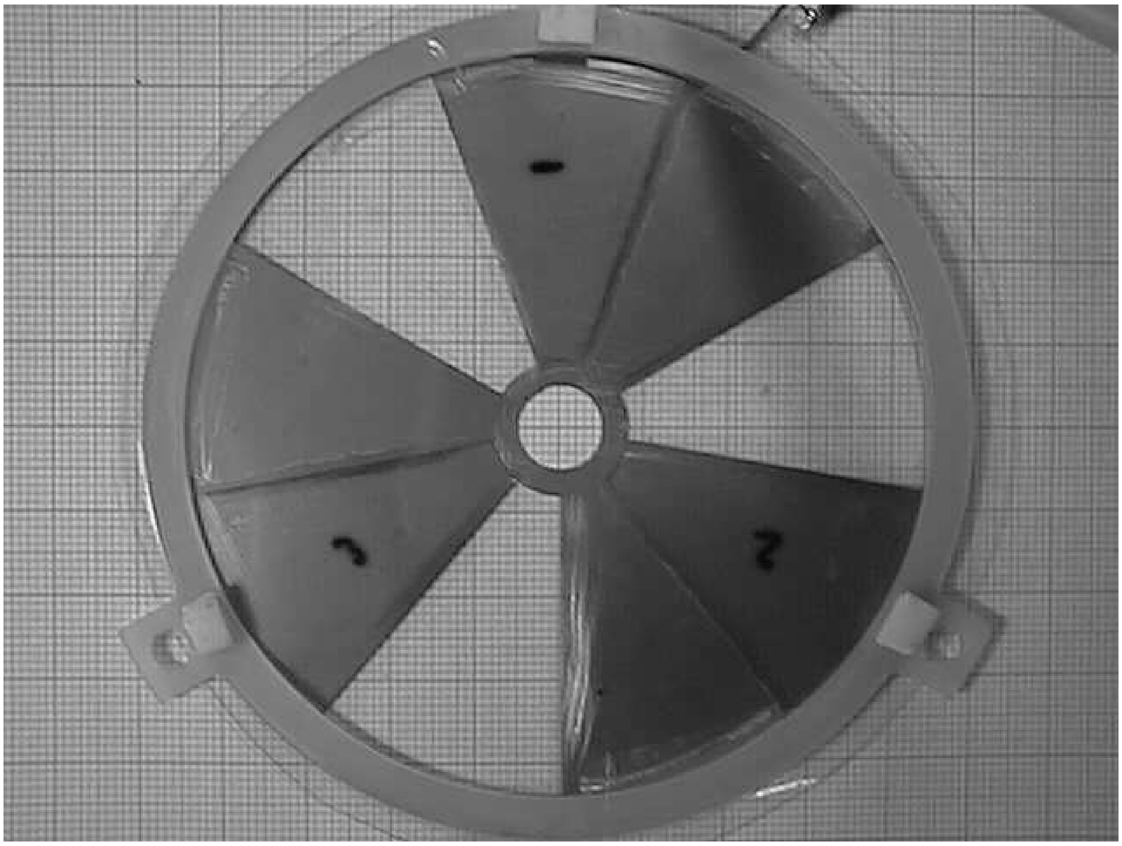

Figure 3.5: Photograph of the photon converter. The material is 100 μm steel, segmented into areas of zero, single and double thickness. The outer diameter is 10cm.

The RICH detectors in the CERES experiment operate with CH_4 at atmospheric pressure as a radiator gas. The threshold for Čerenkov radiation is thereby reached at a Lorentz factor of $\gamma_{th} = 32$. This means that electrons produce light at an asymptotic angle

$$\theta_\infty = \frac{1}{\gamma_{th}} \ , \tag{3.1}$$

whereas most hadrons, except pions with a momentum of more than 4.5 GeV, produce no signal at all. The detector is *hadron blind*.

The produced light is reflected by spheric mirrors which are mounted such that the target is in the focal point. Light which is emitted at a certain angle in the radiator is focused to a ring in the focal plane with radius

$$R = R_\infty \left[1 - \left(\frac{\gamma_{th}}{\gamma}\right)^2\right]^{-\frac{1}{2}} \tag{3.2}$$

where R_∞ is 31.25 mrad for the chosen radiator gas. The distance of the ring center on the focal plane to the focal point depends on the polar angle at which

the particle traversed the radiator. This means that a RICH can measure only angles of trajectories. Particles traveling at identical angles will produce the same ring image.
The number of photons on a ring is given by

$$N_\infty = N_0 \frac{L}{\gamma_{th}^2} \quad , \tag{3.3}$$

where N_0 is a detector constant and L is the radiator length. With the high value of $\gamma_{th} = 32$ the light output is anyway meager, typically of the order of some ten photons on a ring. It is of great importance to optimize all detector components for maximum light transmission. N_0 is $131cm^{-1}$ for RICH-1 and $75cm^{-1}$ for RICH-2. The difference of these numbers is mainly due to the window which separates the radiator tank on the upstream end from the readout chamber. Whereas for RICH-2 this consists of quartz, for RICH-1 the material is CaF_2 which has a higher UV transparency. This compensates for the different radiator lengths of the two detectors and yields an asymptotic N_∞ of 11.2 for RICH-1 and 9.5 for RICH-2 with the presently used analysis software. In the non asymptotic case the number of photons depends on the Lorentz factor with

$$N = N_\infty \left[1 - \left(\frac{\gamma_{th}}{\gamma} \right)^2 \right] . \tag{3.4}$$

To minimize the number of photon conversions in the spectrometer and to get the least possible loss of momentum resolution due to multiple scattering, the amount of material within the acceptance is kept as low as possible. The RICH-1 mirror is therefore based on a thin carbon fiber structure which defines the spherical geometry and a vaporized coating of aluminium for reflectivity. Whereas the radiation length is only 0.4%, the reflectivity is with 85% the same as for the glass mirror of RICH-2.

The UV detectors are gas counters (94% He, 6% CH_4). The incoming photons are converted into electrons by added TMAE (Tetrakis-di-Methyl-Amino-Ethylen). The primary produced electron is then amplified in three steps to $2 \cdot 10^5\ e^-$. The ion cloud produced in the last step induces a signal on a pad plane of 53800 pads in RICH-1 and 48400 pads in RICH-2. The pad sizes are $(2.7\ \mathrm{mm})^2$ and $(7.6\ \mathrm{mm})^2$ respectively which corresponds to 2 mrad per pad in both cases.

3.5 The Pad Chamber

The pad chamber is located closely behind the mirror of RICH-2. It is a multi wire proportional chamber with an almost identical copy of the pad readout of

RICH-2. Its 20000 pads cover a polar angle which corresponds to an interval of $2.0 < \eta < 2.7$ in pseudo-rapidity and give a spacial resolution of 0.6 mrad. By measuring an additional point on each track the amount of background rings in RICH-2 can be greatly reduced. The analysis of 1995 and 1996 data has shown that this is of vital importance in the environment of large charged particle multiplicities as reached in Pb-Au collisions. A short circuit in the high voltage distribution of one of four sectors made some 25 % of the pad-chamber unusable for the photon run.

3.6 The Magnetic field

A pair of super-conducting solenoidal coils, located between the radiators of the two RICHes, produces a magnetic field which deflects charged particles in azimuthal direction. The polar angle remains to first order unchanged. This allows to identify rings in the two detectors which belong to the same track. The deflection $\Delta\Phi$ gives a momentum measurement with

$$p = \frac{144mrad}{\Delta\Phi}\ [GeV/c] \quad . \tag{3.5}$$

The opposite sign currents in the two coils produce a sharply located azimuthal kick and also leave the radiator of RICH-1 essentially free of magnetic field. To ensure that the particle travels unobstructed through the radiator of the second RICH, a set of warm coils form the field parallel to the particle trajectories (figure 3.1). Since the azimuthally deflected particles cross the lines of force, in second order, the track is slightly bent towards the beam axis. The angle is

$$\Delta\Theta = 66.2(\Delta\phi)^2 \frac{\mathrm{mrad}}{\mathrm{rad}^2} \quad . \tag{3.6}$$

This effect is corrected in the analysis software.

3.7 The Trigger

The detector readout is triggered, if a beam-particle reaches the target, but does not enter the spectrometer. In addition a minimum charged particle multiplicity is required. This is realized by a set of Čerenkov beam counters (BC1,BC2,BC3), a veto counter (VC) and a multiplicity detector (MD) which are both plastic scintillators. BC1 is located 60 m upstream of the experiment, BC3 is directly downstream of the target and BC2 is at the downstream end of the spectrometer. The MD covers a polar angle between 1^o and 6^o, 5 m behind the pad chamber. A trigger decision requires a signal in BC1, no signal in BC2, BC3, VC, and around 100 charged particles in MD. This represents roughly 35% of the geometrical cross-section in Pb-Au collisions.

Chapter 4

Data Recording and Offline Analysis

CERES has been designed to measure e^+e^--pairs at low invariant masses. Of particular interest is the region around the ρ/ω resonance at 770 GeV/c^2. Looking at particle production ratios and the branching ratios for decays into e^+e^-, one sees that these pairs have to be extracted from a huge background. The e^+e^- cross section for photon conversions and π^0 decays dominates that of the signal of interest by four orders of magnitude. Since this problem arises mainly at very low masses ($<$ 200 MeV/c^2), it can be removed by a cut on the mass. But even then it enters the analysis as *combinatorial background.* One track of an only partly reconstructed photon conversion or π^0-Dalitz-decay can be combined with another electron track and create a pair at masses above 200 MeV/c^2. This requires not only an exceedingly good capability of background rejection, but means also that four to five orders of magnitude more heavy ion collisions have to be recorded than the number of pairs desired in the final sample. In principle, an analysis of photon conversions profits from this. A difficult background situation for the low-mass pairs means that a large sample of conversions is easily accumulated. Since, however, one desires a small statistical error also for the highest measurable transverse momentum ($p_\perp$) in an exponentially decreasing spectrum, a very large sample is indeed required. The signal of direct photons has to be extracted from a large physical background, i.e. the decays of hadrons into photons, which one expects to account for some 90 % of the total yield.
Data of $6 \cdot 10^7$ events has been taken during six weeks of beam time in the fall of 1996 to extract a sample of 2000 pairs with masses between 0.2 and 2.0 GeV [27]. Another five days were dedicated for data taking with the special setup for photon conversions, resulting in four million Pb-Au events and, in total, 70000 photons. Of the events recorded during the dedicated photon run, $1.5 \cdot 10^6$ events were taken with a special setup in which the magnetic field was reduced to 30 % of its

nominal strength. Since the field plays an important role in deflecting particles with very low momenta (such as delta-electrons) out of the acceptance, this gives a completely different background situation. A separate analysis of this data can be used as a consistency check. The smaller deflection of electron trajectories results in a search-window which is narrower in azimuthal direction. This should improve the measurement of photons with small transverse momenta. The analysis of this data-set is at present incomplete and therefore plays no role in the work presented here. Looking at the correction function, however, one can say that, using the same criteria as described in chapter 8.1, it will be possible to measure photons in the region 0.2 GeV/c $< p_\perp <$ 0.8 GeV/c.
CERES is a high luminosity experiment. The following paragraphs explain how these large data volumes are handled with sufficiently high speed.

4.1 The Data Aquisition System

During the five seconds of beam-extraction onto the target, the so called *burst*, CERES records data of up to 1200 multiplicity triggered collisions. This is achieved by a data aquisition system (DAQ) with very high rate capability combined with a highly compressed data format. Zero suppression and Huffmann coding are done by purpose-built hardware directly in the readout systems of the individual detectors. For each detector, the information is buffered in memory modules which are linked by a VME bus to the DAQ-CPUs. There the further processing is done by software. An event-builder program collects all information from the memory modules and packs everything relevant for one event into a structure of data and labels. The such produced stream is stored in the CPU memory and written to tape during the ten second interval between two bursts, using nine DAT[1] drives in parallel. The front-end readout and the software DAQ run asynchronously by means of a two-event pipeline in-between. In this way the impact of dead-times in one of the systems is substantially reduced.
The 65 million events recorded in the 1996 beam time for both the open-pair and the photon analysis occupy some 50 kBytes each and thus amount to a total of 3.2 TByte on some 1800 DAT cassettes.

4.2 Requirements for Offline Analysis

The immense amount of data expected for the Pb run, along with several modifications of the spectrometer, i.e. the introduction of additional detectors, considerably

[1]Digital Audio Tape

increased the demands on the analysis software. For the setup before 1994 a complete package for offline analysis as well as Monte-Carlo simulation was written in Fortran 77.
Processing the Pb data required additional code. New algorithms were needed to cope with the difficult background situation. Since CPU resources are limited, speed was also of the essence. The sheer amount of data dictated the maximum time which could be allowed for the processing of one event. In 1994 it was therefore decided to add this code and indeed, to rewrite the complete software package in a more modern programming language: Fortran 90.
By the end of 1995 some 40000 lines of code existed and the first steps of analysis, like detector calibration and the testing of new algorithms, were performed in this environment. However, it soon became clear that the situation was not ideal. The code was still incomplete, several low-level routines already had to be written in C, and software companies stopped to support Fortran 90. The existing compilers produced very inefficient code and there were no debugging tools available. Again one decided to change horses.
During the first four months of 1996 the whole offline software of CERES was redesigned and rewritten in an object-oriented way, using the programming language C++. This particular choice had several reasons.

- C++ compilers are available for almost every platform. They produce efficient programs. The gain in speed one anticipated from benchmark tests comparing to Fortran 90 was around a factor of four. The development environments are modern and user friendly, including graphic desktop debuggers and static analyzers.

- The still missing code could be added in one of the most modern programming languages.

- The special features of C++ like inheritance, encapsulation and strong type checking make software packages easy maintainable.

- The usage of C++ and object-oriented design in general are the official policy of CERN for the experiments at the large hadron collider (LHC). This meant that help from CERN R&D people and easy access to commercial software libraries could be expected.

- Storage of raw data and production output (DST) can be done in a more modern way, using an object-oriented database.

- The offline software would be compatible with programs used for data aquisition, already written in C or C++.

Using this new analysis package, the complete processing of one event takes on average 2.5s on a SUN HyperSparc processor. The subset of the 1996 data from the dedicated photon run, the basis of the analysis presented here, was processed on a parallel computer which consists of 128 such processors, the CS2 at the CERN computing center. 32 of those CPUs where allocated to CERES. At a CPU efficiency of some 80% the processing of the $4 \cdot 10^6$ events took about 4.5 days.

4.3 COOL Software

COOL stands for **C**ERES **O**bject **O**riented **L**ibrary. This collection of more than 100 classes contains the entire offline software of the experiment. The features of C++ which were found to be extremely useful and which are used throughout the code shall be briefly discussed with some examples in the following paragraphs. See [32,36] for a detailed description of the language and the underlying philosophy.

4.3.1 Inheritance

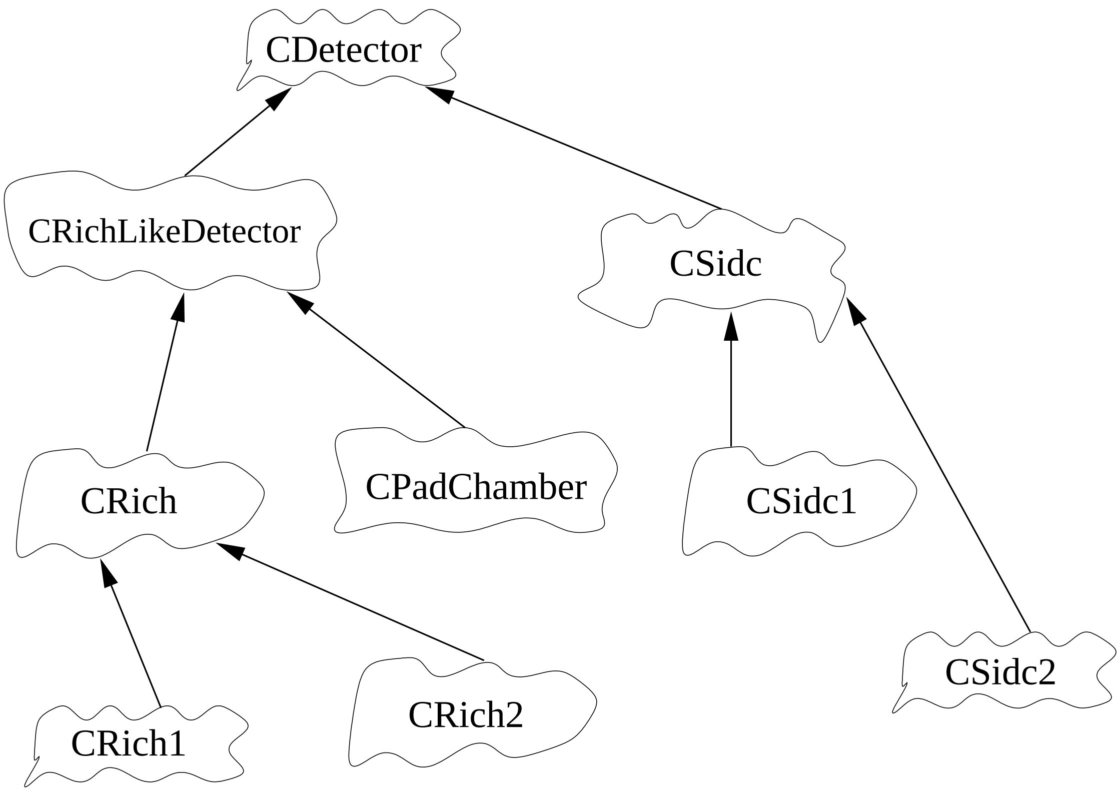

Figure 4.1: Inheritance tree of the CERES analysis

In C++ a class can be derived from a so called base class. The functionality and the data members of this base class can be used without any code being rewritten. Only data and functions needed for the special purpose are added. This principle is called *inheritance*. In the design of COOL it was applied very consistently. Figure 4.1 shows the inheritance tree of the CERES detector classes. CDetector provides for characteristics common to all detectors, like being able to draw itself, the existence of a name, id and raw data label. CRichlikeDetector contains unpacking of RAW data and the reconstruction of hits which the pad chamber and the RICHes have in common (see chapter 3). Since CRich1,CRich2 and CSidc1,CSidc2 differ only by small details, the actual definitions of these classes are extremely short as compared to CRich and CSidc. Here inheritance saves a huge amount of code copying.

4.3.2 Encapsulation

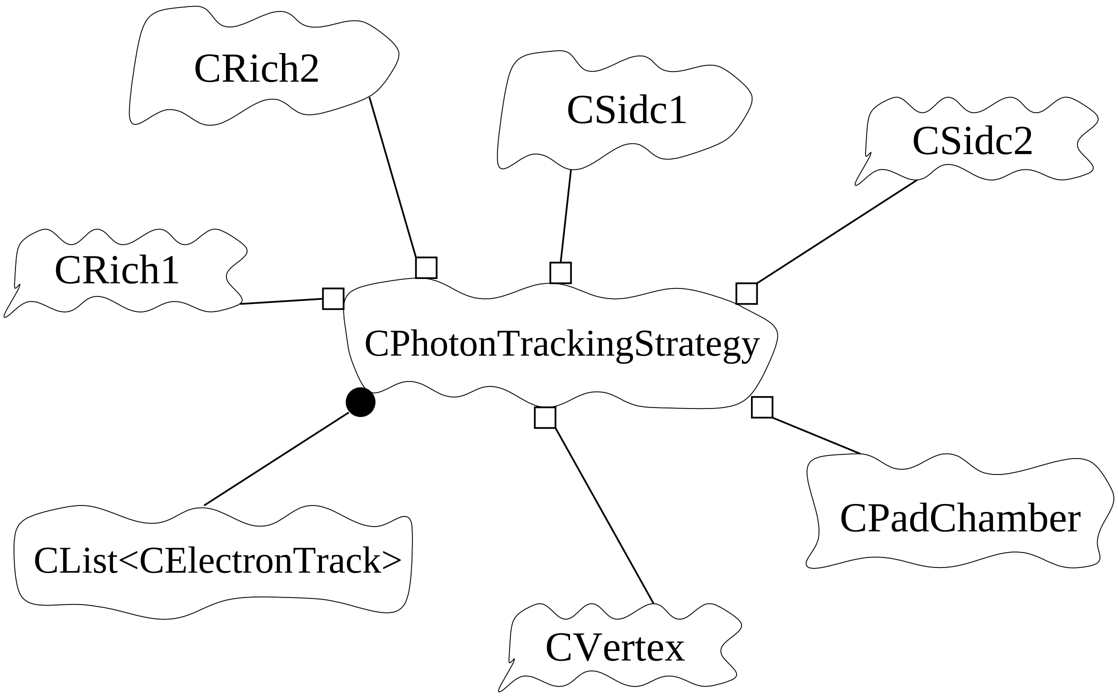

Figure 4.2: Tracking with all detectors

Variables or functions which are defined within a class declaration are called members. By declaring them *private* they can only be accessed from within the class, i.e. by so called member functions. Access from the outside is either completely forbidden, or, in the case of some data members, done via special access functions. This sharp definition of the channels by which the state of an object can be modified is called *encapsulation*. In the design and subsequent usage of COOL this was found to be an important measure to prevent the introduction of errors (bugs) and to facilitate the maintenance of the library. Figure 4.2 illustrates how, in some cases, one has to design carefully in order not to brake this rule. The tracking, i.e.

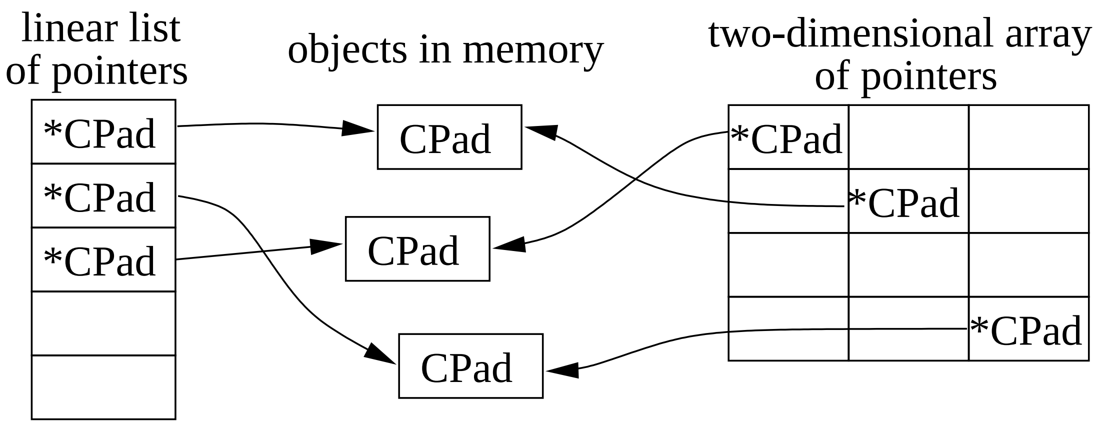

Figure 4.3: The CCollection class

the combination of all detector information to find electron trajectories, is done at the very end of the analysis chain. The tracking class needs access to all detectors. For visualization the detectors also need information about the tracks. Instead of making all information global (as with Fortran common-blocks) the tracking class holds only pointers to all the detectors and gets its information via access functions. Each detector holds a pointer to a list of tracks which can be set (attached) from the outside. In this way encapsulation is ensured and the mixing of previously well separated classes kept at a minimum.

4.3.3 Templates

A class operates on variables of a certain type. In C++ one can omit the specification of this type when declaring the class and rather do this only when an actual object (an instance) is created. One declares only a *template*.
The most common examples are lists of objects. The functionality of a list class is in most cases exactly the same, regardless of the type of objects which are stored. Figure 4.3 shows an example for a collection class with sophisticated functionality, the CCollection. Objects which reside in memory can be reached via a linear list or a two-dimensional array. Both ways of access are very common for UV-hits in the RICHes or cells (see chapter 5.1) in the SDDs. If an object is deleted, the collection class will take care of removing it from the list *as well* as from the array, thus completely eliminating a dangerous source of errors. By making this CCollection a template class, it had to be written only once and can be used for every type of object.

Chapter 5

From Raw Data to Conversion Pairs

The first step in the offline analysis is similar for all detector systems. The highly compressed raw data which is stored by the DAQ in a label structure (see 4.1) has to be unpacked. The result is a collection of primary detector information. In the case of the SDDs this means anode and FADC time-bin coordinates of so called cells, and for the RICHes and the pad chamber a collection of pad coordinates (x,y) and amplitudes (ADC-counts). For further processing, the different detectors require an individual treatment.

5.1 Hits in the SDDs

A hit in the SDD, i.e. the signature left by a MIP, typically contains some ten samples in time-bin direction and, due to the split anode structure, is spread over one to five anodes. Figure 5.1 shows an event display of SDD-2. A typical Pb-Au collision produces several hundred hits which amounts to some 10000 (anode,time-bin) coordinates (cells).
In a first step, cells which could possibly contribute to the same hit are collected by a so called *cluster* finder. Starting from the first coordinate-pair in the linear list of cells, all adjacent ones, which have either the same anode number or the same time-bin coordinate, and are not yet marked as belonging to a cluster, are appended, provided their amplitude value is above a certain threshold. Cells which are connected only by one edge will not be joined. For each of those added coordinate pairs the algorithm recursively calls itself and stops if no new neighbour-cell is found.
Within a reconstructed cluster, adjacent time-bins above readout threshold are

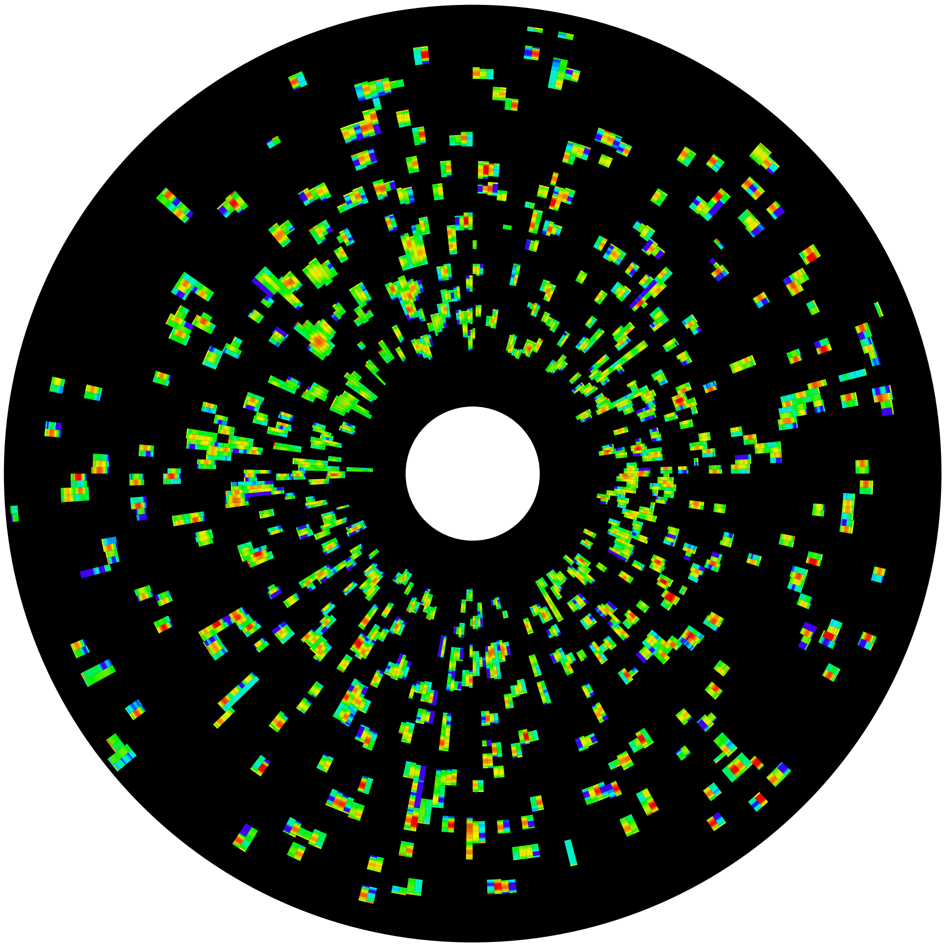

Figure 5.1: Event display of SDD-2. The amplitude values are coded by a grey-scale.

connected to *pulses* and their center calculated as the maximum of a gaussian regression to the amplitude-time-bin distribution. Pulses on adjacent anodes with centers differing by less than one time-bin are then connected to one hit. The hit center in azimuthal direction is calculated as the center of gravity of the contributing pulses.

A problem arises, if some cells in a pulse have an amplitude beyond the sampling range of the FADC. By simply adding the sampled amplitudes, the part of the signal above the saturation limit is omitted (figure 5.2). For the amplification used during the 1996 photon run, 5% of the pulses produced by a single MIP reach saturation amplitude. For a double dE/dx signal of two MIPs, the signature of a converted photon, this fraction grows to more than 20%. Important information is lost. With the method of gaussian regression, a more precise determination of the pulse position, and especially of its integral amplitude is achieved in those cases.

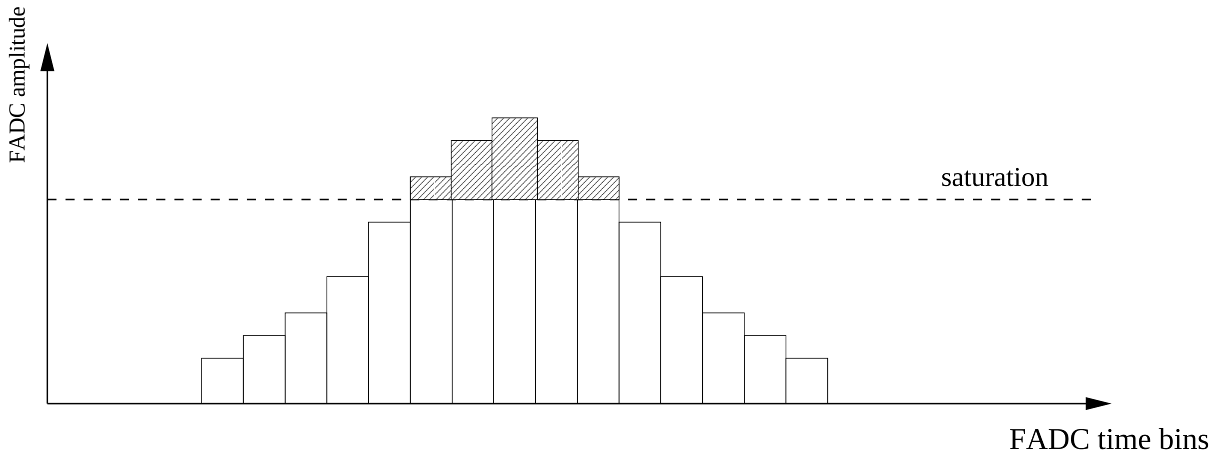

Figure 5.2: An SDD Pulse in saturation. Simple amplitude counting omits signal above threshold (hatched). The area of a gaussian fit gives a better approximation.

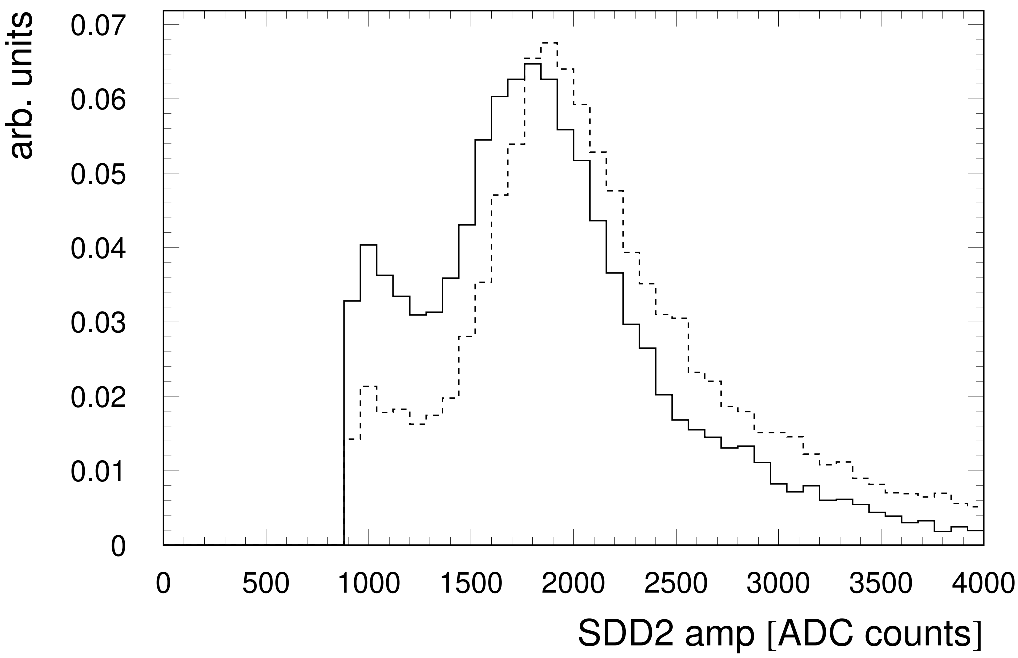

Figure 5.3: Hit amplitudes in SDD-2. The solid line shows the distribution for a simple summation of cell ADC-counts in each pulse. The dashed line represents the amplitude calculated from the gaussian regression to the pulse. The shift of the rising edge towards higher amplitudes means a higher efficiency for the conversion selection.

The improvement is illustrated in figure 5.3.
Once the hits are identified, their positions in anode and time-bin have to be translated into the detector coordinate system. For the azimuthal angle this means simply a rotation by a constant. The radial coordinate is obtained assuming a linear relation of radius and drift-time, i.e. a constant drift velocity. We will see later-on that second-order corrections to this assumption have to be made.
Diffusion widens the charge distribution in azimuthal and radial direction with time, thus increasing the rise time of the pulse. This leads to an attenuation of the signal by the shaping amplifier, the *ballistic deficit*. Since the hit amplitude, the dE/dx, is such a crucial quantity for the identification of photon conversions, this effect has to be corrected.

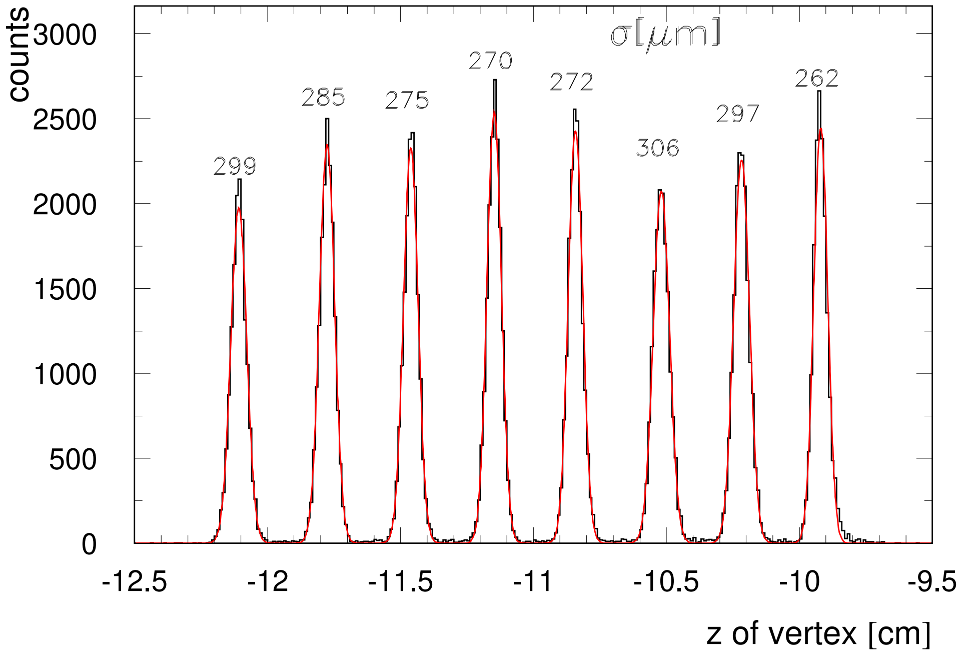

Figure 5.4: Fitted z-coordinate of the vertex, overlaying all runs. The width(σ) of the gaussian fit to each vertex disc is indicated in the plot.

5.2 Vertex Reconstruction

Once all hits in the SDDs have been found and their positions calculated in laboratory coordinates, they can be used to reconstruct the exact location of the Pb-Au collision, the *vertex position*. The most simple method to do this is to minimize the quadratic sum of hit mismatches between the two SDDs by iterating an assumed vertex position. The procedure is extremely time-consuming and has therefore been replaced by a robust fitting method, implemented by the end of 1995 [37]. Hereby all hits (within sensible windows) of SDD-1 and SDD-2 are combined to straight track segments and the weighted sum of all their projected distances to an assumed vertex position is calculated. In the next iteration this center of gravity becomes the new assumed vertex and each segment gets a new weight, according to it's deviation from the mean-value in the step before. The procedure converges on average after five iterations and is with some 50ms running time (on a SUN

HyperSPARC workstation) more than 20 times faster than the old fitting method. Figure 5.4 shows a distribution of vertex z-positions obtained with the robust fitting. The average scattering around the (25 μm) target discs is 280 μm using hit positions calculated after a careful calibration of the whole spectrometer (see chapter 5.6).

5.3 Hits in the RICH-like Detectors

Since the pad-readout of the two RICHes and the pad chamber is very similar, the same software is used for all three. In a first step, adjacent pads are connected to *clusters*. Adjacent, in this context, means that one coordinate on the two-dimensional pad-plane must be identical. Pads which are connected only by their edges are not joined to the cluster. In the such created list of clusters, background signals from various sources are identified and removed. Omitting this step would cause a serious problem for the pattern recognition of rings. On the other hand, some genuine photon-hits will be removed by the cleanup, which also causes a loss of efficiency. The procedure outlined below is carefully tuned to find the best compromise.

- Electronic noise can raise the signal of single pads above the readout threshold. Removing clusters which consist of only one pad takes care of this. Since, however, real UV-hits with small amplitude have the same signature, a loss of efficiency is inevitable. The effect was kept at a minimum by adjusting the amplification of the UV-detectors sufficiently high.

- Fluctuation of the pedestal-value in an entire PCB-board of readout channels (modules). This problem is easily removed due to the unique geometrical shape of a rectangle.

- Ionizing particles which traverse the UV-detectors produce very big clusters which, in their center, mostly saturate the amplitude range of the ADCs. Great care has to be taken in removing this, because the signature of several photon hits connected to each other is very similar. This type of cluster is removed if

  - it is very big indeed ($>$ 200 pads),
  - it looks like an ionization track (long and thin),
  - the amount of saturated pads is unusually large ($>$ 6),

  and in some sub-cases of those mentioned above.

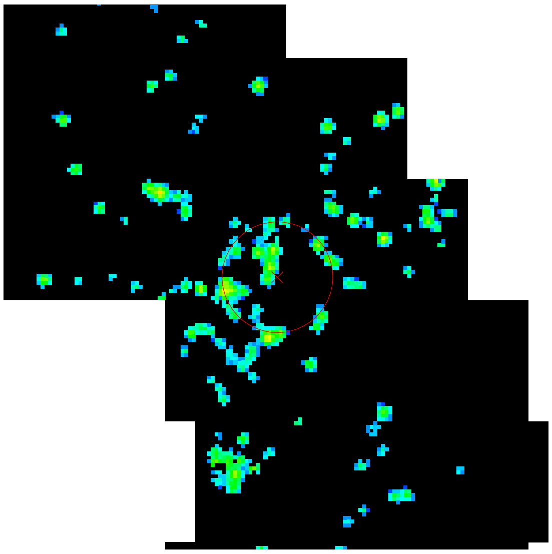

Figure 5.5: Event display of RICH-1, selected from the final photon sample. The solid circle indicates the fitted position of a (double) ring produced by an electron and a positron. The matching rings, opened up in the magnetic field can be seen in the RICH-2 display below. From these pictures one also gets an idea of the difficulties the large background causes for pattern recognition.

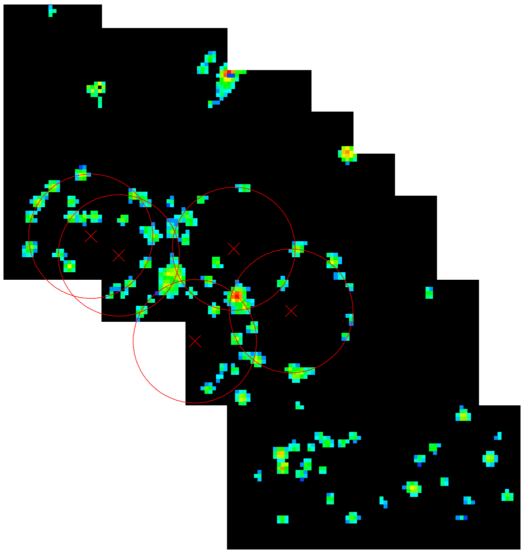

Figure 5.6: Event display of RICH-2, selected from the final photon sample. The two solid circles closest to the outer rim are the rings of the electron and positron after their tracks are separated by the magnetic field.

The remaining clusters are then split. Each local maximum and the surrounding pads are identified as hit of a UV-photon in the RICHes and of an ionizing particle in the pad-chamber.

5.4 Rings in the RICHes

Figures 5.5 and 5.6 show an example of electron-rings in the RICHes.
The ring reconstruction is done in three steps:

- Pattern recognition is performed in the RICHes only. This is done by a point to ring Hough-transformation. Around each photon hit a ring with asymptotic radius is created in the transformed plain. The intersection of those rings indicates the center of the electron ring in the original pad-plain. The double-Hough-transformation used for this analysis has been described for the example of pion-rings in [28]. The result is a list of ring *candidates*.

- Background (fake) rings are rejected by matching to the tracking detectors. For RICH-1 all candidates must have a corresponding track segment (see 5.5) in the target telescope. The match requirement is set to a generous 4σ to minimize the efficiency loss in this stage. The filtering for RICH-2 is more complicated, due to the deflection in the magnetic field. All kinematically desirable (see 5.5) combinations of candidates in the two RICHes are used to calculate a predicted point in the pad-chamber. Again using a sufficiently generous match criterion, only those candidates are kept in the list for which a corresponding pad-chamber hit was found.

- All surviving candidates get their final center-coordinates and radii by a robust χ^2 fit. The function minimized is a modified χ^2 where the fit-potential varies in a gaussian way (instead of quadratically) with the distance to the minimum. See [3] for an extensive description of the fitting algorithm.

5.5 Electron Tracks

Once all data has been processed into physically meaningful information, i.e. hits of minimum ionizing particles in the tracking detectors and electron rings in the RICHes, complete particle trajectories can be reconstructed. In describing this, we shall keep the chronological order of the analysis program.
The first step are track segments in the target telescope. Since the target region is essentially free of magnetic field, tracks are straight lines. By default all hits in SDD-2 form, together with the fitted event vertex, such a segment. With this

information a predicted position in SDD-1 is calculated and a fast search algorithm looks for the closest hit in SDD-1 which is then associated to the track data-structure. The next closest hit is also memorized.
The magnetic field between the two RICHes deflects a trajectory in azimuthal (Φ) direction, whereas the polar angle (Θ) is preserved. Track candidates in the RICHes, therefore, are formed by rings with equal Θ-coordinate, considering a maximum $\Delta\Phi$ dictated by a chosen lower momentum cutoff (see equation 3.5), in this case a transverse momentum ($p_\perp$) of at least 50 MeV/c. The matching quality in Θ depends on the amount of multiple scattering a particle suffers when traversing the spectrometer and therefore on the momentum itself. In second order, one observes also a deflection in Θ due to the magnetic field. The resulting window in (Θ,Φ) has a shape which is commonly referred to as *butterfly*. See [3] for a more detailed description. Rings matching within this window are considered as track candidates. A ring in RICH-2 can contribute only to one track, whereas a ring in the first RICH can be used twice, provided the two tracks formed in this way have opposite charge-sign (photon conversion). Ambiguities are resolved by the choice of combinations with smaller $\Delta\Theta$, favouring those which have a matching hit in the pad-chamber. For each ring associated with the track, the next closest in the same detector is also memorized.
In the end, for all the so found ring combinations, the in Θ and Φ best matching track segment in the silicon drift detectors is selected and the result is a complete electron track.

5.6 Intercalibration of Detectors

For the reconstruction of electron tracks the positions of all detectors with respect to each other must be known with sufficient precision. In the very first steps of data analysis this is ensured by using a best guess. Externally measured distances and locations are used for the RICHes and the pad-chamber. The silicon drift detectors are aligned in the software by using visualization tools and by trying to match patterns in the two detectors which obviously have the same physical origin, i.e. a trajectory of some particle. Once it is possible to fit the event vertex and reconstruct complete tracks, further calibration can be done by using the data itself. With a sample of reconstructed pions [26], matching distributions can be accumulated with high statistics and small misalignments can be corrected in an iterative procedure. The level of precision is in the sub-milliradian range for all detector matches. To ensure a clean sample of electron tracks, purely coincidental detector combinations (fake tracks) must be suppressed. This is mainly done by matching-cuts. Although tracks can be identified even with much less accuracy, a high level of calibration is desirable to reduce the efficiency loss and at the same time get a maximum suppression of those fake tracks.

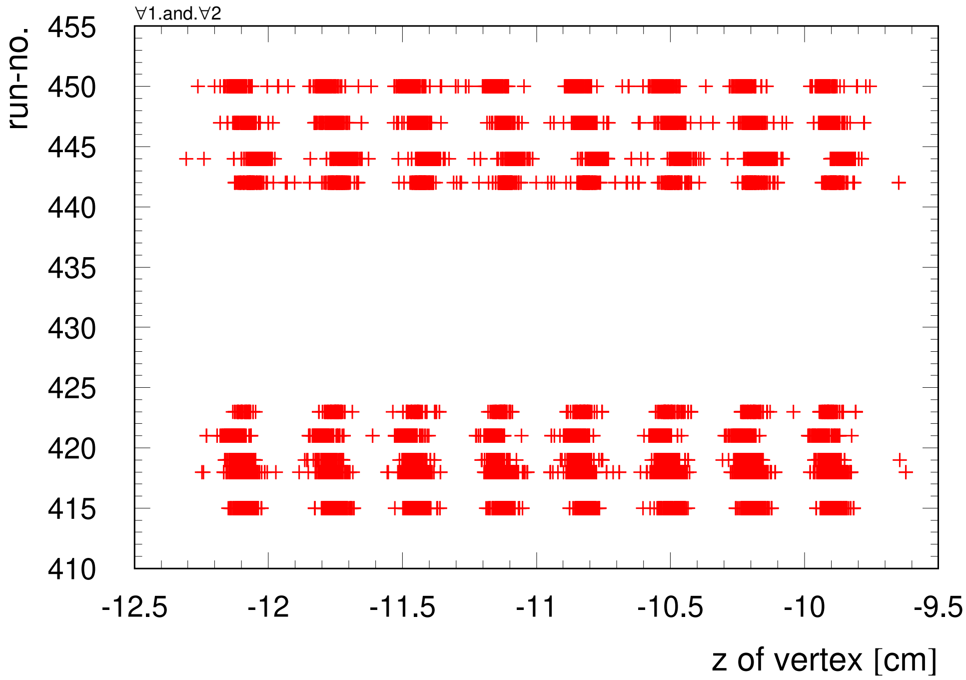

Figure 5.7: Z-position of the vertex versus run-number before time dependent calibration of the drift velocity.

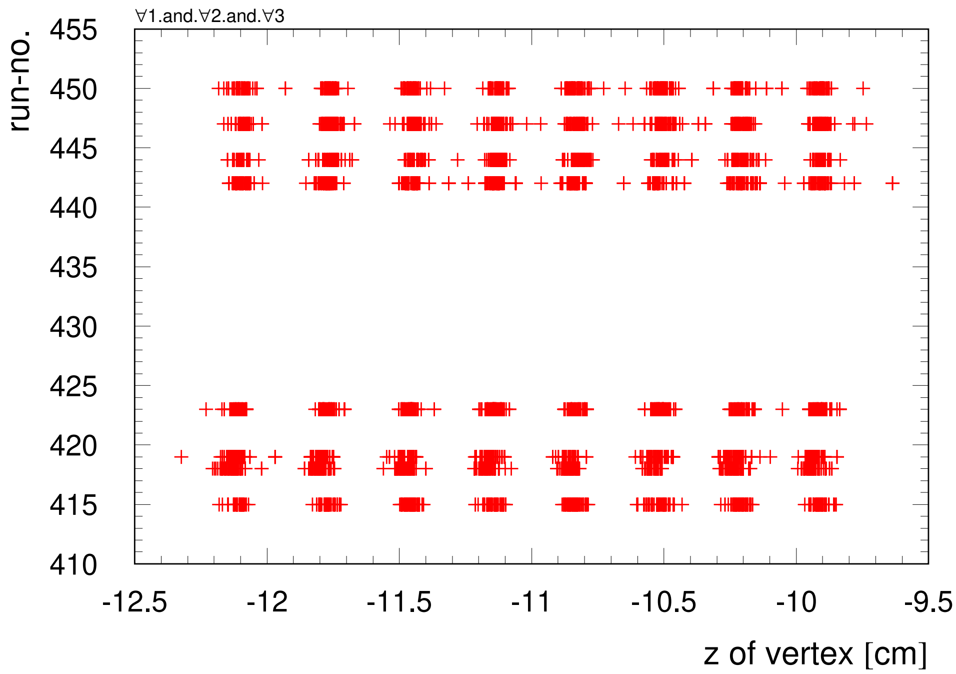

Figure 5.8: Z-position of the vertex versus run-number after time dependent calibration of the drift velocity.

The calibration of the silicon drift detectors depends also on time. Small changes in temperature (some 0.1°C) affect the mobility of the drifting charge such that, using a constant drift velocity, reconstructed hits can shift by some 100μm. This causes an error of up to 1 mrad in the match to the other detectors. With an automatic procedure, the drift velocity is adjusted for each processed data file which resembles about one hour of data taking. By preprocessing 1000 events a drift-time spectrum of SDD hits is accumulated. With a fit to the upper edge (close to the anodes) of the spectrum, the maximum drift time is determined and the change in drift velocity with respect to some reference calculated. Figures 5.7 and 5.8 show the effect of the procedure on the fitted z-position of the event vertex. Before calibration the fluctuations with run-number are as large as 1 mm. This is reduced to less than 100 μm after the correction of the drift velocity.

5.7 Recognition of Photons

In the final step of data processing tracks are combined to e^+e^--pairs. For the photon analysis only those combinations are considered which have a conversion signature as illustrated in figure 5.9. In this stage all track segments reconstructed in the target telescope are used regardless if there is a hit in the first SDD. A minimum amplitude of 1100 ADC-counts is required in the second drift detector. Such a segment must match to a ring in RICH-1. Whereas the open pair analysis requires at least five photon hits on this ring, here the minimum is set to seven. This favours double rings already in the first stage of photon recognition. The combination of ring and hits must match to two rings in RICH-2. At the extrapolated positions in the pad-chamber matching hits must also be found. With these constraints a photon candidate is found only in one of seven multiplicity triggered events. All information is stored in an n-tuple format with some 300 variables for each reconstructed pair. The overall data volume is reduced by a factor of 50. The compressed data set contains also photon conversions in the target. They are kept at this stage for systematic studies and are removed by the final cuts.

The following constraints ensure a clean sample of conversions from between the two SDDs (converter signature):

- The most powerful cut for conversion recognition is that on the energy loss (dE/dx) in the second silicon drift detector. In some cases the hit reconstruction does not manage to associate all information of the two MIPs to one hit. This is due to deficiencies of the reconstructing algorithm, the so called artificial hit splitting. The problem is solved by using the sum amplitude of the hit associated to the track and the next closest hit, if the distance between the two is small enough. The problem is illustrated in figure 5.10. The circle

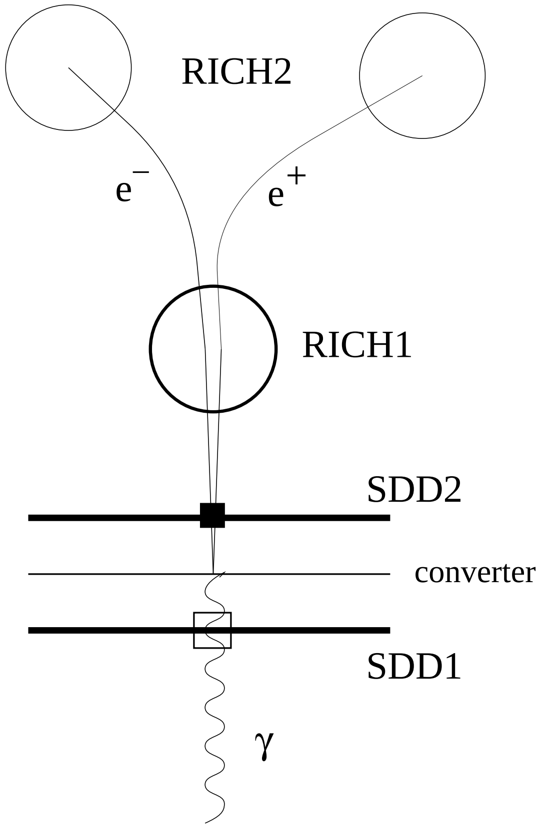

Figure 5.9: Schematic signature of a photon conversion. Two rings in the second RICH match to one (double) ring in RICH-1 and to a track segment in the SDDs. For the final sample of photons converted *between* the two SDDs, a signal of two MIPs is required in the second drift detector and no matching hit at all must be found in the first SDD.

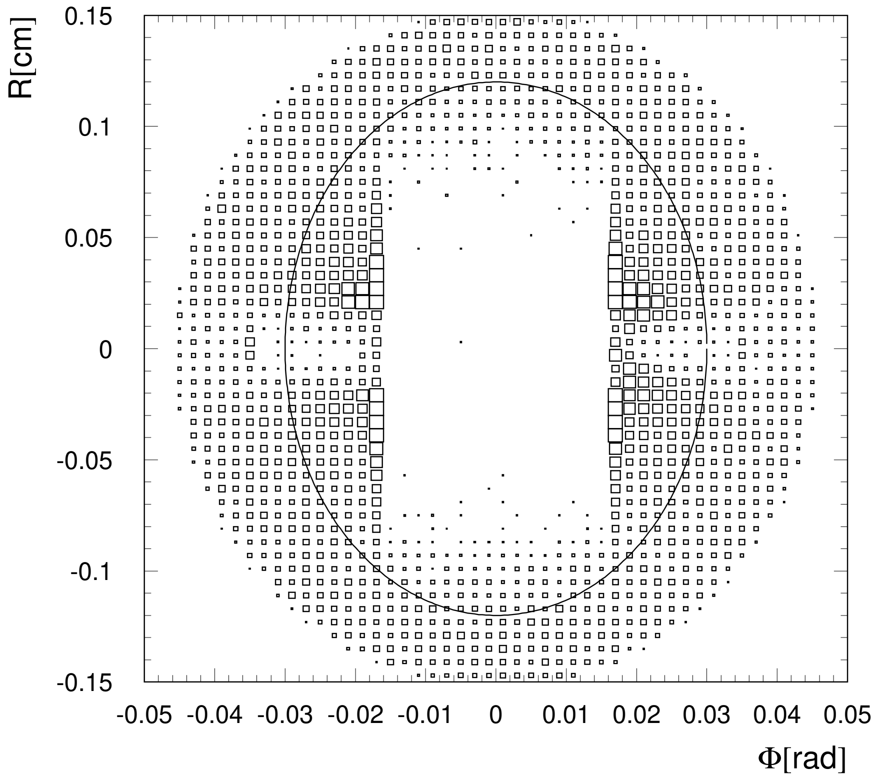

Figure 5.10: Distances between neighbouring hits in SDD-2. The rectangular gap indicates the limit of double-hit resolution.

indicates the maximum allowed distance for hits to be summed. Only those conversions pass this step which have a sum-amplitude of more than 1400 ADC-counts.

- A minimum of 11 photon-hits is required to further reject rings in RICH-1 which may not be genuine double rings. Also the sum of all amplitudes of photon hits which where used for the ring-fit must be more than 1000 ADC-counts. Both cuts fulfill the same purpose and are largely correlated. The number of hits is to first order independent of variations of the amplification in the UV-detectors. For the amplitude, however, this is not the case. Such *gain variations* as a function of time and of (x,y)-position on the readout plane (figure 5.11) must be known and corrected for. For this purpose a gain-map is constructed which contains for each of the 54000 pads a mean amplitude. In the sum, all hit amplitudes are weighted with the deviation from the mean. Fluctuations in time are treated in a similar way, using the mean gain over all pads for one run.

- Most of the conversions which occurred before (or inside) SDD-1 are now removed by the requirement of *no* matching hit in the first silicon drift detector. The size of the veto window is 300μm in radial and 15 mrad in azimuthal direction. The rejection power of this cut is shown in figure 5.12. The circle

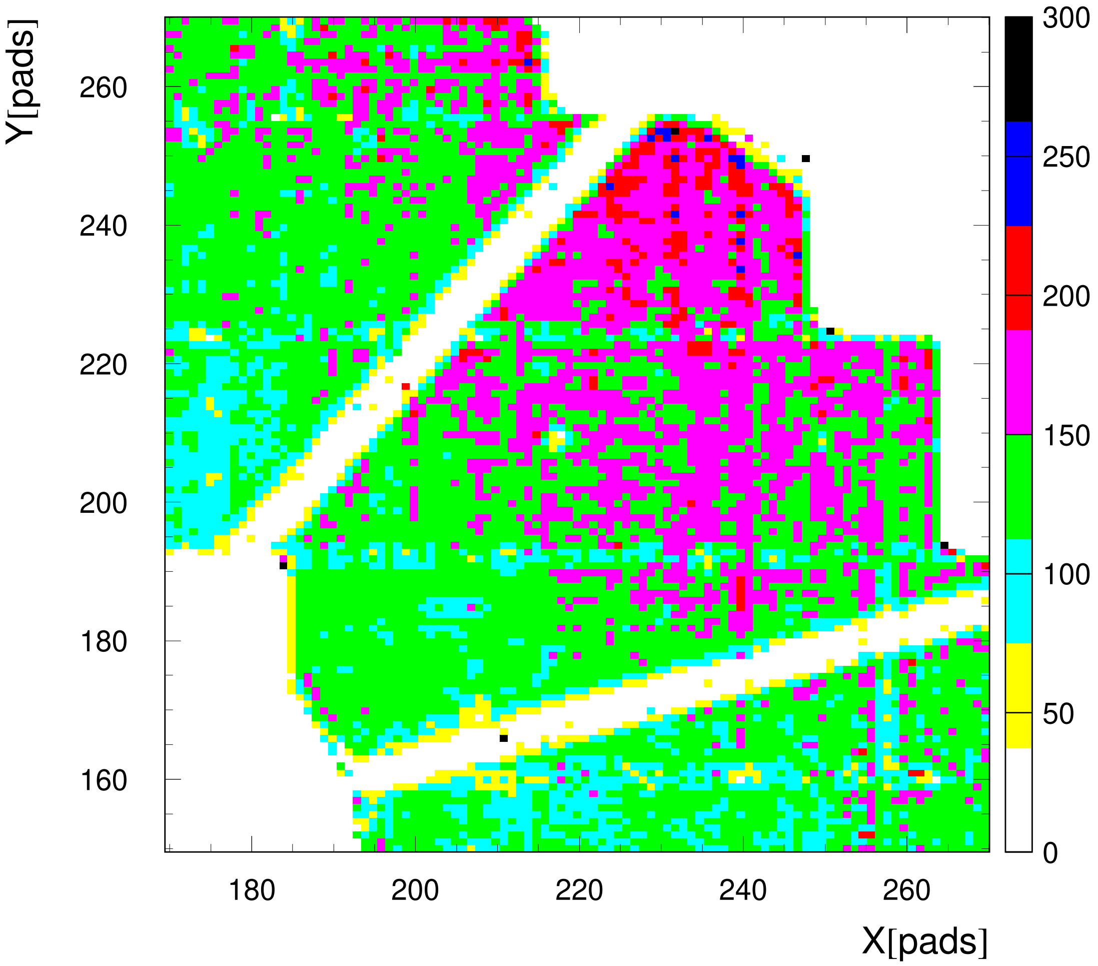

Figure 5.11: Gain variations in RICH-1, shown for one high-voltage sector in the upper right corner of the detector. The grey-scale corresponds to a mean amplitude. Variations of 50% are observed and must be corrected for.

indicates the region of double dE/dx (a hit of two MIPs) in both detectors. Here one finds most of the conversions in the target. Without any additional cut on the amplitude this signal completely disappears, once the mismatch-cut is applied. The remaining contamination of target conversions is due to inefficiencies in SDD-1. Since, however, the regions of dead anodes (the main inefficiencies) are completely removed from the analysis, this contribution is below 5%. It is simulated by the Monte-Carlo and thus enters the systematic error only as a second order effect.

The final sample after all cuts contains 34000 photon conversions with the converter signature. Figure 5.13 shows the transverse momentum distribution without any corrections. To get an absolutely normalized p$\perp$-spectrum, the spectrometer effects

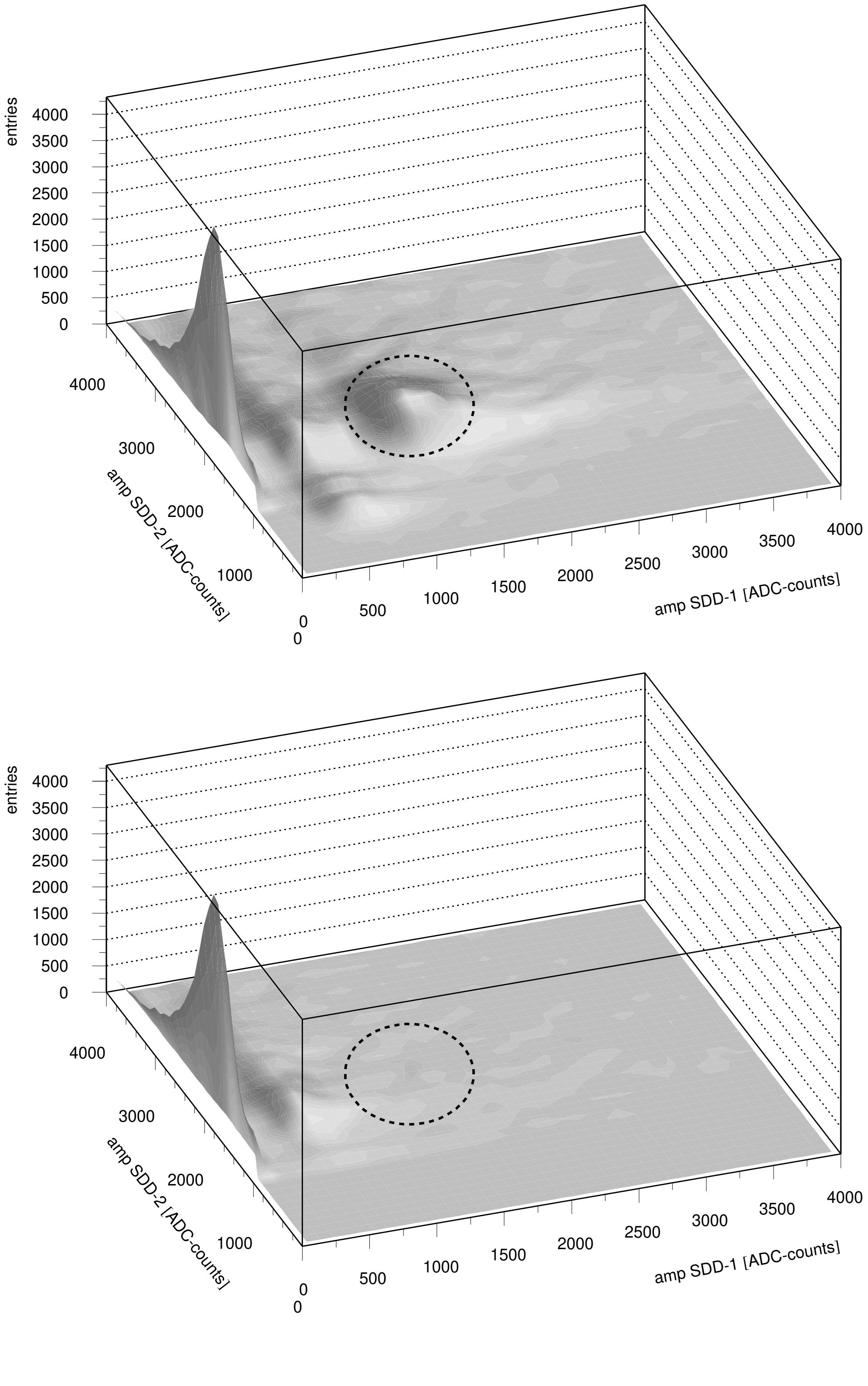

Figure 5.12: Rejection power of the SDD-1 mismatch cut.

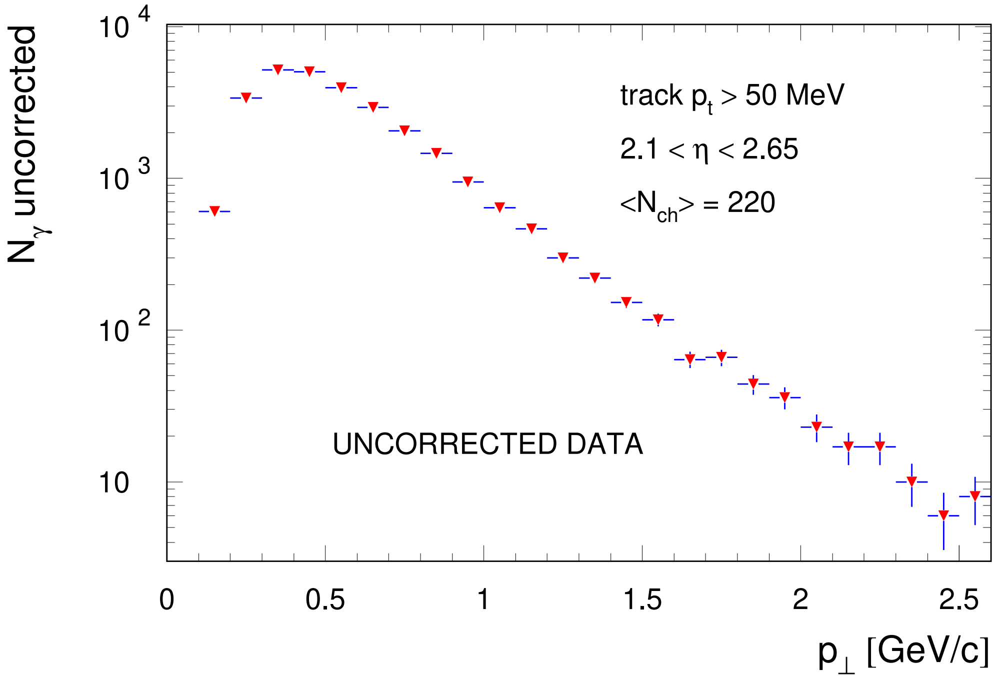

Figure 5.13: Uncorrected transverse momentum distribution of photons.

like acceptance, efficiency, and conversion length must be corrected for. The Monte-Carlo simulation used for this shall be explained in the next chapter.

Chapter 6

Monte-Carlo

The aim of this analysis is to measure a cross-section - the absolute number of photons in one event. Therefore all detector effects like limited geometrical acceptance, tracking efficiency, finite momentum resolution, and the probability for photon conversions, have to be known and corrected for. To get all this information a Monte-Carlo simulation of the complete spectrometer is implemented.
Since a full description of a heavy ion reaction including all sources of background did not succeed so far and would, in any case, consume a tremendous amount of CPU time, the simulation is done using a *Monte-Carlo overlay* technique. What this is and how it is realized shall be explained in the following paragraphs.

6.1 The Monte-Carlo Production Chain

The spectrometer efficiency and the conversion length strongly depend on the polar angle Θ and the azimuthal angle Φ of a particle trajectory. The simulation input must therefore show the same distributions as real data. The best guess for this (a priori unknown) data is the hadron-decay generator (see chapter 7).
The produced photons are passed through the spectrometer simulation. Every piece of material and all sensitive detectors are implemented in a GEANT [34] environment. The program calculates the path of the initial and all subsequently produced particles through the experiment. Multiple scattering with its dependence on momentum, photon conversion, and deflection in the magnetic field, as well as all signals in the particle detectors are simulated. Only photons which converted into an e^+e^--pair are stored as raw Monte-Carlo output.
The output of GEANT is then used as a parallel input stream for the standard analysis program. The Monte-Carlo information of one photon conversion is processed into a set of anode and time-bin coordinates in the SDDs or pad (x,y) coordinates in the RICH-like detectors and then added to the event's raw data. From there

on all processing is done in exactly the same way as for real data. With each reconstructed photon, the original Monte-Carlo information is stored in addition to the standard set of analysis results. By counting reconstructed versus all overlaid photons, the efficiency can be extracted differentially in transverse momentum or charged particle multiplicity or any other quantity characterizing the track.

6.2 Spectrometer Simulation for the Photon Run

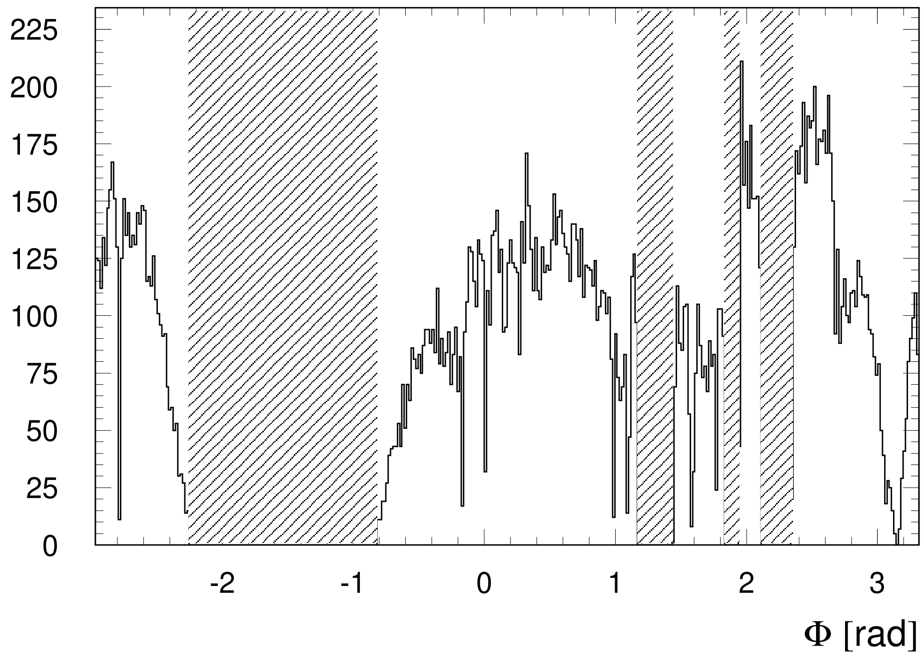

Figure 6.1: Φ - distribution of conversions in the target. The hatched areas show dead regions of the spectrometer. The biggest defect is due to a non operational high-voltage sector in the pad-chamber, the others are caused by dead anodes in the two SDDs.

Figure 6.1 shows a distribution of the azimuthal angle at which conversions in the target could be reconstructed. Since, in contrast to the more complicated Φ-structure of the converter (see chapter 3.3), the target is azimuthally symmetric, this can be used to point out the strong dependence of reconstruction efficiency and spectrometer acceptance on Φ. All detector properties and defects which contribute to this must be simulated with best possible precision.
Part of the identification of a photon signal from the converter is the requirement of **no** matching hit in SDD-1. Due to inefficiencies of the first SDD, one has to expect a certain fraction of target-conversions in the final sample. This should also

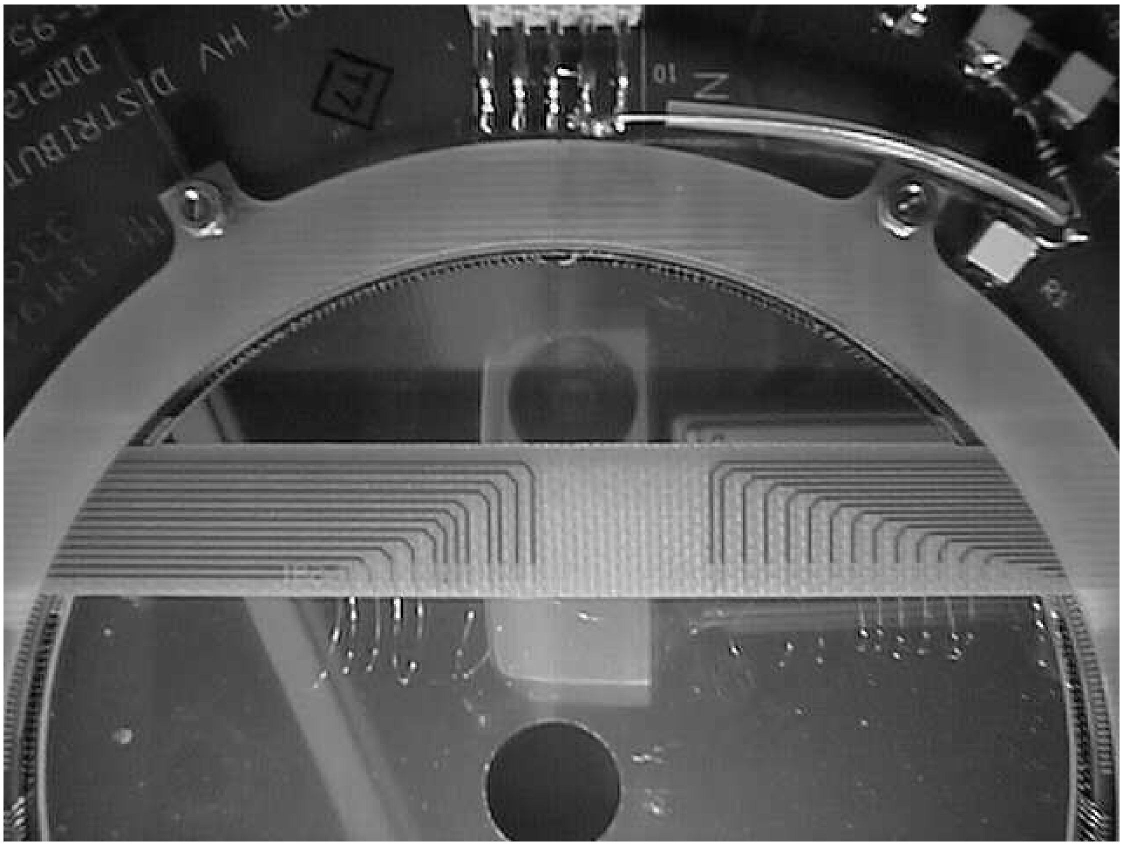

Figure 6.2: SDD HV-bridge N-side

be correctly simulated by the Monte-Carlo. To do this, the amount of material at each track angle must be known.
To supply the silicon wafers with high voltage, the mother-boards of the SDDs are fitted with *high-voltage bridges.* Their structure, essentially glass-fiber epoxy (FR4) with Cu conductors, is shown in figures 6.2 and 6.3. Due to the location of dead areas, they contribute some 30% to the overall conversion-length (X/X_0). The structure of the Cu conductors contributes up to 10% locally and must also be implemented with its exact geometry.

6.3 Tuning of Detector Responses

To get the correct efficiencies and momentum resolution, the Monte-Carlo must resemble the data in all details. An inaccurate description of the match between detectors and of the hit amplitudes has a direct impact, since in the analysis cuts

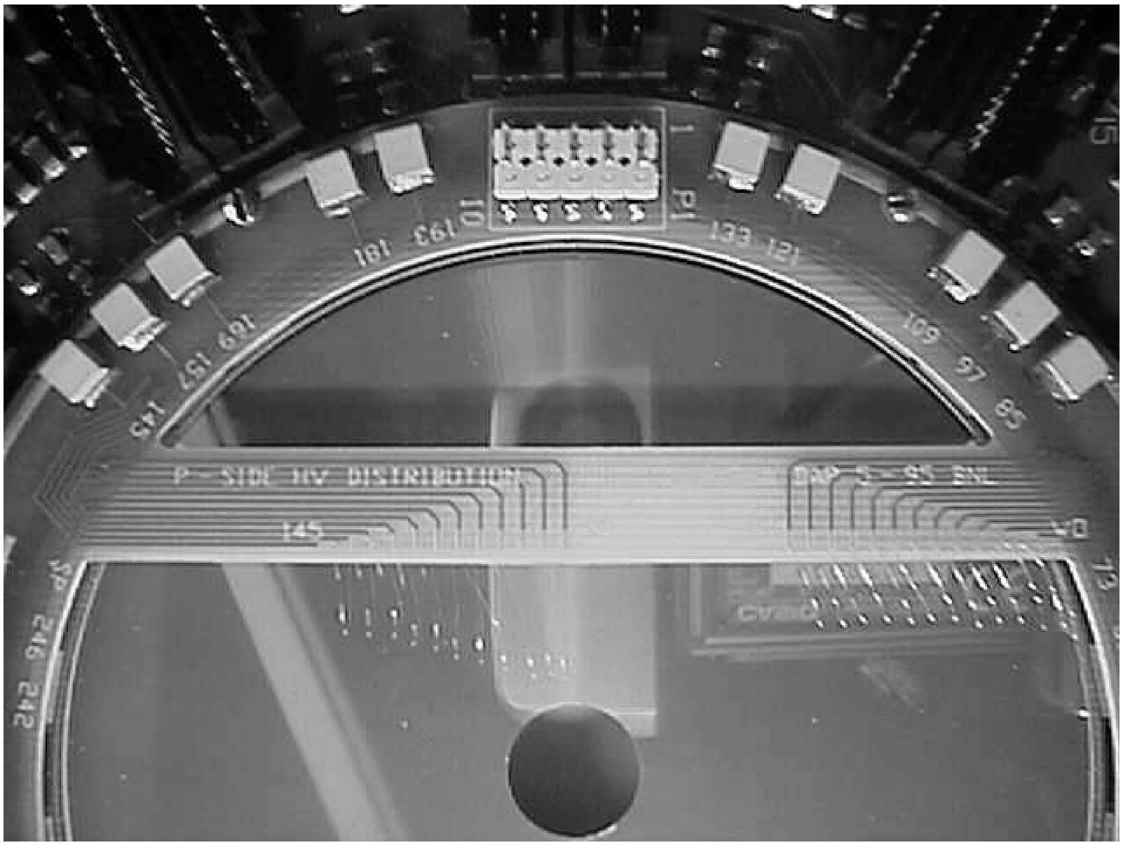

Figure 6.3: SDD HV-bridge P-side

are applied on these quantities. A correction of the distribution themselves, e.g. by random smearing, would cure only the most obvious part of the problem.
The matching quality which is observed in the Monte-Carlo simulation is the result of a modulation of all the physics processes and electronic signal processing which in the end leads to raw-data like detector responses. A very detailed description of all the effects can be found in [27]. If one of those fundamental simulations is done incorrectly, that is, not completely resembling the real world, one can see the effect in the distributions of detector-matches and amplitudes, but one also has to assume the accompanying efficiencies for the pattern recognition of ČErenkov rings and the reconstruction of hits to be inaccurate.
For this reason all low-level parameters like amplification of the SDD pre-amplifiers, or smearing of photon-hits in the UV-detectors due to non-ideal mirror quality, to name only few, have to be correct. In general they are taken by first principles [27]. Within their uncertainties they are then tuned to decribe the data. Only in two cases additional smearing had to be applied. One is the vertex-position, which has an accuracy of 30 μm in the (x,y)-plane in the simulation. An additional

30 μm has to be added here. Another case is the ring-center resolution of RICH-1. The Monte-Carlo prediction is correct, if one measures this quantity in the data via the radial scattering of hits on the ring. The match to the other detectors, however, is considerably worse. This is a long standing problem of CERES and, though studied extensively, up to the present not understood. It is accounted for by explicitly adding an uncertainty of 0.88 mrad to the ring-center position. The correctness is finally checked by comparing width of hits, ring center resolution and also in the end the matching distributions with those obtained from data. Figure 6.4 shows a selection of detector matches from data (dots) and simulation (histogram line). For almost all distributions, there is apparently no discrepancy. An exeption is seen only in Δx between RICH-2 and the pad-chamber. The impact of this on the systematic error shall be discussed along with the analysis results in chapter 8.
The amplitudes relevant for the analysis are shown in figure 6.5. Cut values used in the data are a minimum of 1400 ADC-counts for hits in SDD-2, more than 1000 ADC-counts for the sum-amplitude and at least 11 photon-hits on rings in RICH-1. The deviation of hit amplitudes below the cuts are due to different event types selected in data and Monte-Carlo. The data sample at the stage when these plots where produced still contained a selection of target-conversions and e^+e^--pairs from dalitz decays kept for systematic studies. In the simulation only photons are considered which convert in the relevant zone, that is before the second silicon drift detector.
The final distributions in polar and azimuthal angle (figure 6.6) show generally good agreement. The decreasing efficiency at the edges of dead areas as well as single dead anodes are correctly simulated. A deficiency in the description of the overall conversion length in the GEANT implementation leads to the partly observed disagreement in photon yield versus Φ. Since the Monte-Carlo simulation is used for efficiency determination including an estimate of the remaining fraction of target conversions in the final sample, but is not used for determination of the conversion length, the error generated by this mismatch is only a second order effect.
The conversion length itself is determined in a more precise way including a study of the systematic error by a seperate method described in the following paragraph.

6.4 The overall conversion length

Out of 500000 produced Monte-Carlo events, 26000 photons which converted between the two SDDs are reconstructed by the analysis program and pass all selection cuts. The statistical significance of this sample (compared to 34000 photons from data) is good enough. The differential efficiencies which are used to correct the data are obtained by fitting the distributions of efficiency versus transverse

Material and Location	thickness	substance	$\%X/X_0$	target relevant	converter relevant
target-discs	12.5μm	Au	0.377	X	
space before SDD-1	11cm	Air	0.03	X	
HV-bridge before SDD-1	0.5mm	G10-PCB	0.256	X	
SDD-1 wafer	0.28mm	silicon	0.27		
HV-bridge after SDD-1	0.5mm	G10-PCB	0.256		X
steel converter	0.1mm	Fe	0.568		X
HV-bridge before SDD-2	0.5mm	G10-PCB	0.256		X
SDD-2 wafer	0.28mm	silicon	0.27		
conductor on HV-bridges	17μm	Cu	0.119	(X)	(X)
sum before SDD-1			0.472	X	
sum between SDDs			0.922		X

Table 6.1: Materials relevant for photon conversions. The last two collumns indicate, whether this item contributes to the conversion length *before* SDD-1 (target-like conversions) or *between* the two SDDs (converter-like conversions). The Cu-conductor is summarized only as one item, as its structure is complicated. Note that the total X/X_0 before and between the SDDs is obtained by the simulation method described in this chapter and not simply by summing the single contributions.

momentum, or versus charged particle multiplicity. In this way the remaining statistical fluctuations are smoothed. Since processing of this sample already consumed more than one week CPU-time on the ten available HP-735 computers, it is not possible to do many iterations for systematic studies. For this reason a different approach is chosen to determine the relevant conversion length and study its systematic uncertainties.

A large number (several millions) of tracks is randomly generated within the spectrometer acceptance. The azimuthal angle is chosen from a white distribution, wheras the polar angle is generated according to a gaussian shape in pseudorapidity with center at $\eta_0 = 3$ and width $\sigma_\eta = 1.4$, taken from a measurement by the NA49 collaboration [42]. For each point where this assumed particle crosses material between the two silicon drift detecors, the conversion length (see summary in table 6.1) is calculated and summed. An entry then is made in a histogram versus the generated azimuthal angle using as a weight the total conversion probability. The result is shown in figure 6.7. In the upper plot one immediately sees that the so beautifully simple shape expected from the geometry of the steel converter, i.e. a repeated pattern of zero, single and double conversion length of 100μm of steel, is strongly obstructed by the additional material. The residual at zero converter thickness is due to the PVC foil which was used as a support for the steel discs. The structures which are not locally constant in Φ but more or less linear rising

and falling are the effects of the high-voltage bridges and their complicated shape of copper conductors. In the lower plot a cut is made on the regions of the spectrometer which are known to be non-functional. The largest dead area is due to a completely missing high voltage sector in the pad-chamber, the three smaller regions stem from dead anodes in either the first or the second silicon drift detector. Together they reduce the spectrometer acceptance to 66.91 % of $2{\cdot}\pi$.
The conversion length for the remaining active area is found to be $(0.922{\pm}0.024)$ %. Since the satistical significance of this study can be regarded as infinite, the error is purely systematical. The way in which it is determined is described along with the other systematic errors in chapter 8.

6.5 Monte-Carlo correction of Nch

The number of charged particles (Nch) in one unit of rapidity is measured by simply counting all track-segments reconstructed in the target telescope within the chosen range of pseudo-rapidity. In principle, the Monte-Carlo can also be used to calculate the efficiency of this method as a function of Nch. For this purpose a first attempt of a full event simulation is done. Different numbers of charged pions are generated, randomly distributed in Φ and Θ in the same way as for the determination of X/X_0 in the previous section. They are all processed through the GEANT simulation and the analysis chain without any overlay of real events. The number of reconstructed versus that of simulated pions gives a correction function for the Nch measurement. It is found to be

$$Nch_{true} = Nch_{meas} \cdot (1.035 + 0.00045 \cdot Nch_{meas}) \quad . \tag{6.1}$$

The problem of this procedure is that the systematic error is extremely difficult to estimate. The Monte-Carlo is relied upon, not only for calculation of tracking efficiency, but also for correct simulation of pile-up effects, that is, obstruction of the hit reconstruction by high particle density. Up to now, no reliable method has been found to judge the precision of this correction. We will see in chapter 8 how this problem is overcome for the absolute normalization of the data.

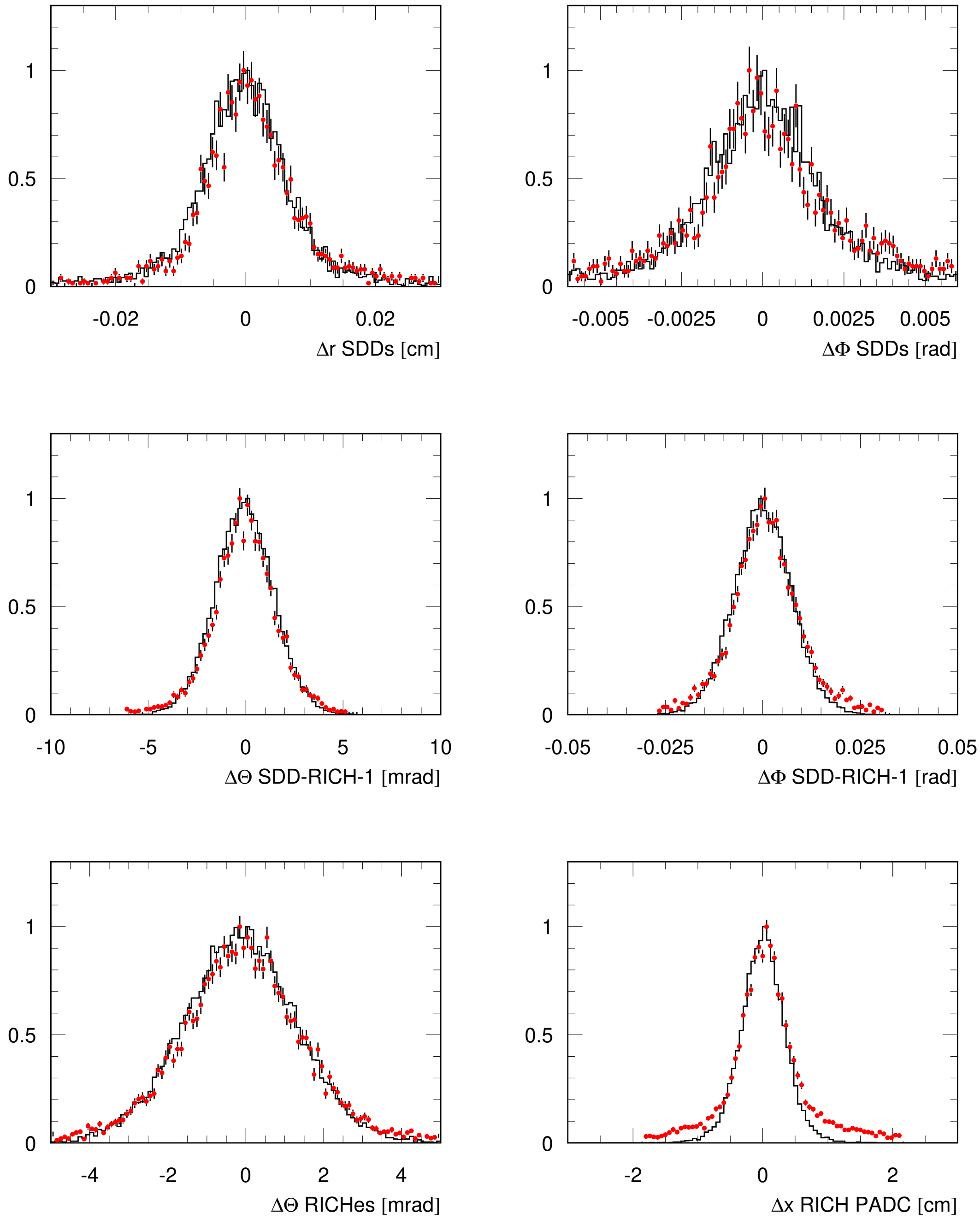

Figure 6.4: Matching distributions data and Monte-Carlo. The plots are scaled such that the maxima of the distributions, data and Monte-Carlo, are equal. The histogram line is the simulation result and the dots resemble the data.

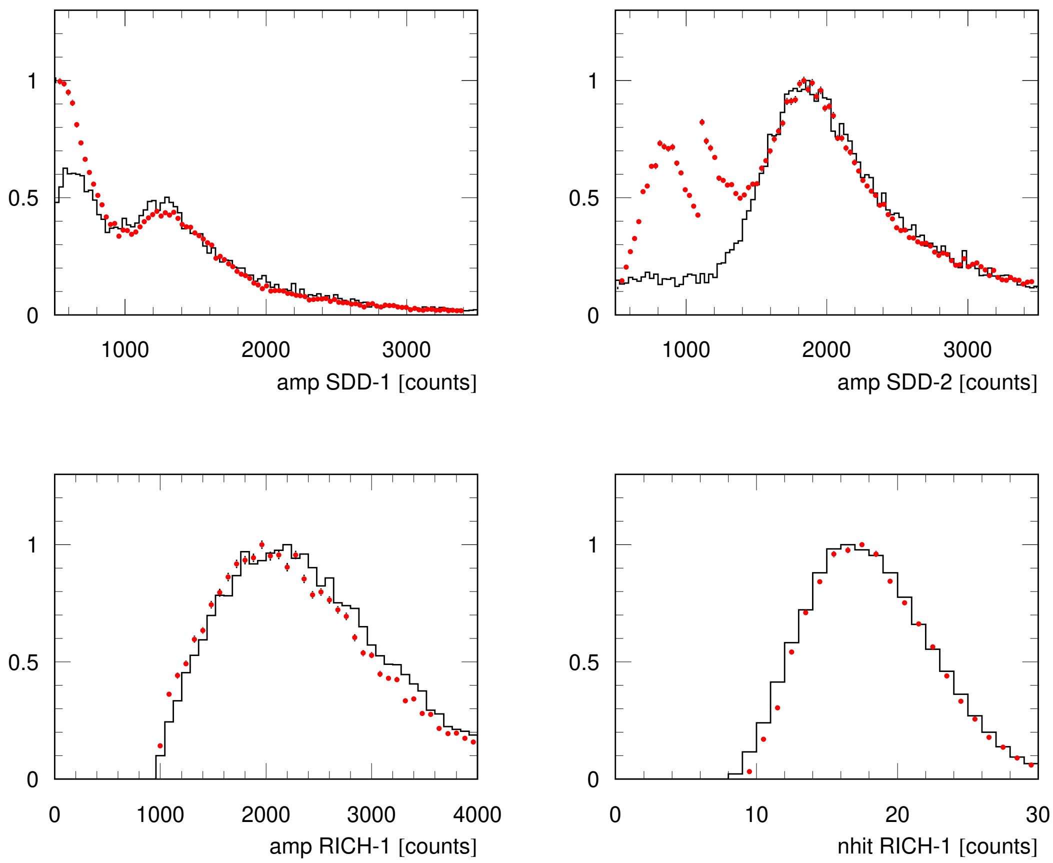

Figure 6.5: Amplitude distributions data and Monte-Carlo. The plots are scaled such that the local maxima for double hits/rings of the distributions, data and Monte-Carlo, are equal. Dots refer to data and the histogram line shows the Monte-Carlo distribution. The mismatch of the SDD amplitudes for single MIPs is due to the absence of such a component in the simulation. Above the chosen cut values (amp $>$ 1400 in SDD-2 and amp $>$ 1000 in RICH-1) the data is well described.

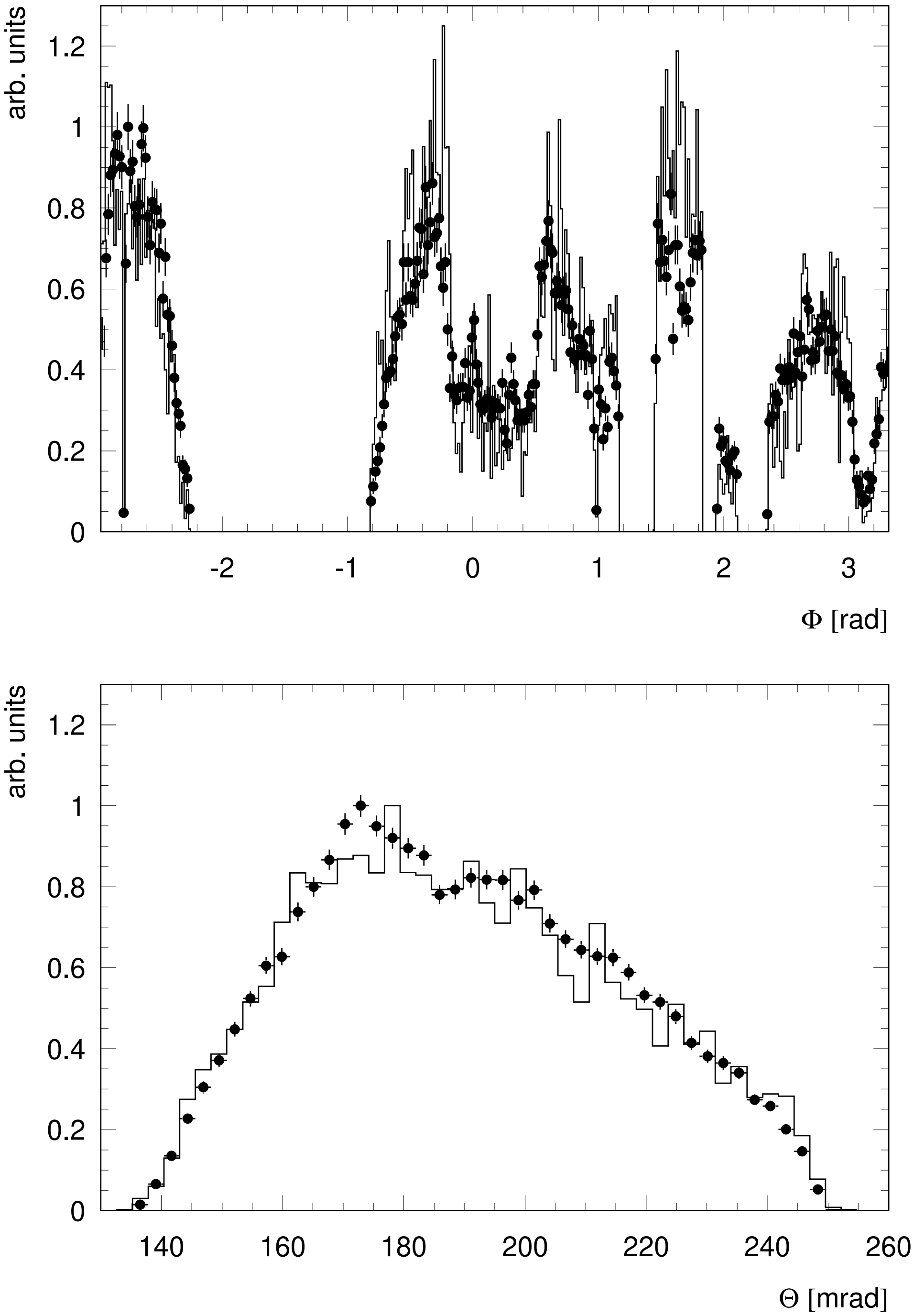

Figure 6.6: Angular distributions of data and Monte-Carlo.

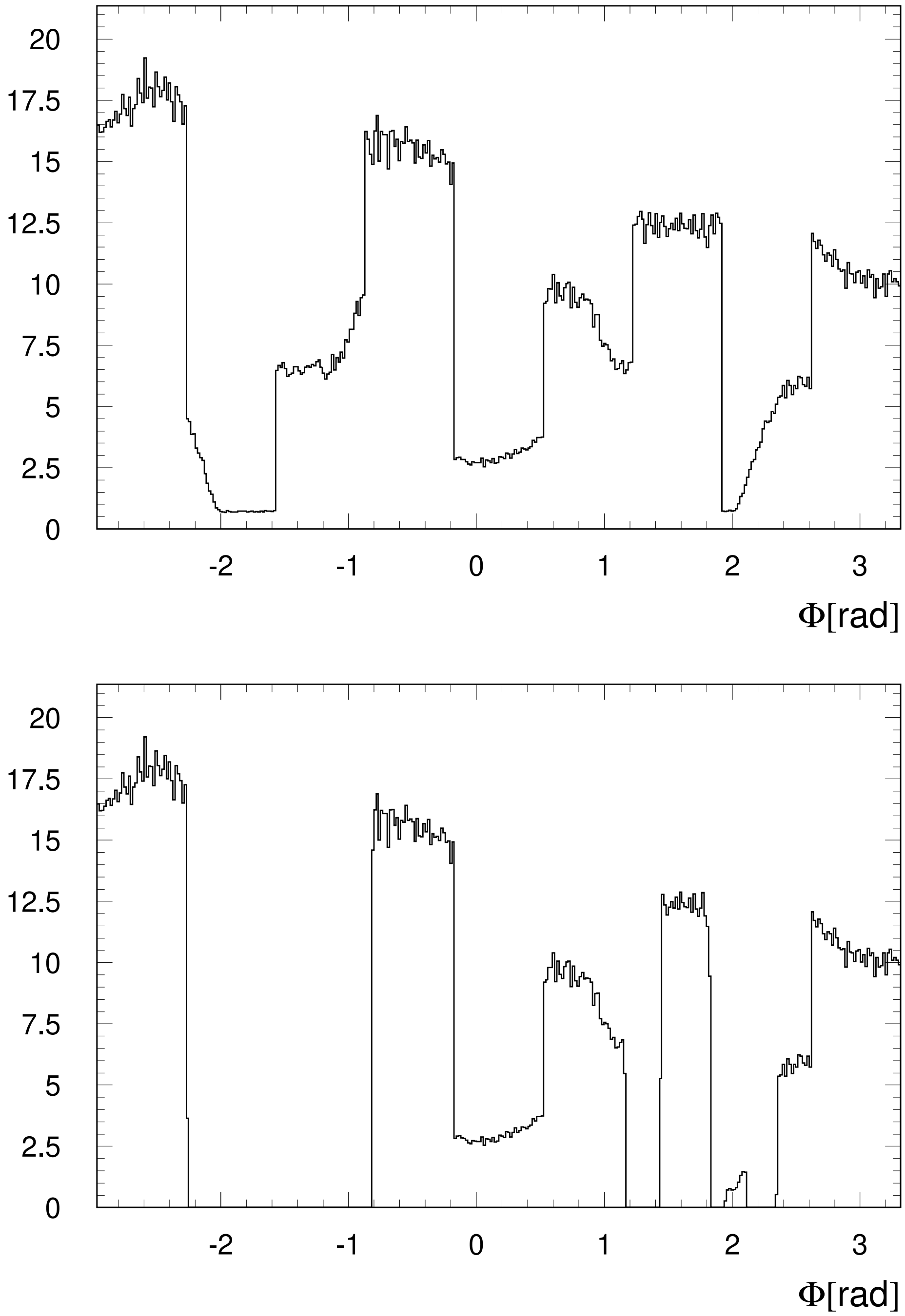

Figure 6.7: Angular distributions from the simulation of the conversion length. The upper picture shows the distribution as expected for a 100% operational spectrometer. The bottom picture shows the expected distribution when the known dead areas are cut out.

Chapter 7

The Chapter of Genesis

To make a statement on the observation of direct photons, the number of photons expected from the decay of hadrons must be known. In this analysis the same event generator GENESIS is used as for the low-mass electron-positron pairs. Descriptions can be found in [3,10,11,27]. The review of the principles shall therefore be brief.

7.1 Principle of Genesis

The GENESIS program could be described as a decay-machine. One particle after the other, randomly selected according to the probabilities given in the last column of table 7.1, are sent through a chain of decays until only stable particles remain. The decay dynamics are treated as described in [3]. The rapidity distributions are taken, as far as possible, from measurements in Heavy-Ion collisions. For the branching ratios of all considered decays the summary by the Particle Data Group is used [38]. The inclusive production ratios of hadrons are implemented relative to the number of π^0s. Inclusive hereby means that all decays of other particles which contribute to the total yield are already considered in this ratio. The values are taken from calculations in the framework of a thermal model [44,46] which is found to describe the hadronic final state well. Figure 7.1 shows a summary of measured relative particle abundances along with the calculations. The predicted values are confirmed for 18 different particle ratios. For the analysis only those photons are used, which are produced by a decay of a primary particle. In this way double counting is avoided.
The $p_\perp$ distributions of all hadrons apart from the π^0 are calculated under the

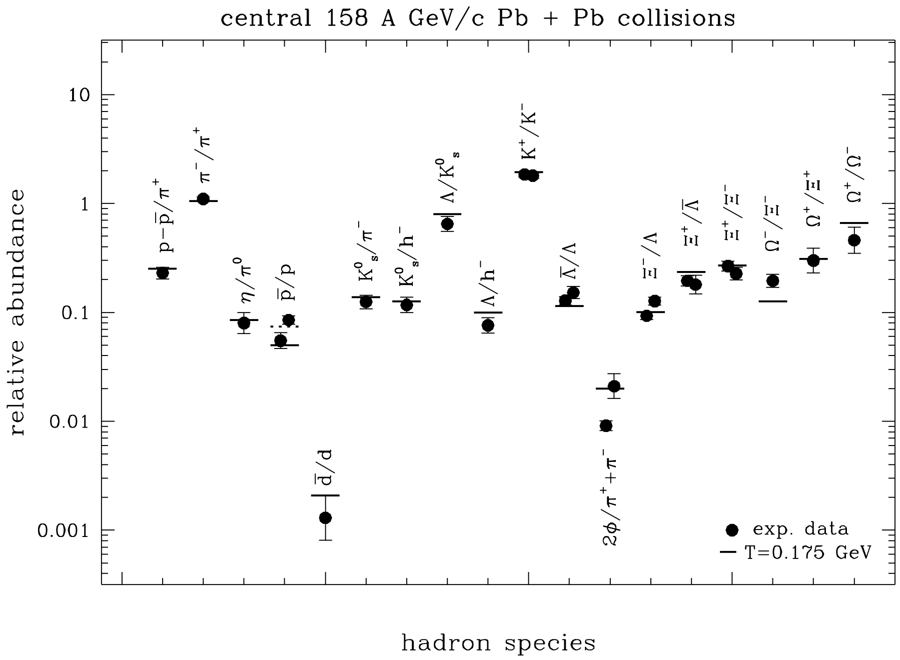

Figure 7.1: Relative abundances of hadrons, measured and compared to calculations in a thermal model. [45]

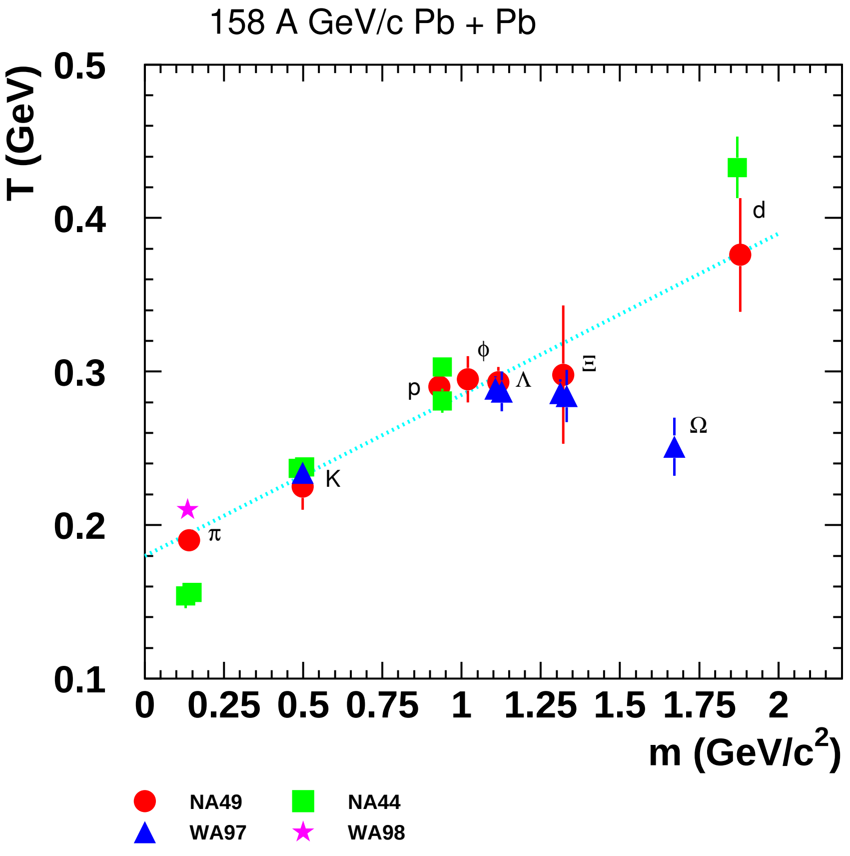

Figure 7.2: Dependence of the slope parameter on particle mass. The dotted line indicates the fit-result as reflected by equation 7.2. The data was summarized in [45]

Particle Decay	Branching Ratio	$\sigma_{tot}/\sigma_{\pi^0,tot}$	$\sigma_\gamma/\sigma_{\gamma,tot}$
$\pi^0 \to \gamma\gamma$	98.798 %	1	94.616 %
$\pi^0 \to \gamma e^+e^-$	1.198 %	1	1.147 %
$\eta \to \gamma\gamma$	39.25 %	8.5 %	3.20 %
$\eta \to \gamma e^+e^-$	0.49 %	8.5 %	$4.0 \cdot 10^-4$
$\eta \to \gamma\pi^+\pi^-$	4.78 %	8.5 %	0.39 %
$\eta' \to \gamma e^+e^-$	$5.6 \cdot 10^-4$	0.78 %	$4.1 \cdot 10^-6$
$\eta' \to \gamma\rho$	0.99 %	0.78 %	$7.4 \cdot 10^-5$
$\eta' \to \gamma\gamma$	2.12 %	0.78 %	$1.6 \cdot 10^-4$
$\rho \to \gamma\pi^+\pi^-$	$4.44 \cdot 10^-5$	9.4 %	$4.0 \cdot 10^-6$
$\omega \to \gamma\pi^0$	8.5 %	6.9 %	0.57 %
$\Phi \to \gamma\eta$	1.25 %	1.26 %	$1.5 \cdot 10^-4$

Table 7.1: Particle decays and relative cross-sections implemented in GENESIS. Since only photons from primary particles are used for the analysis, only decays which yield photons are considered here. The branching ratios are taken from [38]. The (inclusive) particle production ratio, relative to the number of π^0s is taken from [46]. The last column shows the composition of the obtained photon-sample, normalized to one. Note that, compared to the most prominent decays $\pi^0 \to \gamma\gamma$ and $\eta \to \gamma\gamma$, all the others contribute on the 1 %-level or below.

assumption that their spectral shape can be described as

$$\frac{1}{m_t}\frac{dN}{dm_t} = e^{-(m_t - m_0)/T} \quad , \tag{7.1}$$

with the *transverse mass* defined as $m_t = \sqrt{m^2 + p_\perp{}^2}$, m_0 being the particle rest-mass. The experimental finding that in p-p collisions, to first order, all hadron distributions can be parametrized according to equation 7.1 using one common slope parameter T is called *m_t-scaling*. In Pb-induced collisions at the CERN SPS a changing of the slope with mass is observed [45]. Figure 7.2 shows a summary of various measurements. A linear fit to all this data results in

$$T = 0.175 MeV/c^2 + 0.115 MeV/GeV * m_0 \ . \tag{7.2}$$

For the η-meson, the most important source of photons apart from π^0, this results in T = 238 MeV/c^2. Up to now, no reliable direct measurements exist to check this value, but the interpolation of many measured slope parameters as illustrated in figure 7.2 gives some confidence.
The absolute normalization of the generator result is done by quoting the number of produced photons relative to the number of neutral pions in one unit of rapidity. Using the same low-$p_\perp$-cutoff for the π^0s in the generator as in the data, the problem which arises through the uncertainty in extrapolating to $p_\perp = 0$ can be

to first order avoided. This fact is extremely valuable with respect to the final systematic error, as those uncertainties are indeed large. The following section gives a description of how the input spectra for neutral pions are achieved.

7.2 Input distributions for π^0

The differential ratios for hadron production are applied in GENESIS to the given $p_\perp$-spectra, which are normalized to an integral of one. To get the correct ratio of, say, η/π^0 at some value of $p_\perp$, it is therefore important to use an input spectrum for the π^0 which is extrapolated in the best possible way to $p_\perp = 0$. To study the systematic error introduced by the choice of some such spectrum, four different $p_\perp$-distributions are created, each in its own a plausible choice.

- Spectrum no. 1:
  The data for negatively charged hadrons (h^-) as measured by CERES [25,26] are used as a basis. Contributions of negative kaons as well as anti-protons [40] are subtracted to get a clean π^--spectrum. Since h^- have only been measured for $m_\perp$ - $m_0 > 200$ MeV/c^2, data of charged pions are used to get the correct spectral shape at very low transverse masses. The NA44 collaboration [41] has measured pions in the range 20 MeV/$c^2 < m_\perp$ - $m_0 < 750$ MeV/c^2, but without absolute normalization. This data is arbitrary scaled to match the so far corrected h^--spectrum in the region of overlap.
  The main difference between charged and neutral pions is the additional yield, which the latter get from the decay $\eta \rightarrow 3\pi^0$. To account for this, an additional component is added, with an inverse slope of 102 MeV/c^2 and integral fraction of 8 % to the total [46]. The resulting spectrum is later on referred to as "CERES h^- corrected". The upper plot in figure 7.3 shows the spectra of CERES h^-, kaons, and anti-protons, along with the $\eta \rightarrow 3\pi^0$-component to give a quantitative idea of the applied corrections, as a function of transverse momentum. At the highest $p_\perp$ the fraction is $(K^- + \bar{p})/h^- = 30$ %. The bottom half of figure 7.3 shows the final π^0-spectrum.

- Spectrum no. 2:
  The WA98 collaboration has measured neutral pions in a range 200 MeV/$c^2 < m_\perp$ - $m_0 < 3.5$ GeV/c^2 [49]. These are used as a basis which is then extrapolated to small $m_\perp$ using the NA44 data of charged pions and, in this region, corrected for the contribution of $\eta \rightarrow 3\pi^0$ in the same way as described above. The result is referred to as "WA98 π^0 corrected" in the following chapter. This version is also used as generator input in the open pair analysis [27].

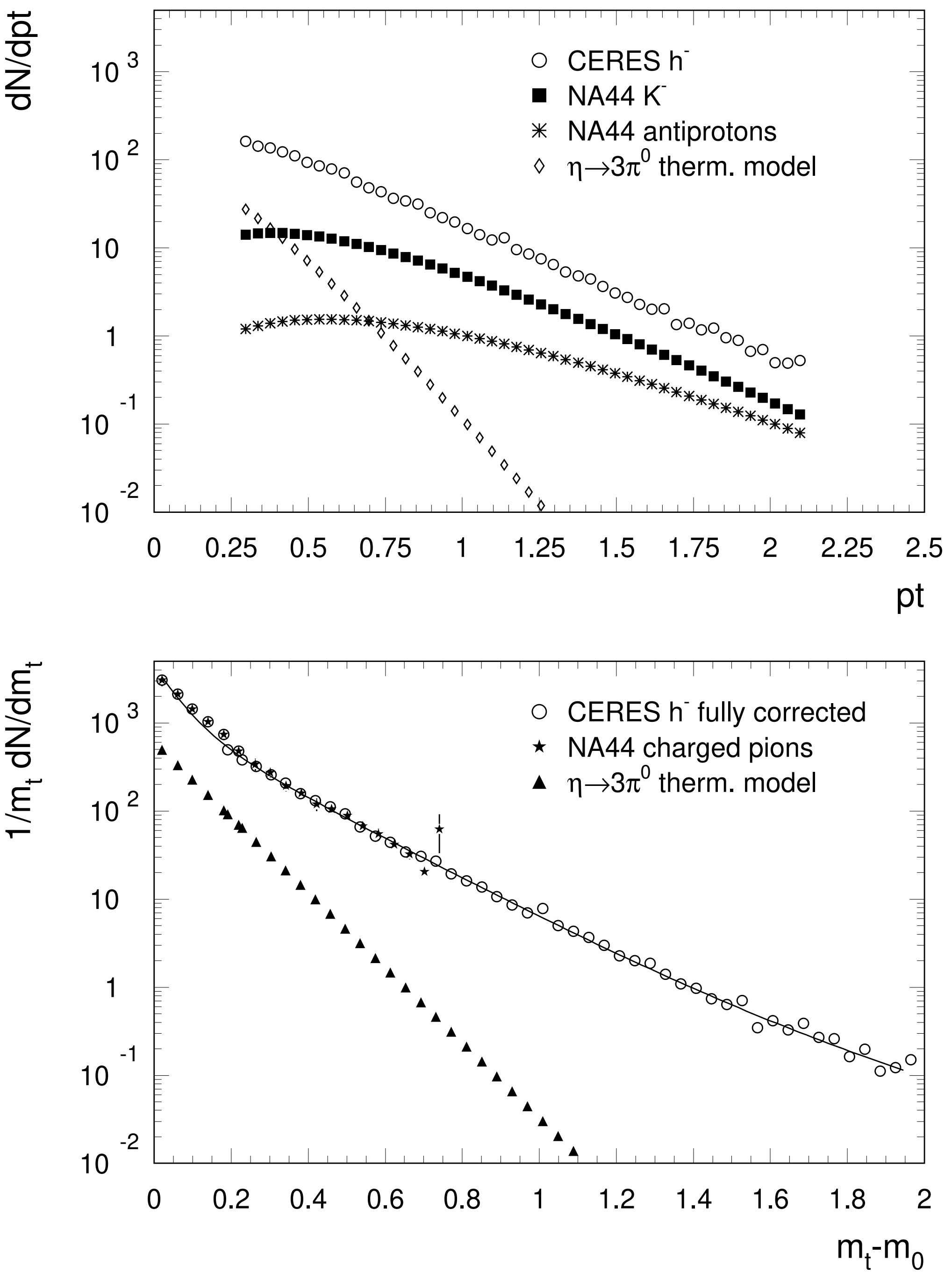

Figure 7.3: Input spectra for neutral pions for the example of "CERES h$^-$ corrected".

- Spectrum no. 3:
  In the bottom half of figure 7.3 one can see a sharp kink produced at 200 MeV/c^2 by adding the NA44 pions. This surprising shape suggests some problem in the measurement of NA44. To study the impact on the systematic error of the generated photons, the π^0-spectrum of WA98 is simply extrapolated to $m_\perp$ - m_0 = 0, and used as an alternative input spectrum. It is later referred to as "WA98 π^0". Whereas for spectrum no. 2 the minimum bias data of WA98 was used (70 % of the total geometric cross-section), here the WA98 data for central collisions (10 % σ_{geo}) serves as input. The difference of these spectra at large $m_\perp$ serves as an additional variation to test the centrality dependence.

- Spectrum no. 4:
  For the same reason as described in the last point, the "CERES h^- corrected" spectrum is modified by not using the NA44 data, but rather extrapolate the h^- to $m_\perp$ - m_0 = 0. It is then corrected for K^-,$\bar{p}$, and $\eta \to 3\pi^0$ as described above. This is later-on called "CERES h^- corrected NO NA44"

7.3 How to get from h^- to π^0

The number of h^- measured by CERES is used for absolute normalization of the photon spectra. Interpreting the integral number of h^- above sum lower $p_\perp$ cutoff as the number of π^0s, introduces an error, since also here all the corrections mentioned in the previous section have to be applied. Using the correction method as explained for the creation of the "CERES h^- corrected"-spectrum, a correction factor is deduced, which can be written as follows. With

$$N\pi^0 = \int_{0.4}^{2.5} \frac{dN\pi^0}{dp_\perp} dp_\perp = \int_{0.4}^{2.5} \frac{dNh^- - dNK^- - dN\bar{p} + dN(\eta \to 3\pi)}{dp_\perp} dp_\perp \quad (7.3)$$

we define

$$C_{h^-}^{\pi^0} = \frac{N\pi^0}{Nh^-} \quad . \quad (7.4)$$

With the procedure for spectrum no. 1 one obtains $C_{h^-}^{\pi^0} = 0.84$. If the NA44 data are not used, as for spectrum no. 4, one obtains $C_{h^-}^{\pi^0} = 0.87$. This discrepancy will be later on used as part of the systematic error on the normalized number of photons.

A further correction could be necessary due to the isospin asymmetry. Taking the relative abundances of the constituent quarks from table 7.2 under the assumption that $N\pi^0 = (N\pi^+ + N\pi^-)/2$ one would get a maximum correction of $N\pi^0 = 0.94 \cdot N\pi^-$. Since one has observed baryon stopping in Pb-Au collisions at SPS energies ([26] for an overview) this effect will play a role also at mid-rapidities.

nucleus	N(udd)	p(uud)	u-quarks	d-quarks
Pb^{82}_{208}	126	82	290	334
Au^{79}_{197}	118	79	276	315

Table 7.2: Parton abundances in a Pb-Au collision

The number quoted here is an upper limit. On the other hand, measurements available for $p_\perp > 1$ GeV/c show no visible deviation from $N\pi^+/N\pi^- = 1$. For this analysis it was chosen not to do this correction, but to consider it as an uncertainty which enters as an (asymmetrical) systematic error.

7.4 On the η/π^0 - Problem

The four different input spectra differ mainly in the region of very small $p_\perp$. The main impact on the photon cross-section predicted by the generator is kept at a minimum by using only the number of π^0s above some $p_\perp$ cutoff (0.4 GeV/c^2 in this analysis) for absolute normalization. As explained later-on in the discussion of systematic errors (chapter 8.4), the uncertainty in the pion spectra at low transverse momentum introduces an error only via the relative abundance of η-mesons in the total spectrum. This means that to judge the effect of different input spectra, also the relative cross-section η/π^0 must be known. Figure 7.4 shows this as a function of $p_\perp$ for the created input spectra, together with several experimental results. The relatively small ratio of 8.5 % used in the generator is somewhat misleading, considering that in the analysis photons are measured only with $p_\perp > 0.4$ GeV/c. Above this cutoff, the integral ratio is about 20 % (see plot). The preliminary result (without systematic errors) of a measurement by the WA98 collaboration [49] is $\eta/\pi^0 = (53\pm10_{stat})$ % for $m_\perp > 1$ GeV/c^2, scaled to the CERES centrality selection of 35 % of the total geometrical cross-section. Within large errors, their result stays constant over a range of 1 GeV/c^2 $< m_\perp <$ 3 GeV/c^2. For the ratio integrated over all $p_\perp$ the scaling to CERES centrality yields $\eta/\pi^0 = (12\pm2_{stat})$ %. In figure 7.4 one can see the problems for the extrapolation to $p_\perp = 0$. Although the result of WA98 indicates a larger relative abundance of η-mesons in Pb-Pb collisions than for the lighter collision systems, no reliable judgment for the integrated ratio can be made. The measurement of CERES/TAPS has the best precision, since it extends to very low transverse momenta. On the other hand, this may not be correct for Pb-Pb data.
A variation of this ratio will be part of the determination of the systematic error in chapter 8.4.

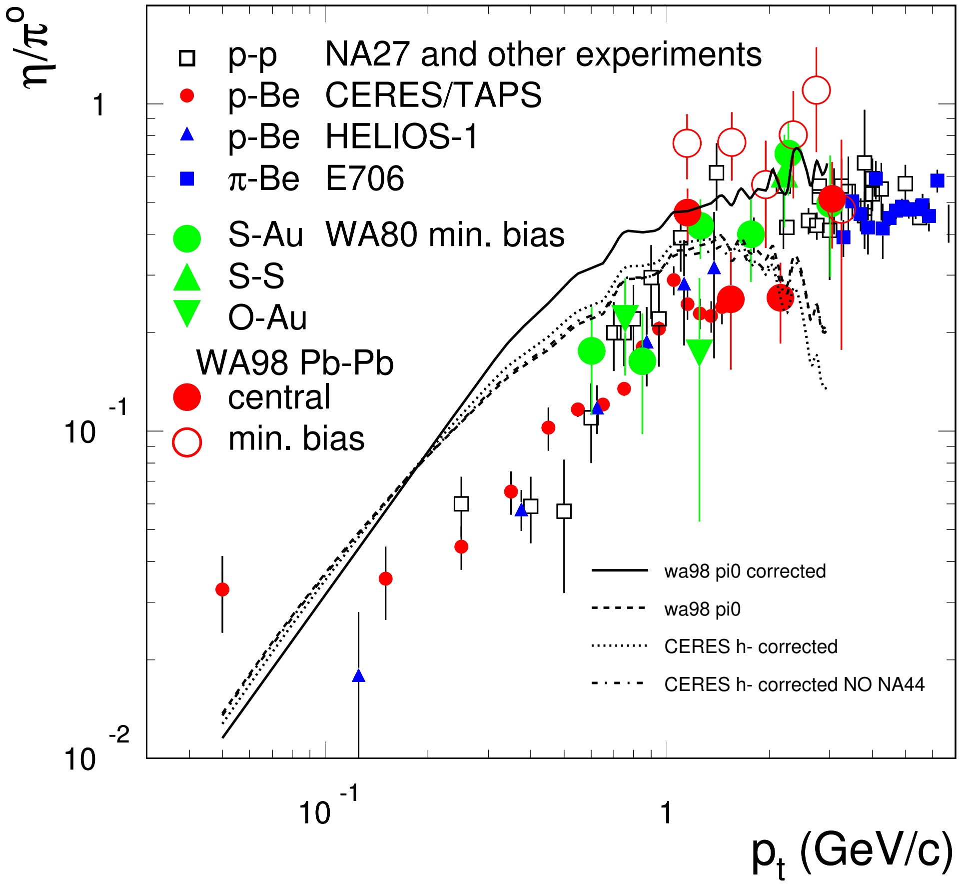

Figure 7.4: Differential ratio η/π^0 for the four different generators. The spectrum "WA98 π^0 corrected" was produced with min.bias data (see text) and the spectrum "WA98 π^0 with data from more central collisions. Whereas for small $p_\perp$ no difference can be observed, for $p_\perp > 1$ GeV/c the discrepancy is obvious. Also plotted are various experimental results for proton, S, and Pb-induced collisions.

Chapter 8

Photons per π^0

The analysis procedure described in chapter 5 resulted in a sample of 34000 reconstructed conversion pairs. First of all, the number of all photons produced in the observed collisions must be extracted from the data. Detector effects like acceptance, efficiency and relevant conversion probability are corrected for, using a Monte-Carlo simulation of the spectrometer.
To make a statement on direct photons the obtained signal must be compared to a prediction on the number of photons from hadron decays. Since the GENESIS program (see chapter 7) simulates only particle decays and not complete heavy ion collisions, a comparison cannot be made for such a simple quantity as the number of photons per event. Relative abundances of primary particles and the decay branching ratios are implemented using the current knowledge about Pb-Au collisions at such energies. The number of primary π^0 is chosen here for absolute normalization, because it is accessible both in the generator and in the data. How the corrected and normalized numbers are produced is subject of the following paragraphs.

8.1 Correction of $p_\perp$-spectra

The most obvious loss of efficiency is due to the big holes in the acceptance. Some 25 % of the spectrometer is covered by the dead high-voltage sector of the pad-chamber. Three other segments in Φ had to be omitted for the analysis beacuse of dead anodes in the silicon drift detectors (see figure 6.1). These parts are explicitly switched off in the data analysis as well as in the Monte-Carlo, since their contribution can be simply calculated with high precision. After this step only 66.91 % of the spectrometer are active. The efficiency loss from border effects at the edges of these sectors are left to be described by the simulation.
Apart from the efficiency as a function of $p_\perp$, also the distortion of the spectra

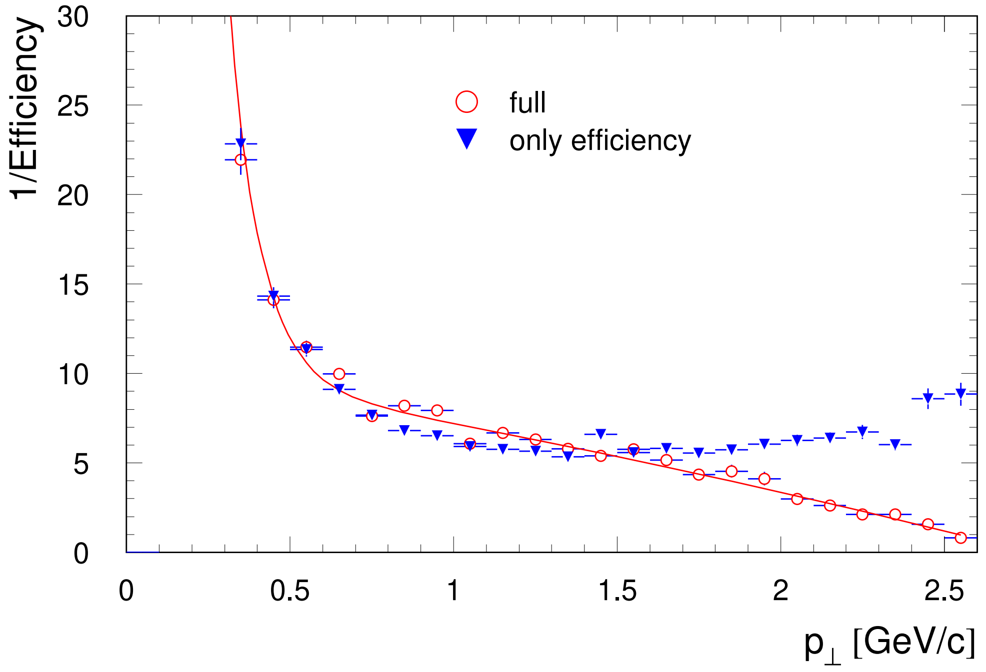

Figure 8.1: Correction function from Monte-Carlo. The open circles represent the full correction factor taking into account also the finite momentum resolution. The triangles show the pure inverse efficiency obtained by using the simulated momentum both for input and output spectrum.

due to finite momentum resolution must be corrected. On an essentially constant distribution the momentum smearing has no impact, if the reconstructed momentum is with equal probability larger or smaller than the original momentum. For an exponentially decreasing spectrum the situation is different. The additional population of regions with larger momenta cannot be compensated. The result is an overestimated yield at high momenta.

For each simulated photon conversion the generated momentum is known. In case of a successful reconstruction by the analysis program also the reconstructed momentum is memorized. Dividing the simulated by the reconstructed $p_\perp$-spectrum using the simulated and the reconstructed $p_\perp$ respectively, yields the correction function, i.e. the inverse efficiency including the correction for momentum resolution. This function is parametrized with

$$C(p_\perp) = p_1 e^{(-p_2 p_\perp)} + p_3 + p_4 p_\perp + p_5 p_\perp^2 \tag{8.1}$$

and multiplied with the data histogram to get the corrected spectrum.
The method works only, if the input spectrum for the Monte-Carlo resembles the corrected data. To ensure this an iterative procedure is used. The corrected spectrum is parametrized with three exponentials and used as a new Monte-Carlo input distribution. The simulation is then rerun and a new correction function determined. Already after two iterations the simulation output was indistinguishable from the data, when the spectrum produced by the GENESIS program was used as a first guess. The convergence of this method was found to be not affected by using different starting spectra. The resulting correction function stays stable, only the number of necessary iterations varies.
Figure 8.1 shows the final correction function. Apart from the full correction also the pure inverse efficiency is shown, omitting the effect of momentum smearing. This curve is essentially flat in the range 0.7 GeV/c $< p_\perp <$ 2.2 GeV/c. For $p_\perp <$ 0.4 GeV/c the correction due to efficiency is more than a factor 10. For $p_\perp >$ 2.5 GeV/c the discrepancy between pure efficiency and full correction is also a factor of 10. Further analysis is done only within this range.

8.2 Absolute Normalization

For comparison with the generated spectrum of photons from hadron decays, some common quantity for normalization must be found. In a previous analysis the charged particle multiplicity was used [11]. From this the number of neutral pions can be derived which is also used to normalize the generator spectrum. The two distributions can then be compared. The problem of this method is not only the systematic error which is introduced by the estimation of the number of π^0/Nch, but also that the (probably larger) error of the measurement of Nch itself is difficult to estimate (see chapter 6.5). An additional error is introduced when extrapolating the $p_\perp$ spectrum to zero. This is necessary to calculate the fraction of photons expected above a chosen lower $p_\perp$ cutoff.
The whole problem can be avoided by directly normalizing to the number of π^0s above a minimum $p_\perp$ as measured in the data. Since CERES cannot directly reconstruct neutral pions, a measurement of negatively charged hadrons (h^-) is used instead [25, 26]. Data of charged hadrons is available from an analysis of the 1995 Pb-Au run. They are absolutely normalized to the number of events, in seven different regions of Nch. The 1995 setup of the spectrometer is almost exactly the same as for 1996, a fact which gives additional confidence in the precision of the absolute normalization.
Figure 8.2 shows the fully corrected multiplicity distributions for the 1995 h^-

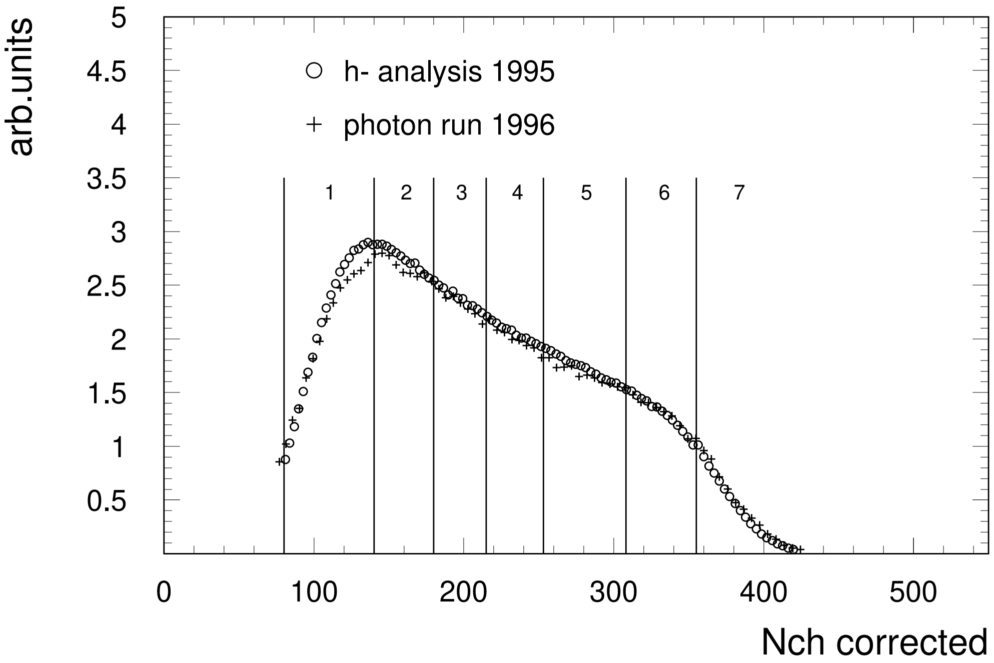

Figure 8.2: Multiplicity spectra for the h- analysis of the 1995 data and for the 1996 photon run. The spectra are scaled arbitrary in the vertical direction and a constant shift of -20 is applied to the 1996 data to get an exact agreement. For the photon spectra, only Nch-bins 2-7 are used to avoid uncertainties due to different trigger thresholds.

analysis and for the 1996 photon data. A constant shift of -20 was applied to the 1996 measurement to match the two spectra at large Nch. The shape of the spectra at high Nch has a physics origin and reflects the fact that here the most central collisions occur. A different shape at the lower end of the distribution stems merely from a slightly different setting of the Nch trigger. Once the two spectra are shifted in the described way and the lowest multiplicity bin is cut off, one can be sure to measure photons per event as well as h^- per event with the same centrality selection.
The integral number of h^- for $p_\perp > 0.4$ GeV/c is then corrected by a factor of 0.84 to get the number of π^0s. This factor is obtained as a by-product when creating the input spectrum for the hadron-decay generator (see chapter 7.3). The integral for $p_\perp > 0.4$ GeV/c of the uncorrected h^- spectrum is related to the corresponding integral of the corrected spectrum.

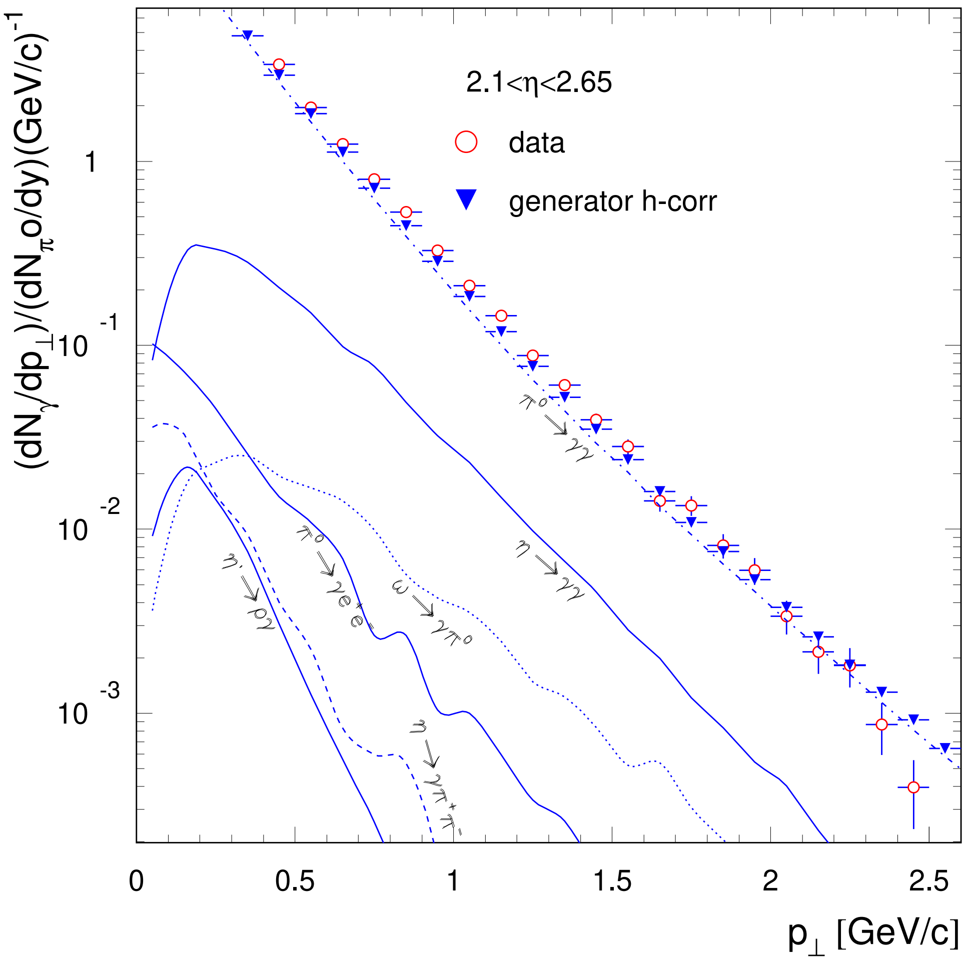

Figure 8.3: Photon $p_\perp$ spectrum absolutely normalized to the number of π^0 with $p_\perp(\pi^0) > 400MeV$. The circles represent the measured data, the triangles generated hadron decays. Also shown are the largest contributions of particle decays to the total generator spectrum.

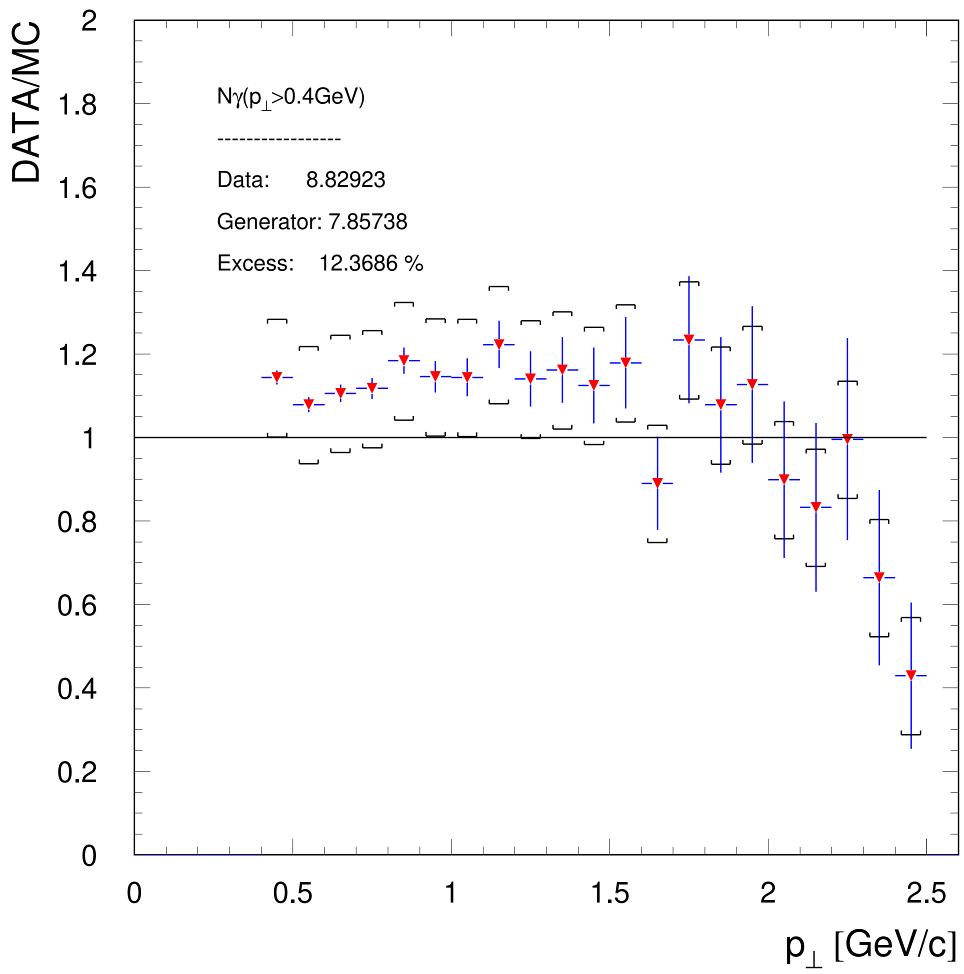

Figure 8.4: Ratio of measured photons versus photons expected from hadron decays. Here the "CERES h$^-$ corrected"-spectrum is used as input for the GENESIS program (see chapter 7.2).

8.3 Photon p$_\perp$-spectra

Once all corrections are known, the number of photons per π^0 can be calculated as

$$\frac{N_\gamma(p_\perp)}{N_{\pi^0}} = \frac{1}{\epsilon(p_\perp)} \cdot \frac{N_\gamma(p_\perp)}{evt} \cdot \left(0.84 \cdot \frac{N_{h^-}}{evt}\right)^{-1} \cdot \left(\frac{7}{9} \cdot \frac{X}{X_0}\right)^{-1} \tag{8.2}$$

where $1/\epsilon$ is the inverse efficiency, X/X_0 is the integral relative conversion length, and N_{h^-} is the number of negatively charged hadrons in one unit of rapidity.
Figure 8.3 shows the spectrum of reconstructed photons and generated hadron decays. For $p_\perp < 0.4$ GeV/c the efficiency drops rapidly below 5 % and its determination becomes inaccurate. For $p_\perp > 2.5$ GeV/c the statistical error is very

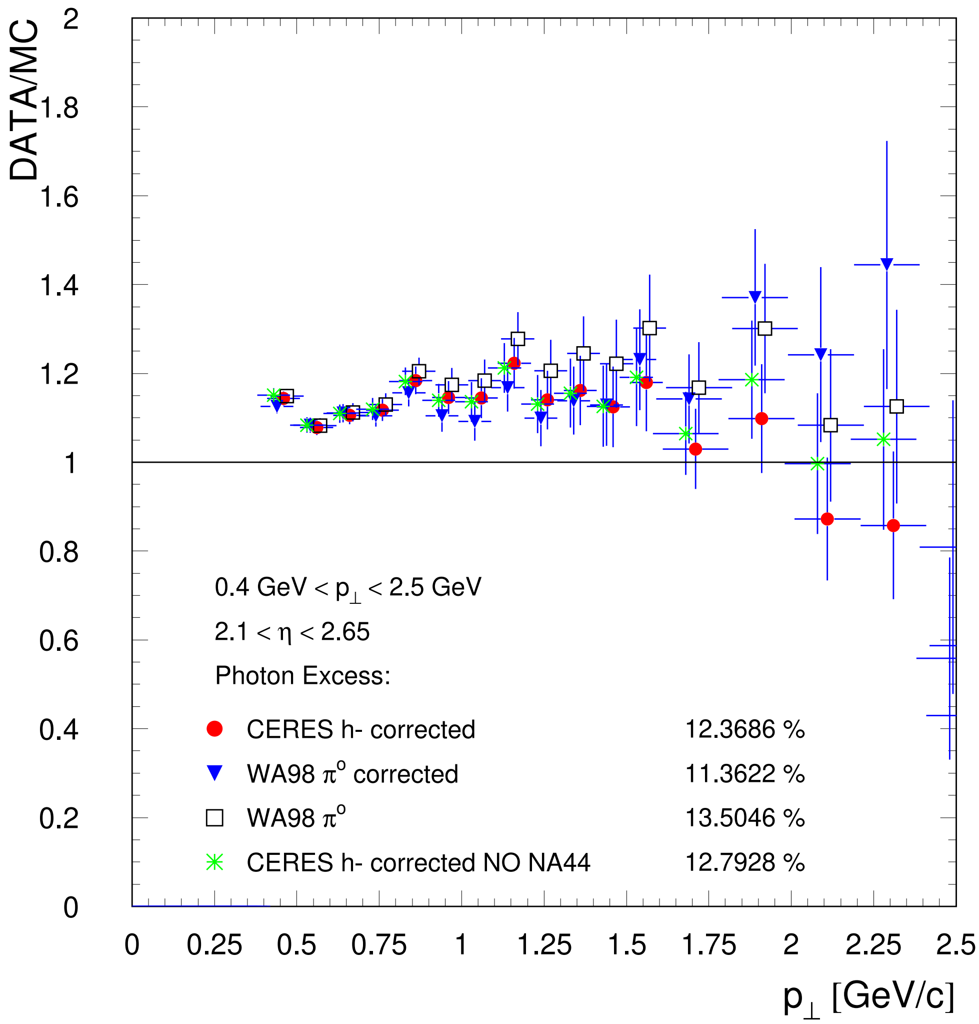

Figure 8.5: Ratio of measured photons versus photons expected from hadron decays shown for the four different input spectra used for the generator program.

large. The spectra are only plotted within this range. Also shown are those contributions to the total generator spectrum which are more than 1 %, at least in some region of $p_\perp$. The main decay channels are $\pi^0 \rightarrow \gamma\gamma$ and $\eta \rightarrow \gamma\gamma$.
Within $\pm$ 20 % the generated distribution follows the data points over four orders of magnitude in photon yield. Apart from a systematic tendency of the generated spectrum to overshoot the data for transverse momenta of more than 2 GeV/c, in general the data points are above the expectation from hadron decays.
To take a closer look, a linear representation is more appropriate. Figure 8.4 shows the ratio of signal from data over signal from generated photons. Included here are also the systematic errors as discussed in chapter 8.4. An error of 3.1 % on the number of photons from different input distributions for the generator is included, assumed to be constant in $p_\perp$. The differential effect of this uncertainty is shown

in figure 8.5. From this plot one learns that the undershooting of the generator prediction for large transverse momenta is seen only for input distributions which have the negatively charged hadrons measured by CERES as a basis. One can conclude that this effect is probably not due to a wrong correction of the photon data, but to different exponential slopes of the generator input distributions at high $p_\perp$.
Common to all of these spectra is a rise in the ratio which sets in at 0.5 GeV/c and ends in a plateau at 0.8 GeV/c. From there on up to 1.5 GeV/c the excess over the predicted hadronic yield is around 15 %. This is a somewhat more than 1 σ effect, taking into account statistical and systematic errors.

In the sum over the whole $p_\perp$-range one is, of course, dominated by the contribution at the lower end of the spectrum. In this analysis the integral number of photons per neutral pion is defined as

$$\frac{N_\gamma}{N_{\pi^0}} = \frac{\int_{0.4}^{2.5}(dN_\gamma/dp_\perp)dp_\perp}{\int_{0.4}^{2.5}(dN_{\pi^0}/dp_\perp)dp_\perp} \quad . \tag{8.3}$$

For reconstructed photon conversions one finds:

$$r_{incl} = \frac{N_\gamma}{N_{\pi^0}} = 0.883 \pm 0.007_{stat} \begin{array}{c} + \\ - \end{array} \begin{array}{c} 0.090_{syst} \\ 0.092_{syst} \end{array} \tag{8.4}$$

and for photons from the generator:

$$r_{hadr} = \frac{N_\gamma}{N_{\pi^0}} = 0.786 \pm 0.001_{stat} \pm 0.031_{syst} \tag{8.5}$$

This means an excess of

$$\frac{r_{incl} - r_{hadr}}{r_{hadr}} = 12.4\% \pm 0.83\%_{stat} \begin{array}{c} + \\ - \end{array} \begin{array}{c} 13.0\%_{syst} \\ 13.4\%_{syst} \end{array} \tag{8.6}$$

over the expected yield from hadron decays. For the excess as described in equation 8.6 this results in an upper limit of

$$\frac{r_{incl} - r_{hadr}}{r_{hadr}} < 33.8\% \tag{8.7}$$

on the 90 % confidence-level. The systematic errors are discussed in the following section.

8.4 Systematic Errors

8.4.1 Simulation of the Spectrometer

Part of the systematic error of the final result stems from uncertainties in the determination of the efficiency of the photon reconstruction. The Monte-Carlo simulation is tuned to represent the data as good as possible. However, in some cases the degree of resemblance can only be judged with finite precision. The most important points where such uncertainties arise shall be pointed out below.

- The most important of all matching cuts is the one on radial match between RICH-2 and pad-chamber (figure 6.4). It gives the best background reduction and is set to $2 \cdot \sigma$ in the analysis. Different attempts to fit the Δx and Δy distributions show that the accuracy with which the Monte-Carlo describes the width can be judged only within $\pm$ 3 %. The impact on the determination of efficiency can be studied varying the cut by this value.

- Part of the identification of double rings in the first RICH is a cut on the amplitude sum of all hits used in the ring fit. Figure 6.5 shows a good agreement of data and Monte-Carlo. However, this can only be said within $\pm$ 40 ADC-counts. The cut requires a minimum of 1000 ADC counts.

- The most powerful cut to identify a conversion is to require a minimum dE/dx in SDD-2. In this analysis it is set to 1400 ADC counts. Comparison of the distributions of data and Monte-Carlo (figure 6.5) can be made with a precision of $\pm$ 30 counts. Again the inaccuracy of the efficiency determination is tested by varying the minimum dE/dx within this uncertainty.

- Extensive studies done by varying many of the fundamental parameters of the Monte-Carlo simulation [27] have shown that one can assume a $\pm$ 1.5 % accuracy on all single detector efficiencies. For this analysis, SDD-1 enters only via the background rejection and plays no role for the error on the photon reconstruction efficiency. In SDD-2 only one hit and in RICH-1 only one ring contribute to the conversion. After the magnetic field, in RICH-2 and the pad-chamber, two rings or hits are measured for each photon. Therefore the resulting error on the photon reconstruction efficiency can be written as

$$\epsilon_{photon} = \sqrt{\Delta(\epsilon_{SDD-2})^2 + \Delta(\epsilon_{RICH-1})^2 + \Delta(\epsilon^2_{RICH-2})^2 + \Delta(\epsilon^2_{PADC})^2} = \pm 4.7\% \quad . \tag{8.8}$$

- Due to limited CPU-time the correction function shows some remaining statistical fluctuations. These are eliminated by applying a fit to the histogram which is then used to analytically correct the data. The scattering of the points around this fit give a contribution which is found to be quadratically small as compared to the error on the absolute efficiency. It is assumed to be negligible.

The impact of the first three points is tested by varying the three cut values one after the other. The Monte-Carlo information is then reprocessed with these new settings and the resulting correction functions compared. The three contributions are added quadratically. On the integrated signal for $p_\perp > 0.4$ GeV/c the resulting relative error is $\pm$ 5.4 %.

8.4.2 Determination of the Conversion Length

The conversion length and the thickness of all materials which contribute to the overall conversion probability are known only with finite precision. Using the fast simulation method as described in chapter 6.4 the impact on the determination of X/X_0 can be studied.

- The complicated shape of the Cu-conductor strips on the HV-bridges of the drift detectors is not implemented in every detail (see photograph 6.2). An approximation is made by parameterizing triangular shapes of different conversion length according to the measured Cu-density. The error on this method is estimated to be $\pm$ 50 % which gives a relative error of $\pm$ 0.7 % on X/X_0 and the same on the normalized number of photons.

- One of the two largest contributions is the error for the HV-bridges themselves. The exact composition of the circuit board material, i.e. the relative density of glass-fiber and epoxy, is unknown. The error is estimated to be $\pm$ 10 % which results in a relative uncertainty of $\pm$ 1.4 % on the measured signal.

- The PVC foil which was used as a support structure for the segments of the steel converter has a glue coating and its overall thickness can also be measured only with finite precision. The error is (somewhat generously) estimated to be $\pm$ 10 % and the effect on the signal is $\pm$ 1 %.

- The thickness of the steel converter (100 μm) is known with the machining precision of about 1 μm. The amount of material lost by cutting out the triangular segments (using a laser) is estimated to be negligible. Some uncertainty is, however, in the exact composition of the chosen steel. This uncertainty is quantified by comparing the precisely measured weight of the whole disc with the calculated weight. For the calculation the thickness and the measured diameter along with the density of Fe is used. The error is found to be $\pm$ 3 % which has an effect (the largest of all contributions) of $\pm$ 1.8 % on the error of the measured number of photons.

The quadratic sum of all these errors is $\Delta(X/X_0) = \pm$ 2.6 %.

8.4.3 Absolute Normalization to Nπ^0

The multiplicity distribution was shifted by -20 to fit the 1995 data. Since this shift is the same for Nch in an event where a photon was found as for the determination of the total number of input events in the chosen Nch-range, an uncertainty in this shift should cancel to first order. A variation of this shift by $\pm$ 10 indeed showed no significant effect on the normalization.
The systematic uncertainty in the total number of negatively charged hadrons is $\pm$ 3 % [43]. This directly propagates into the error on the number of photons.
A somewhat larger error stems from the correction factor $C_{h^-}^{\pi^0}$ (equations 7.3 and 7.4) which is used to translate the number of h$^-$ into a the corresponding number of π^0. Various tests have been made to quantify this:

- The particle ratio η/π^0 integrated over all $p_\perp$ is not very well known. Calculation in a thermal model [46] indicates a number of 8.5 %. Measurements of the WA98 collaboration in Pb-Pb collisions [49] favour 12 %, if one extrapolates their numbers to the CERES centrality selection. From p-Be collisions CERES extrapolates 5.3% [47]. To estimate the contribution to the systematic error, a value of (8 $\pm$ 3.2) % is used, assuming that the measurement for p-Be can be regarded as a minimum and taking the difference between this and the value from the thermal model as an estimate for a symmetric error. This has an influence via the added signal from the decay $\eta \rightarrow 3\pi^0$ and the effect on the correction factor is $\pm$ 2.8 %.

- The charged pion spectrum of the NA44 collaboration, which is used to extrapolate the corrected CERES h$^-$ data to low $p_\perp$, shows an extremely large exponential slope. Figure 7.3 shows a kink in the spectrum at $m_\perp$-m_0 = 0.2 GeV/c which is commonly regarded with suspicion. As an alternative correction method only the CERES data is extrapolated to zero, which gives an asymmetric error on the correction factor of (+ 3.4 - 0) %.

- The absolute number of K$^-$ and $\bar{p}$ is given by NA44 with an error of 20 %. Variation within these boundaries give an error on the correction factor of $\pm$ 4 % for the Kaons and $\pm$ 1.2 % for the anti-protons.

- The problem of isospin asymmetry has been discussed in chapter 7.3. Since it is, from experimental evidence, unclear how large such a correction would have to be in this analysis, it is not done at all. As an upper limit, a correction Nπ^0 = 0.94$\cdot$Nπ^- has been estimated. Since a large fraction of nucleons is found *not* at mid-rapidities only half of this maximum value is assumed as a possible correction. It introduces an error on the correction factor of (+ 0 - 3) %.

source of error	test method	relative error on N_γ/N_{π^0}
RICH-PADC match	vary cut by $\pm$ 3 %	$\pm$ 3 %
sum-amp in RICH-1	vary cut by $\pm$ 40 counts	$\pm$ 2 %
amp in SDD-2	vary cut by $\pm$ 30 counts	$\pm$ 2 %
rec. efficiency	vary many fundam. MC-param.	$\pm$ 4.7 %
X/X_0 Cu-conductors	vary thickn. by $\pm$ 50 %	$\pm$ 0.7 %
X/X_0 HV-bridges	vary thickn. by $\pm$ 10 %	$\pm$ 1.4 %
X/X_0 PVC-foil	vary thickn. by $\pm$ 10 %	$\pm$ 1 %
X/X_0 steel-converter	vary thickn. by $\pm$ 3 %	$\pm$ 1.8 %
norm. of h^-	result of h^--analysis	$\pm$ 3 %
corr. factor for norm.	vary η/π^0 by $\pm$ 50 %	$\pm$ 3.4 %
corr. factor for norm.	do not use NA44 data	(+ 0 - 4) %
corr. factor for norm.	vary K^- dN/dy by $\pm$ 20 %	$\pm$ 4.8 %
corr. factor for norm.	vary $\bar{p}$ dN/dy by $\pm$ 20 %	$\pm$ 1.5 %
corr. factor for norm.	isosp.asym (+ 0 - 3) %	(+ 3.6 - 0) %
sum data		(+ 10.2 - 10.5) %
η/π^0 in generator	vary η/π^0 by $\pm$ 50 %	$\pm$ 2.4 %
inp.spec. for generator	use 4 diff. spectra	$\pm$ 3.1 %
sum generator		$\pm$ 4 %

Table 8.1: Summary of systematic errors. The errors which are assumed to be constant in $p_\perp$ are summed quadratically. In the case of asymmetric errors the negative and positive part are summed separately. Note that the errors introduced by the uncertainty in the ratio η/π^0 are anticorrelated in data and generator. for the error on the ratio data/generator they are summed linearly.

8.4.4 Uncertainties in the Generator

- The uncertainty in the ratio η/π^0 as discussed in the previous section also leads to an error in the prediction by the generator. Its effect is studied in the same way as for the error of the absolute normalization of the data. Since the effect on the spectral shape, although present, is small compared to the statistical errors, only an error on the integral is assumed. It is found to be $\pm$ 2.4 %. Note that this error is 100 % anti-correlated to the error on $C_{h^-}^{\pi^0}$ discussed as first point of the previous section. For the total uncertainty on the ratio in figure 8.4 they are added linearly.

- Several plausible input distributions have been tested for the $p_\perp$-spectrum of π^0s. They strongly effect the spectral shape of the generated photons which is shown in figure 8.5. The main difference is the description at very low $p_\perp$. Since the method of normalization used here is completely insensitive to problems in the extrapolation to $p_\perp = 0$, the error is created only in a more complicated way. The GENESIS program normalizes the input distribution of all particles to an integral of one. They are then scaled using the particle ratios which are explicitly set by the user. If a chosen pion spectrum has more yield at small $p_\perp$, the number of photons per neutral pion does not change, since it is created by normalization to the integral number of π^0 for $p_\perp > 0.4$ GeV/c. What does change is the relative abundance of other sources in the spectrum, most important the decay $\eta \rightarrow \gamma\gamma$, and with it the total photon yield. This means that the effect of different input spectra for pions is more dramatic for higher ratios η/π^0. The error, conservatively assuming the highest plausible value of $\eta/\pi^0 = 12$ %, is $\pm$ 3.1 % for the integral photon yield.

8.5 Photons versus Multiplicity

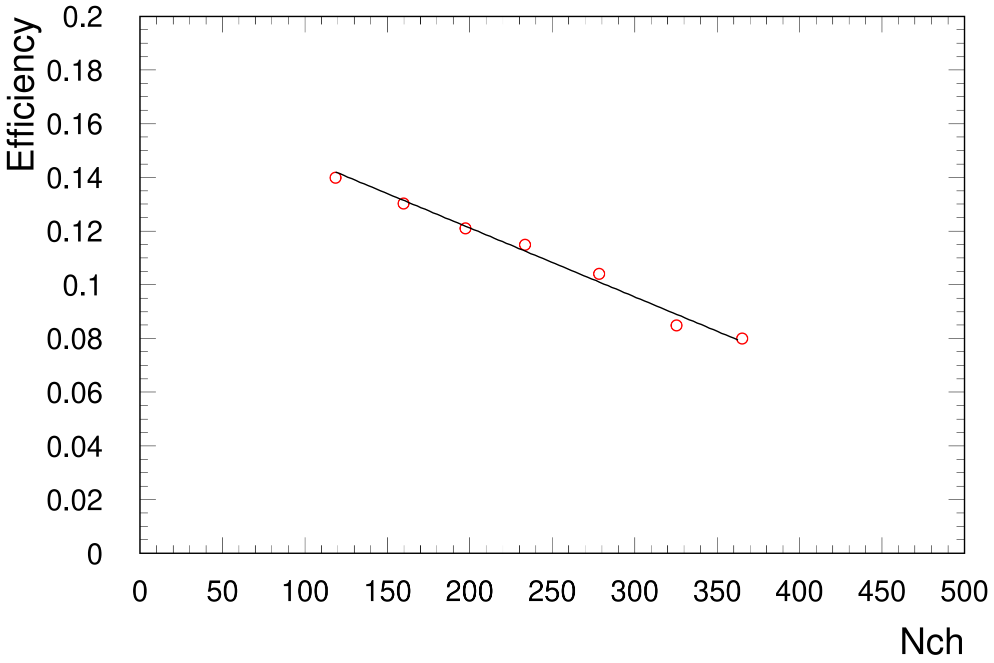

Figure 8.6: Efficiency as a function of Nch.

For the number of photons from hadron decays one expects a linear rise with multiplicity. This means that N_γ/N_{π^0} is constant versus Nch. A more than linear dependence could be a hint to new physics.

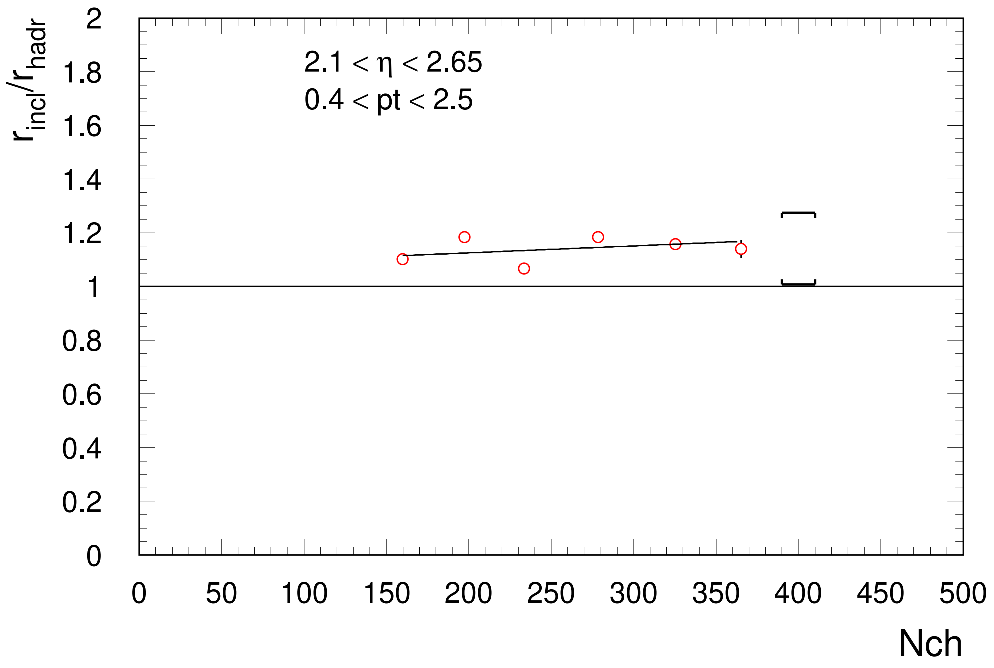

Figure 8.7: Photons per π^0 as a function of Nch, normalized to the expectation from hadron decays. The statistical errors are extremely small. The single bracket represents the systematic errors, assumed to be constant in Nch. No obvious deviation from a constant can be seen. This is quantified in the text. Note that the plotted systematic errors are largely correlated, as they do not depend on Nch.

To extract this signal the efficiency of the conversion reconstruction is calculated in each of the Nch-bins shown in figure 8.2, using the Monte-Carlo simulation. Figure 8.6 shows the result. The efficiency drops linearly from a maximum of 14 % at the lowest measured multiplicity to little more than half of this, 8 %, at the highest values of Nch. For normalization reasons, as explained in section 8.2, photons from events with the lowest Multiplicities do not enter the analysis. For the remaining six Nch-bins $r_\gamma = N_\gamma / N_{\pi^0}$ is calculated according to equation 8.3.
Figure 8.7 shows r_{incl}/r_{hadr} as a function of charged particle multiplicity. The correlated systematic errors are shown by the bracket, collectively for all data points. Within the uncertainties, no obvious deviation from a constant can be seen. To quantify this, a dependence of the form

$$\frac{r_{incl}}{r_{hadr}} = C \cdot \left(1 + \alpha \frac{dNch}{dy}\right) \tag{8.9}$$

is assumed and the parameters C and α are determined by a linear fit to the Nch spectrum. If photons are produced only by hadron decays one would expect C = 1

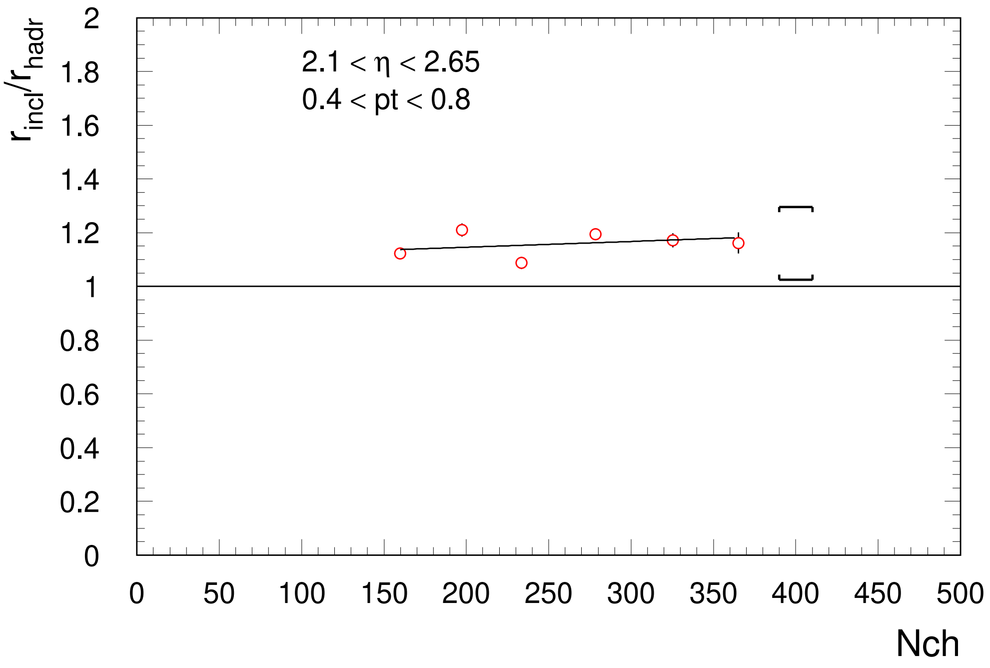

Figure 8.8: Photons per π^0 as a function of Nch for 0.4 GeV/c $<$ p$_\perp$ $<$ 0.8 GeV/c.

and $\alpha = 0$. The fit-result is

$$\alpha = (2.5 \pm 1.3_{stat} \begin{array}{c} + \\ - \end{array} \begin{array}{c} 2.5_{syst} \\ 3.7_{syst} \end{array}) \cdot 10^{-4} \tag{8.10}$$

in the full range of 0.4 GeV/c $<$ p$_\perp$ $<$ 2.5 GeV/c (figure 8.7). The statistical error is given by the least-squares-fit, the systematic error is discussed in the next section.

The mean charged particle multiplicity is $<$Nch$>$ $= 255 \pm 25_{sys}$ for the upper six Nch-bins which were used for the analysis (figure 8.2). The systematic error is estimated by variations of input-parameters for the Monte-Carlo correction of Nch (see also [27]). With this information and the assumption that the number of direct photons scales exactly quadratically with multiplicity one deduces an upper limit of

$$\frac{r_{incl} - r_{hadr}}{r_{hadr}} < 21\% \tag{8.11}$$

for the direct photon excess on the 90 % confidence-level.

The spectral shape in p$_\perp$ as seen in figures 8.4 and 8.5 could suggest that a direct photon signal can be seen only for transverse momenta above, say, 1 GeV/c. In this case it would be interesting to study the behaviour with multiplicity for different

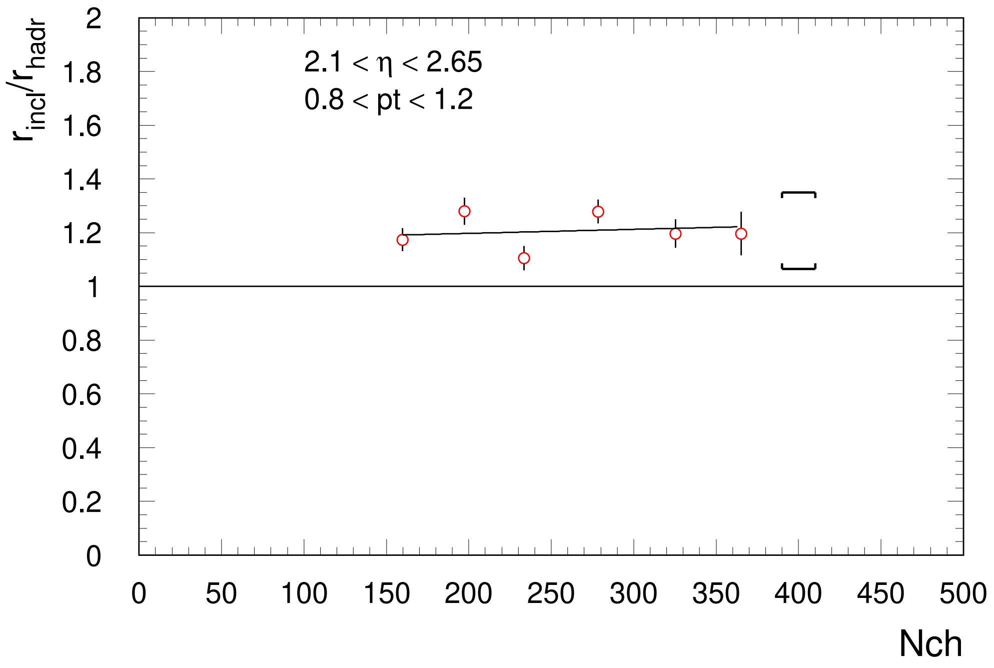

Figure 8.9: Photons per π^0 as a function of Nch for 0.8 GeV/c $< p_\perp <$ 1.2 GeV/c.

selections of $p_\perp$. Figures 8.8, 8.9, and 8.10 show the result of such a study. Whereas for the first two $p_\perp$-bins the result looks very much the same as for the integral over all $p_\perp$, the plot for transverse momenta of more than 1.2 GeV/c suggests a stronger rise with multiplicity. Unfortunately the statistical errors are too large to make a meaningful quantitative analysis.

8.5.1 systematic errors on $(N_\gamma/N_{\pi^0})(\mathrm{Nch})$

All error discussions in section 8.4 also apply to the ratio N_γ/N_{π^0} as a function of multiplicity. Since they are mostly independent of Nch, they are correlated for the points in figure 8.7 and do not fully enter in the determination of α. To make a statement on an eventual non-constant behaviour versus Nch only those errors are important which are not correlated.

- To smooth statistical fluctuations in the Monte-Carlo correction of the efficiency, a linear fit was applied to the efficiency versus Nch. Different plausible fit-results, i.e different possible slopes of the correction in figure 8.6 lead to an uncertainty of ± 4.1 % for the direct photon excess when going from the

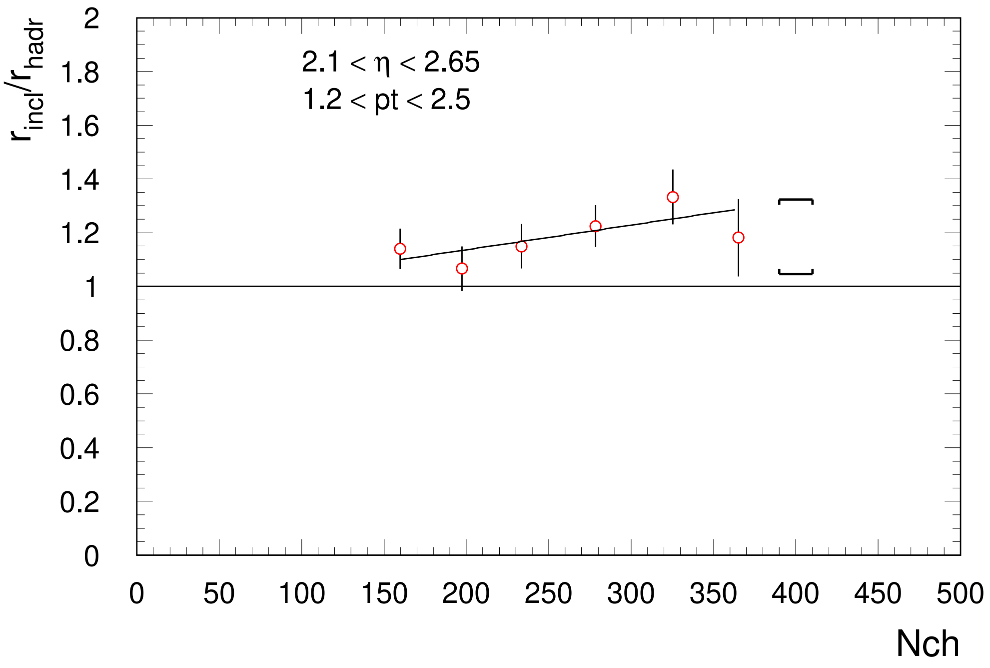

Figure 8.10: Photons per π^0 as a function of Nch for 1.2 GeV/c $< p_\perp <$ 2.5 GeV/c.

smallest to the largest considered multiplicities. This gives an error on α of $\pm 1.8 \cdot 10^{-4}$.

- A crucial point is the precision, differential in Nch, of the normalization to the number of π^0. For a quantitative asessment the number of h^- per event was plotted versus Nch in the six chosen bins and a linear fit was applied (figure 8.11). The scattering of the single points around the fit-result is found to be ± 2 % which is conservatively assumed to give the maximum possible error on the slope. The result for α is $\pm 1 \cdot 10^{-4}$.

- If the relative abundance of η-mesons changes when going from p-p to Pb-Pb collision systems, one can also expect a dependence on Nch. The measurement of WA98 [49] indicates such a behaviour and this already entered in the determination of the error for the $p_\perp$-spectra. For an estimation of the error on α one can assume that in very peripheral collisions the value measured for p-p by CERES/TAPS of $\eta/\pi^0 = 5.3$ % is still correct whereas for the most central collisions the result of calculations in the thermal model [46] can be used. Assuming that half the variation of 5.3 % $< \eta/\pi^0 <$ 8.5 % can be seen when moving from the smallest to the largest values of multiplicity, the resulting error on α is asymmetric and estimated as (+0 -2.7) $\cdot 10^{-4}$.

- The subtraction of negative Kaons from the measured h^- spectrum may also be subject to Nch-dependent errors. Using the same argumentation for different centralities as in the previous point one can deduct an error from measurements in different collision systems. The value obtained by the NA44 collaboration [40] was used for the correction in this analysis. Other measurements, summarized in table 8.2, would suggest to vary this value by ± 1 %. There is, however, no clear tendency visible, since the value for p-p is higher than that for S-S. Therefore a symmetric error is assumed and the impact on α is $\pm 1.3 \cdot 10^{-4}$. The same study could be made for the subtraction of anti-protons. Since this correction is comparatively small, the error is assumed to be negligible.

System	K^-/π^-	Reference
p-p	8.38 %	NA27 [51]
S-S	7.46 %	NA35 [52]
Pb-Pb	8.74 %	NA44 [40]
Pb-Pb	9.73 %	thermal model [46]

Table 8.2: Abundances of K^- relative to π^-. Measurements in various collision systems.

The quadratic sum of all these contributions gives an error on α of $(+2.5\,\text{-}3.7) \cdot 10^{-4}$. The positive and negative values are summed separately.

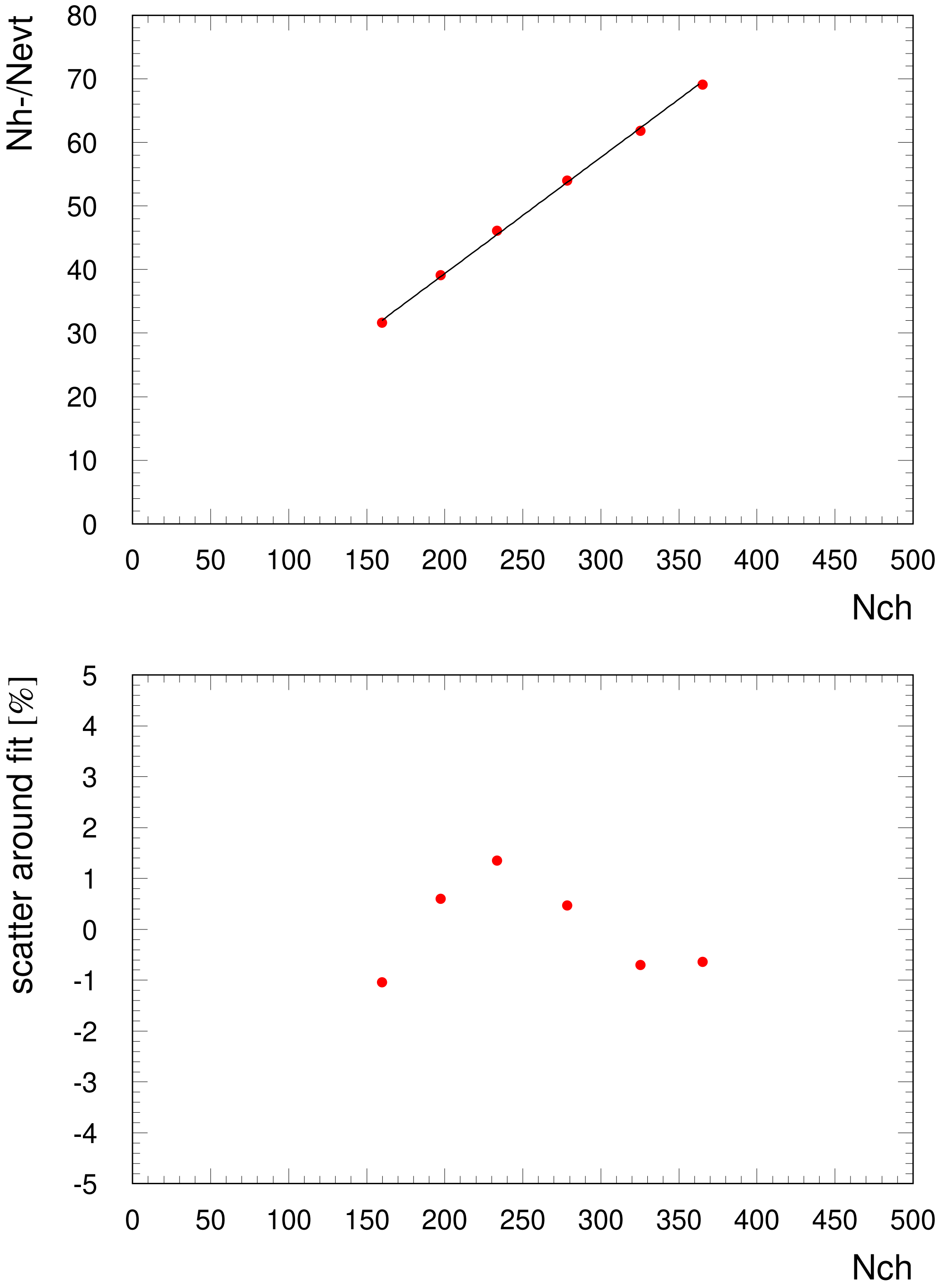

Figure 8.11: The upper plot shows CERES h^- per event as a function of Nch. The line is a linear fit to the data. The lower plot shows the scattering of the measured points with respect to the fitted curve. This is used for determination of the systematic error.

Chapter 9

Summary of the Results

The photon-spectra which where studied in this analysis show an excess production of 12.4 % over the predicted rate for hadron decays. Within the systematic errors of (+13.0-13.4) % this is not significant. The resulting upper limit for such an excess is 33.8 % on the 90 % confidence-level. The spectral shape shows a rise with $p_\perp$ in the region above 0.5 GeV/c and below 0.8 GeV/c. From there on the signal stays constant at 15 %.
In the multiplicity-dependence of the number of photons per neutral pions a, within the errors, constant behaviour can be seen. A fit to the data gives a slope of $\alpha = (2.5 \pm 1.3_{stat}\ (+2.5\ -3.7)_{sys}) \cdot 10^{-4}$. This results in an upper limit of 21 % for an excess photon production on the 90 % confidence-level, if one assumes that the number of direct photons scales quadratically with multiplicity.
A closer look, dividing the data-set in three different bins in $p_\perp$, seems to indicate an interesting behaviour with multiplicity for photons with $p_\perp > 1.2$ GeV/c. Unfortunately the statistical errors become dominant in this region.
These results are consistent with a preliminary analysis by the WA98 collaboration, which also looks for direct photons at the CERN SPS [50]. Also here, no stronger than linear rise of the number of photons with multiplicity was found. Their $p_\perp$-spectrum shows an excess photon production of 20 % which has, however, the striking property of rising from 0 % at small $p_\perp$ quite suddenly to the full value at a transverse momentum of 1 GeV/c. Here one may find an incompatibility to the CERES measurement, once the result is available including systematic errors.

Appendix A

Frequently Used Quantities

Some of the quantities used throughout the text are not self-explanatory and may indeed be unknown to the not so dedicated follower of heavy ion physics. Some words of explanation can be found in the paragraphs below.

A.1 Transverse Momentum $p_\perp$

In the fixed-target experiments used for heavy ion physics up to the present, $p_\perp$ almost always means momentum transverse to the beam axis.

$$p_\perp = p \cdot \sin\Theta \quad ,$$

where Θ is the polar angle of the track. For the small angular acceptance of CERES (140 mrad $< \Theta <$ 250 mrad) a first approximation can always be made with $p_\perp = 1/5 \cdot p$

A.2 Transverse Mass $m_\perp$

The transverse mass of a particle is the quadratic sum of its transverse momentum and its mass

$$m_\perp = \sqrt{p_\perp^2 + m_0^2} \quad ,$$

where m_0 is the particle rest mass.

A.3 Rapidity y

The rapidity of a particle can be loosely described as a kind of velocity with respect to a reference direction. This reference direction is here again that of the beam axis (z). The rapidity is then defined as

$$y = \frac{1}{2} \ln \frac{E + p_z}{E - p_z} \tag{A.1}$$

where E is the energy, p_z is the momentum component in beam direction.

Under Lorenz transformation along the z-axis, this quantity is transformed by adding a constant - the rapidity of the new reference system. All rapidities measured in a collision are in the interval between target-rapidity ($y = 0$) and projectile rapidity ($y = 5.84$ for $p_{beam} = 158$ A GeV/c.

A.4 Pseudo-Rapidity η

To calculate the particle rapidity, its mass and momentum must be known. Much more easy to determine is the so called pseudo-rapidity

$$\eta = -\ln(\tan\frac{\theta}{2}) \tag{A.2}$$

where Θ is the polar angle of the track. Because of this simplicity and the fact that in the limit of large rapidities and small masses η is a good approximation for y, this quantity is frequently used to characterize a particle trajectory.

Bibliography

[1] E.V.Shuryak, Phys. Lett. B78 (1978) 150.

[2] M.C.Abreu et al., *Physics Letters B* **410** (1997) 337

[3] T.Ullrich, Doktorarbeit Ruprecht-Karls-Universität (1994).

[4] G. Agakichiev et al., *Phys. Rev. Lett.* **75** (1995) 1272

[5] G.Agakichiev et al. (CERES), Phys.Lett.B. 422 (1998) 405

[6] A.Drees, Nuc. Physics A610 (1996) 536c-551c
A.Drees, Nuc. Physics A630 (1998) 449c-460c

[7] R.Baur et al. (CERES), Z.Phys. C71 (1996) 571

[8] T. Ullrich et al., *Nucl.Phys.* **A610** (1996) 317c.

[9] T. Matsui and H. Satz, Phys. Lett. **B178** (1986) 416

[10] C.Voigt, Doktorarbeit Ruprecht-Karls-Universität (1998).

[11] D. Irmscher, Doktorarbeit Ruprecht-Karls-Universität (1993).

[12] G. Agakichiev *et al.* Phys. Lett. B (1998) (in print)

[13] R. Albrecht et al. *Phys. Rev. Lett* **76** (1996) 3506

[14] C.Y.Wong, Introduction to High-Energy Heavy-Ion Collisions, World Scientific (1994).

[15] M.McLaughlin, *Phys.Rev.Lett.* **51** (1983) 971.

[16] D.L.Adams, *Phys.Lett.* **B345** (1995) 569.

[17] J.Badier, *Z.Phys.* **C31** (1986) 341.

[18] M.Neubert, *Z.Phys.* **C42** (1989) 231.

[19] R.Baier, H.Nakkagawa, A.Niegawa, K.Redlich, *Z.Phys.* **C53** (1992) 433.

[20] J.Kapusta et al., *Physical Review D* **44** (1991) 2774.

[21] T. Åkesson et al., *Z.Phys.* **C46** (1990) 369.

[22] R. Albrecht et al., *Z.Phys.* **C51** (1991) 1.

[23] CERES/NA45-Collaboration, Proposal to the CERN SPSC 88-25, SPSC/P237.

[24] CERES/NA45-Collaboration, Proposal to the CERN SPSC 94-1, SPSC/P280.

[25] F. Ceretto, *Proc. 13th int. conf. on ultra-relativistic nucl. nucl. coll.*, Yapan (1997)

[26] F. Ceretto, Doktorarbeit Ruprecht-Karls-Universität (1998).

[27] B.Lenkeit, Doktorarbeit Ruprecht-Karls-Universität (1998).

[28] B.Lenkeit, Diplomarbeit Ruprecht-Karls-Universität (1995).

[29] E. Gatti and P. Rehak, Nucl. Instr. and Methods **A 225** (1984) 608

[30] O. Nix, Diplomarbeit Ruprecht-Karls-Universität (1996).

[31] J. Seguinot und T. Ypsilantis, Nucl. Instr. Meth. **142** (1977) 377.

[32] G. Booch, Object oriented analysis and design, The Benjamin Cummings Publishing, Inc.

[33] C. Weber, Diplomarbeit Ruprecht-Karls-Universität (1997).

[34] R. Brun et al., CERN DD/EE/84-1 .

[35] U. Faschingbauer, Doktorarbeit Ruprecht-Karls-Universität (1993).

[36] Bjarne Stroustrup, *The C++ Programming Language*, Addison-Wesley (1985-1994)

[37] G. Agakichiev et al., *Nucl. Instr. and Methods* **A 394** (1997).

[38] Particle Data Group, R.M. Barnett et al. *Phys.Rev* **D 54**, 1 (1996).

[39] private communication, Johanna Stachel (1998)

[40] Kaon and Proton Ratios from Central Pb+Pb Collisions at the CERN SPS, M.Kaneta for the NA44 collaboration, *Proc. 13th int. conf. on ultra-relativistic nucl. nucl. coll.*, Yapan (1997)

[41] Hadron Distributions - Recent Results..., N.Xu for the NA44 collaboration, *Proc. 12th int. conf. on ultra-relativistic nucl. nucl. coll.*,
Germany (1996)

[42] S.V.Afanasiev et al., *Nucl.Phys.* **A610** (1996) 188c.

[43] F.Ceretto, private communication, (1998).

[44] P.Braun-Munzinger, J.Stachel, J.P.Wessels and N.Xu, *Phys. Lett.* B 365, 1 (1996)

[45] J.Stachel, Proceedings of the Int. Nucl. Phys. Conf. 1998, Paris

[46] I.Heppe, Diplomarbeit Ruprecht-Karls-Universität (1998).

[47] G. Agakichiev et al. (CERES Collaboration), Neutral meson production in p-Be and p-Au collisions at 450 GeV beam energy, *Euro.Phys.Jour.* C4 (1998) 231.

[48] G. Agakichiev et al. (CERES Collaboration), Systematic study of low mass electron pair production in p-Be and p-Au collisions at 450 GeV beam energy, *Euro.Phys.Jour.* C4 (1998) 249.

[49] C. Blume, Doktorarbeit Universität Münster (1998)

[50] B.Wiesloch for the WA98 collaboration *Proc. 13th int. conf. on ultra-relativistic nucl. nucl. coll.*,
Yapan (1997)

[51] M. Aguilar-Benitez et al. *Z.Phys.* **C 50** (1991) 405

[52] D. Röhrich et al. *Nucl.Phys.* **A 566** (1994) 35c

The CERES Collaboration

Members of CERES from 1995 until December 1998:

Physikalisches Institut der Universität Heidelberg

H. Appelshäuser, R. Bell, R. Baur, K. Dandl, A. Drees, P. Ernst, S. Esumi, P. Glässel, C. Jung, B. Lenkeit, M. Messer, A. Pfeiffer, M. Richter, W. Schmitz, W. Seipp, H.J. Specht, J. Stachel, H. Tilsner, T.S. Ullrich, C. Voigt, C. Weber, J.P. Wessels, T. Wienold, B. Windelband

Guest of Universität Heidelberg,
S. Voloshin

Max-Planck-Institut für Kernphysik, Heidelberg

F. Ceretto, U. Faschingbauer, Ch. Fuchs, M. Hemberger, O. Nix, J. Rak, J. Slivova J.P. Wurm

Gesellschaft für Schwerionenforschung, Darmstadt

P. Braun-Munzinger, G .Hering, A. Marin, D. Miskowiec, A. Sharma, P. Stiller

Weizmann Institure of Science, Rehovot, Israel

A. Cherlin, Z. Fraenkel, C. P. de losHeros, A. Gnaenski, A. Milov, I. Ravinovich, E. Socol, G. Tel-Zur, I. Tserruya

CERN, Genf, Schweiz

J. Schukraft

Brookhaven National Laboratory, Brookhaven, USA

P. Rehak, H. Kraner, P. Holl

Politecnico di Milano, Mailand, Italy

E. Gatti, M. Sampietro

Joint Institute for Nuclear Research, Dubna, Russia

G. Agakischiev, Y. Minaev, Y. Panebrattsev, S. Razin, N. Saveljic, S. Schimansky, V. Yurevich

Acknowledgments

I would like to thank everybody who contributed to the success of this work, especially Prof. Specht for the opportunity to work on the subject within his group at Heidelberg and Prof. J.v.Krogh for accepting to write the second expertise.
Many thanks to Axel Drees for the constant support, endless discussions even across the atlantic ocean, psychological treatment against demotivation, and in the end also acting as best-man.
Thanks also to the Heidelberg-"crew", among them the fellow combatants Björn Lenkeit, Carsten Voigt and Federica Ceretto (I'll come to you again later), but also the senior members Andreas Pfeiffer and Thomas Ullrich for many a happy night in the counting-room with discussion, drinks, and data-aquisition.
One should not forget that without the electronic-chaps there would be no data for all the others to analyze. Roland Baur, Michael Richter, and Wolfram Seipp always managed to get everything going and generally to do the "miracle at the eleventh hour". Thanks to all of you.
Besonderer Dank gilt natürlich auch meinen Eltern, die durch Ihre Unterstützung die Arbeit am Physikalischen Institut erst ermöglichten.
Non tutti hanno la fortuna di lavorare con la piu' bell Fisica del mondo e alla fine anche sposarla. Grazie mille per gli "h^-", per dire sempre che cucino bene e per "il piccolo".